

# Catalytic NO<sub>x</sub> Reduction on Nanomaterials

THESIS

*Submitted in partial fulfilment  
of the requirements for the degree of  
DOCTOR OF PHILOSOPHY*

*By*

Reeshma Rameshan  
ID No. 2018PHXF0412H

*Under the supervision of*  
Prof. Sounak Roy



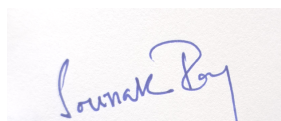
**BITS Pilani**  
Pilani | Dubai | Goa | Hyderabad

BIRLA INSTITUTE OF TECHNOLOGY AND SCIENCE, PILANI  
2024

## CERTIFICATE

This is to certify that the thesis titled, "Catalytic NO<sub>x</sub> Reduction on Nanomaterials" submitted by Reeshma Rameshan, ID No. 2018PHXF0412H for the award of Ph.D. of the institute embodies original work done by her under my supervision.

Signature of the Supervisor:



Name in capital letters: Prof. SOUNAK ROY

Designation: Professor

Date: 05-04-2024

## Declaration of Authorship

I hereby declare that the matter embodied in this thesis entitled "Catalytic NO<sub>x</sub> Reduction on Nanomaterials" is the result of investigations carried out by me in the Materials Chemistry Lab, BITS-Pilani, Hyderabad Campus, India, under the supervision of Prof. Sounak Roy.

In keeping with the general practice of reporting scientific observations, due acknowledgment has been made whenever the work described is based on the findings of other investigators. Any omission which might have occurred by oversight or error in judgement is regretted.

Signed: \_\_\_\_\_



Date: 05-04-2024  
\_\_\_\_\_

*Dedicated to My Mother*



## *Acknowledgements*

I am genuinely grateful for the opportunity to reflect on my arduous journey and acknowledge the instrumental contributions of the remarkable individuals who have guided and supported me along the way. With great pleasure, I wish to extend my deepest gratitude to those who have played pivotal roles in bringing my thesis to fulfillment.

Foremost among the people to whom I wish to express my genuine gratitude is my supervisor, Prof. Sounak Roy, from whom I have gained profound knowledge and been a constant support throughout these years. His motivation and guidance have been the guiding light in the entire Ph.D. study and research. I consider myself immensely fortunate to have had the privilege to work with him. I am thankful for his invaluable insights and comments in shaping the thesis and for the time and dedication he has invested.

I would like to express my gratitude to a multitude of people who have aided me in various ways during my Ph.D. tenure. My heartfelt thanks go out to my doctoral advisory committee members, Dr. Satyapaul Singh and Dr. Himashu Aggarwal, for their continuous support and encouragement. I am also indebted to Dr. Durba Roy, the former convener of the doctoral research committee, for her invaluable suggestions, and Dr. Tanmay Chatterjee, convener of the doctoral research committee, for his guidance through the thesis submission process. Also, I am grateful to Prof. Manab Chakravarty, the former Head of the Department, and the entire faculty of the Department of Chemistry for their valuable support and discussions along the path.

I am deeply thankful to Dr. Satyapaul Singh for his interactions and insightful discussions that enriched my research and his contributions to kinetic modeling. I would also like to thank Dr. Parag A. Deshpande and Dr. Sayan Kanungo for their expertise in DFT calculations done in the study.

My sincere appreciation goes to the former Vice-Chancellor Prof. Souvik Bhattacharyya and the current Vice-Chancellor Prof. V Ramgopal Rao of BITS Pilani and Prof. G. Sundar, the director of BITS Pilani Hyderabad Campus, for providing me with the opportunity to pursue my doctoral research. I wish to express my sincere thanks to Prof. Vamsi Krishna Venuganti, Associate Dean of the Academic-Graduate Studies and Research Division (AGSRD), and Mr. Praveen from AGSRD for their invaluable assistance in navigating the course formalities.

My earnest thanks to HBL for providing financial support in the form of project fellowship and contingency. I would also thank BITS-Pilani, Hyderabad Campus for providing me the institute fellowship that has been crucial to my research endeavors.

Now I would like to express my indebted gratitude to those individuals who helped and supported me academically and personally. I thank my senior fellow researchers Dr. Swapna Challagulla

and Dr. Soumitra Payra for the constant help and subject discussions. My special thanks to Meenu PC for the times she had helped in my hardships. The unflagging support from Dhanya V encouraged me in every way and I am deeply obliged to her. My fellow lab mates Aathira B, Saraswathi Roy, Mariya Midhu Francis, Amita Ann Mathews, and Aniket Diliprao Balapure have been a constant source of encouragement and gregariousness. I am truly grateful for the love and support I received from fellow researchers especially, Dr. Arun Mohan, Dr. Arunraj, Dr. Karuna Anna Sajeevan, Paramita Pattanayak, Anup K Pradhan, Yogesh Khetmalis, and Akhil. I extend my sincere appreciation to the research scholars across the various departments and my colleagues in the department of chemistry for their time and camaraderie, which made my stay on campus truly memorable. Special thanks to Krishnendu Sivadas for assisting LaTeX during thesis writing. I also wish to acknowledge the invaluable cooperation of the non-teaching staff in the chemistry department and the technicians in the central analytical lab.

My deepest gratitude goes to my mother Bindu V V for her unwavering care, support, love, and blessing. I am especially thankful to my sister Swetha Rameshan for her endless support and encouragement, and to my aunt Sujitha Santhosh. My dearest friends Ar. Sachin Raj, Prashanna Balaji, Vishnu PV, Dr. Arjun Muruges, Ar. Anand, and Arjun Sukumar have been pillars of strength throughout this journey.

As my doctoral research unfolded as a personal journey, it would not have been possible without the efforts and assistance of my colleagues, friends, and well-wishers over the past five years. My heartfelt thanks extend to all those mentioned here and to others whose names I may have inadvertently omitted. Your contributions have been pivotal to my success, and I am deeply appreciative of your continuous support and encouragement. Last but not least, I deeply appreciate myself for not giving up under any strenuous circumstances.

Reeshma Rameshan

# Abstract

A higher quality of life and environmental sustainability are two intertwined goals that could be achieved through the mitigation of pollution to promote a cleaner and healthier environment for current and future generations. Environmental pollution, a critical and ever-increasing concern, poses a major threat to the delicate balance of ecosystems and human health worldwide. Among the myriad of pollutants, nitrogen oxides ( $\text{NO}_x$ ) hold a prominent position as one of the most pervasive and detrimental classes of pollutants. The introduction of  $\text{NO}_x$  compounds, into the atmosphere and to the water bodies arises from a wide range of anthropogenic activities, including combustion processes in vehicles, industrial operations, and energy generation. These emissions contribute to various environmental problems, encompassing air quality deterioration, acid rain formation, and the exacerbation of respiratory issues in humans. To address this, stringent regulations and innovative abatement technologies are crucial.

The  $\text{NO}_x$  abatement technologies are challenged with the operational ability in low temperature window of the catalyst. Chapter 1 introduces the importance and current status of the research happening in the field of de $\text{NO}_x$  catalysts. In Chapter 2, we present our studies on dispersing Pt on as-synthesized ZIF-8 and explored the material for thermal  $\text{NO}_x$  reduction. The Pt nanoparticles were found to be highly dispersed over the surface of ZIF-8. The ZIF-8 possessed high surface area, porosity, and basic imidazolate link which helped in high NO adsorption capability. The Pt/ZIF-8 catalyst exhibited efficient  $\text{NO}_x$  reduction at low temperatures while maintaining good recyclability and thermal stability, outperforming other zeolitic catalysts. This enhanced low temperature reactivity is attributed to the excellent dispersion of Pt nanoparticles and their interaction with the ZIF-8 support. The materials' surface properties were studied and characterized and compared the catalytic performance of Pt dispersed over commercial zeolite Y.

It is important to understand the reaction mechanism of the thermal  $\text{NO}_x$  reduction thereby helping the researchers to benefit in preparing more efficient catalysts. In Chapter 3, we have chosen non-noble metal catalysts to investigate the active surface sites and the potential mechanism in the catalytic reduction of NO over solid solutions of  $\text{Ce}_{1-x}\text{Ni}_x\text{O}_{2-\delta}$ . An integrated experimental and theoretical approach was conducted to evaluate the role of *in-situ*  $\text{Ni}^{2+}$  within the  $\text{CeO}_2$  lattice and dispersed on the  $\text{CeO}_2$ . The observed enhancement in catalytic activity in reduced  $\text{Ce}_{1-x}\text{Ni}_x\text{O}_{2-\delta}$  species was confirmed by the Density functional theory (DFT) calculations as active sites in the reaction mechanism. Additionally, a kinetic model was developed to identify the rate-determining step in the NO reduction mechanism by  $\text{H}_2$  over supported metal catalysts  $\text{Ce}_{1-x}\text{Ni}_x\text{O}_{2-\delta}$ .

The escaped gaseous  $\text{NO}_x$  is converted to the aqueous  $\text{NO}_x$  when moisture gets in contact with the  $\text{NO}_x$  present in the atmosphere and pollutes the water bodies, hence it is important we

abate the aqueous  $\text{NO}_x$ . The next chapter, chapter 4, is devoted to the electrocatalytic reduction of nitrates to ammonia wherein the idea of circular economy pitches in. Yet, this technology faces issues such as poor selectivity, low Faradic efficiency, and concurrent hydrogen evolution. The use of nanoalloys shows promise by adjusting the electronic structure and interaction with nitrate and intermediates, enhancing selectivity. We doped Cu with Ni and Zn to create  $\text{Cu}_{0.85}\text{Ni}_{0.15}/\text{C}$  and  $\text{Cu}_{0.85}\text{Zn}_{0.15}/\text{C}$  from bimetallic metal-organic framework materials. Detailed investigation of nitrate reduction on these nanomaterials revealed  $\text{Cu}_{0.85}\text{Zn}_{0.15}/\text{C}$  outperformed  $\text{Cu}_{0.85}\text{Ni}_{0.15}/\text{C}$  and  $\text{Cu}/\text{C}$ , supported by first-principles calculations showing the importance of *d*-band modulation in influencing surface interactions, thus improving selectivity and catalytic efficiency. The final chapter, Chapter 5, presents the overall conclusion and provides insight into future prospects.

# Contents

<b>Certificate</b>	<b>i</b>
<b>Declaration of Authorship</b>	<b>ii</b>
<b>Acknowledgements</b>	<b>iv</b>
<b>Abstract</b>	<b>vi</b>
<b>Contents</b>	<b>viii</b>
<b>List of Tables</b>	<b>x</b>
<b>List of Figures</b>	<b>xi</b>
<b>Abbreviations</b>	<b>xiv</b>
<b>1 NO<sub>x</sub> and its Nefarious Impact</b>	<b>1</b>
1.1 Introduction . . . . .	1
1.1.1 Formation of NO <sub>x</sub> . . . . .	2
1.1.2 Nefarious environmental effect of NO <sub>x</sub> and Consequent Regulations . . . . .	3
1.2 Catalysis for deNO <sub>x</sub> ification . . . . .	5
1.2.1 Gaseous NO <sub>x</sub> . . . . .	6
1.2.2 Aqueous NO <sub>x</sub> . . . . .	9
1.3 Scope and objective of the work . . . . .	10
<b>2 Low temperature catalytic reduction of NO over porous Pt/ZIF-8</b>	<b>13</b>
2.1 Introduction . . . . .	13
2.2 Materials and Methods . . . . .	14
2.2.1 Synthesis of Catalysts . . . . .	14
2.2.2 Characterizations . . . . .	15
2.2.3 Catalytic Reduction of NO . . . . .	16
2.3 Results and Discussion . . . . .	17
2.4 Conclusion . . . . .	26

---

<b>3 Probing the surface active sites of <math>\text{Ce}_{1-x}\text{Ni}_x\text{O}_{2-\delta}</math> for catalytic reduction of NO</b>	<b>28</b>
3.1 Introduction . . . . .	28
3.2 Materials and Method . . . . .	29
3.2.1 Synthesis of Catalysts . . . . .	29
3.2.2 Characterization . . . . .	31
3.2.3 Catalytic Reduction of NO . . . . .	31
3.2.4 Theoretical Calculations . . . . .	32
3.3 Results and Discussion . . . . .	33
3.3.1 Structural, Surface and Electronic Properties . . . . .	33
3.4 Catalytic performances . . . . .	39
3.5 Mechanistic probe . . . . .	45
3.6 Conclusion . . . . .	55
<b>4 Rags to Riches: Meliorating the Electrocatalytic Reduction of Nitrate to Ammonia over Cu-based Nano-alloys</b>	<b>57</b>
4.1 Introduction . . . . .	57
4.2 Materials and Methods . . . . .	58
4.2.1 Synthesis of Catalysts . . . . .	58
4.2.2 Characterizations . . . . .	59
4.3 Results and Discussion . . . . .	63
4.3.1 Structural, Surface and Electronic Properties . . . . .	63
4.3.2 $\text{NO}_x\text{RR}$ . . . . .	68
4.4 Conclusion . . . . .	78
<b>5 Understanding the Catalytic Materials in <math>\text{NO}_x</math> Removal: A Summary and Conclusion</b>	<b>79</b>
5.1 Insight into the Catalytic Materials . . . . .	79
5.2 Future scope of the work . . . . .	80
<b>Bibliography</b>	<b>82</b>
<b>List of Publications and Conference Presentations</b>	<b>92</b>
<b>Biography of the Candidate</b>	<b>93</b>
<b>Biography of the Supervisor</b>	<b>93</b>

# List of Tables

2.1	Surface area, pore volume, and pore diameter of the synthesized catalysts . . . . .	24
3.1	Rietveld refinement parameters of pristine $\text{CeO}_2$ and $\text{Ce}_{1-x}\text{Ni}_x\text{O}_{2-\delta}$ ( $x=0.05$ and $0.1$ ) . . . . .	35
3.2	Kinetic parameters for as-prepared and reduced $\text{Ce}_{0.9}\text{Ni}_{0.1}\text{O}_{2-\delta}$ . . . . .	55
4.1	BET surface area of MOFs and MOF-derived nano-catalysts . . . . .	67

# List of Figures

1.1	NO <sub>x</sub> emission in (a) India in the year 2019 (IEA 2021) (b) Countries in European Union in the year 2022 (EEA Report 2022) . . . . .	2
1.2	Regulatory emission standards implemented in India: Bharat Stage VI . . . . .	5
2.1	Schematic diagram of catalytic reactor . . . . .	16
2.2	XRD profiles of (a) ZIF-8 and 1% Pt/ZIF-8, (b) zeolite Y and 1% Pt/zeolite Y, (c) TGA profiles of the synthesized catalysts, and (d) Temperature-dependent <i>in-situ</i> XRD profile of 1% Pt/ZIF-8 . . . . .	18
2.3	The reduction of NO by H <sub>2</sub> over the synthesized catalysts with equimolar mixture of 1:1 vol.% NO and H <sub>2</sub> . . . . .	19
2.4	(a) NO-TPD profiles of the synthesized catalysts and (b) H <sub>2</sub> -TPR profiles of 1% Pt/ZIF-8 and 1% Pt/zeolite Y . . . . .	21
2.5	FE-SEM images of (a) ZIF-8, (b) 1% Pt/ZIF-8, (e) zeolite Y, (f) 1% Pt/zeolite Y, and (c,d) HR-TEM images of 1% Pt/ZIF-8 . . . . .	22
2.6	STEM-EDS mapping of 1% Pt/ZIF-8 . . . . .	22
2.7	XPS (a) core level spectra of Zn in ZIF-8 and 1% Pt/ZIF-8, (b) core level spectra of Al and Pt in zeolite Y and 1% Pt/zeolite Y catalysts, and (c) core level spectra of Pt in 1% Pt/ZIF-8 . . . . .	23
2.8	(a) N <sub>2</sub> adsorption-desorption isotherms and (b) NLDFT pore size distribution plot of the synthesized catalysts . . . . .	24
2.9	(a) FT-IR spectra of NO <sub>2</sub> adsorption over ZIF-8 and 1% Pt/ZIF-8, ad (b) a proposed molecular mechanism of NO reduction over 1% Pt/ZIF-8 surface . . . . .	25
2.10	Recyclability of the reduction NO by H <sub>2</sub> over 1% Pt/ZIF-8 . . . . .	26
2.11	(a) XRD patterns of 1% Pt/ZIF 8 after reduction of NO by H <sub>2</sub> , (b) FE-SEM images of 1% Pt/ZIF 8 after reduction of NO by H <sub>2</sub> , and (c) Pt core level XPS Spectra of 1% Pt/ZIF 8 after reduction of NO by H <sub>2</sub> . . . . .	26
3.1	(a) XRD patterns of pristine CeO <sub>2</sub> and as-prepared Ce <sub>0.9</sub> Ni <sub>0.1</sub> O <sub>2-δ</sub> (x = 0.05, 0.1, 0.2) and reduced Ce <sub>0.9</sub> Ni <sub>0.1</sub> O <sub>2-δ</sub> , (b) Enlarged XRD profile of Ce <sub>0.8</sub> Ni <sub>0.2</sub> O <sub>2-δ</sub> , (c) XRD profile of 10% NiO/CeO <sub>2</sub> and 10% Ni/CeO <sub>2</sub> (IMP), and (d) Rietveld refined patterns of pristine CeO <sub>2</sub> and as-prepared Ce <sub>0.9</sub> Ni <sub>0.1</sub> O <sub>2-δ</sub> (x=0.05 and 0.1) and reduced Ce <sub>0.9</sub> Ni <sub>0.1</sub> O <sub>2-δ</sub> . . . . .	34
3.2	HR-TEM and particle size distribution of as-prepared and reduced Ce <sub>0.9</sub> Ni <sub>0.1</sub> O <sub>2-δ</sub> 36	
3.3	(a) Ce 3 <i>d</i> core level spectra in pristine CeO <sub>2</sub> , and as-prepared and reduced Ce <sub>0.9</sub> Ni <sub>0.1</sub> O <sub>2-δ</sub> , (b) Ni 2 <i>p</i> core level spectra of as-prepared and reduced Ce <sub>0.9</sub> Ni <sub>0.1</sub> O <sub>2-δ</sub> , (c) Ni2 <i>p</i> core level spectra of 10% NiO/CeO <sub>2</sub> and 10% Ni/CeO <sub>2</sub> (IMP), and (d) O 1 <i>s</i> core level spectra of pristine CeO <sub>2</sub> , and as-prepared and reduced Ce <sub>0.9</sub> Ni <sub>0.1</sub> O <sub>2-δ</sub> 37	



3.4	(a) FE-SEM of (a) pristine $\text{CeO}_2$ , (b) as-prepared $\text{Ce}_{0.9}\text{Ni}_{0.1}\text{O}_{2-\delta}$ , (b) reduced $\text{Ce}_{0.9}\text{Ni}_{0.1}\text{O}_{2-\delta}$ , and (d) $\text{N}_2$ sorption isotherms of pristine $\text{CeO}_2$ , as-prepared and reduced $\text{Ce}_{0.9}\text{Ni}_{0.1}\text{O}_{2-\delta}$ . . . . .	39
3.5	NO conversion efficiency plot as a function of temperature over the synthesized catalysts . . . . .	40
3.6	(a) XRD, (b) XPS, and (c) FE-SEM characterization of exhausted catalysts after NO reduction by $\text{H}_2$ . . . . .	41
3.7	Cyclic NO reduction experiments on oxidized and reduced $\text{Ce}_{0.9}\text{Ni}_{0.1}\text{O}_{2-\delta}$ . . . . .	42
3.8	Ni $2p$ and O $1s$ core level spectra of oxidized and reduced $\text{Ce}_{0.9}\text{Ni}_{0.1}\text{O}_{2-\delta}$ before Cycle 2 . . . . .	43
3.9	Partial pressure vs. $W/F_{\text{NO}}$ plot over (a) as-prepared $\text{Ce}_{0.9}\text{Ni}_{0.1}\text{O}_{2-\delta}$ , (b) reduced $\text{Ce}_{0.9}\text{Ni}_{0.1}\text{O}_{2-\delta}$ , and (c) Activation Energy from Arrhenius plot . . . . .	44
3.10	Adsorption configurations of NO over $\text{Ce}_{0.9}\text{Ni}_{0.1}\text{O}_{2-\delta}$ : (a) $\text{NO}_{2-1}$ , (b) $\text{NO}_{2-2}$ , (c) $\text{NO}_{2-3}$ , (d) NiNO-1, (e) NiNO-2, (f) Ce-bi-NO, (g) Ce-mono-NO, and (h) $\text{NO}_v$ . . . . .	45
3.11	Adsorption configurations of second NO molecule over NO- $\text{Ce}_{1-x}\text{Ni}_x\text{O}_{2-\delta}$ : (a) $2\text{NO}_{v1}$ , (b) $2\text{NO}_{v2}$ , (c) $2\text{NO}_{v3}$ , and (d) $2\text{NONO}_2$ . . . . .	47
3.12	Adsorption energetics for NO over $\text{Ce}_{1-x}\text{Ni}_x\text{O}_{2-\delta}$ (a) adsorption of first NO (b) adsorption of second NO . . . . .	47
3.13	Adsorption configuration of surface hydroxyl over $\text{Ce}_{1-x}\text{Ni}_x\text{O}_{2-\delta}$ formed by dissociative adsorption of $\text{H}_2$ . . . . .	48
3.14	Comparison of energetics and the associated barriers for the formation of surface $\text{N}_2\text{O}$ species . . . . .	49
3.15	Reaction rate variation with respect to partial pressure of NO in terms of $\frac{1}{R^{1/3}}$ vs $\frac{10^3}{P_{\text{NO}}}$ plot at a constant partial pressure of $\text{H}_2$ ( $P_{\text{H}_2}=506.17$ Pa) for (a) as-prepared and (b) reduced $\text{Ce}_{0.9}\text{Ni}_{0.1}\text{O}_{2-\delta}$ catalysts . . . . .	54
3.16	Parity plot to compare model-predicted and experimental reaction rates . . . . .	55
4.1	The powder (a) XRD patterns (b-d) the corresponding FE-SEM micrographs of the as-prepared monometallic MOF Cu-BTC, and the bimetallic MOFs $\text{Cu}_{0.85}\text{Ni}_{0.15}$ -BTC and $\text{Cu}_{0.85}\text{Zn}_{0.15}$ -BTC, and (e,f) XRD patterns of Zn-BTC, and Ni-BTC . . . . .	63
4.2	The powder XRD patterns and the corresponding FE-SEM micrographs of the as-prepared (a-c) Cu/C, (d-f) $\text{Cu}_{0.85}\text{Ni}_{0.15}/\text{C}$ , and (g-i) $\text{Cu}_{0.85}\text{Zn}_{0.15}/\text{C}$ . . . . .	64
4.3	FE-SEM EDAX Mapping of (a) Cu/C, (b) $\text{Cu}_{0.85}\text{Ni}_{0.15}/\text{C}$ , and (c) $\text{Cu}_{0.85}\text{Zn}_{0.15}/\text{C}$ . . . . .	65
4.4	Raman Spectra of (a) Cu/C, (b) $\text{Cu}_{0.85}\text{Ni}_{0.15}/\text{C}$ , and (c) $\text{Cu}_{0.85}\text{Zn}_{0.15}/\text{C}$ . . . . .	65
4.5	Core level XPS data of (a) C $1s$ , (b) Cu $2p$ , (c) Ni $2p$ , and (d) Zn $2p$ of Cu/C, $\text{Cu}_{0.85}\text{Ni}_{0.15}/\text{C}$ , and $\text{Cu}_{0.85}\text{Zn}_{0.15}/\text{C}$ . . . . .	66
4.6	(a) ECSA of MOF derived nano-catalysts, and BET adsorption-desorption plot of (b) MOFs and (c) MOF derived nano-catalysts Cu/C, $\text{Cu}_{0.85}\text{Ni}_{0.15}/\text{C}$ , and $\text{Cu}_{0.85}\text{Zn}_{0.15}/\text{C}$ . . . . .	67
4.7	(a) LSV curves of electrocatalysts with and without nitrate ions over (a) Cu/C, (b) $\text{Cu}_{0.85}\text{Ni}_{0.15}/\text{C}$ , (c) $\text{Cu}_{0.85}\text{Zn}_{0.15}/\text{C}$ , (d) Ni/C, (e) Zn/C, and (f) Yield of $\text{H}_2$ over the Cu/C, $\text{Cu}_{0.85}\text{Ni}_{0.15}/\text{C}$ and $\text{Cu}_{0.85}\text{Zn}_{0.15}/\text{C}$ . . . . .	68
4.8	Representative GC chromatograms of $\text{H}_2$ from $\text{Cu}_{0.85}\text{Ni}_{0.15}/\text{C}$ after 2 h of chronoamperometric study . . . . .	69
4.9	Representative UV-Vis absorption spectra of (a) nitrate concentration, (a) ammonia formed, and (b) nitrite formed against different potentials over $\text{Cu}_{0.85}\text{Zn}_{0.15}/\text{C}$ . . . . .	70
4.10	The degrees of conversion of $\text{NO}_3^-$ against the applied potentials over (a) over Cu/C, $\text{Cu}_{0.85}\text{Ni}_{0.15}/\text{C}$ , and $\text{Cu}_{0.85}\text{Zn}_{0.15}/\text{C}$ , and (b) Ni/C and Zn/C . . . . .	70

4.11 (a) Yield of $\text{NH}_3$ , (b) Yield of $\text{NO}_2^-$ , and (c) Selectivity of $\text{NH}_3$ over Cu/C, $\text{Cu}_{0.85}\text{Ni}_{0.15}/\text{C}$ , and $\text{Cu}_{0.85}\text{Zn}_{0.15}/\text{C}$ . . . . .	71
4.12 (a) Yield of $\text{NH}_3$ , (b) Yield of $\text{NO}_2^-$ , and (c) Selectivity of $\text{NH}_3$ over Ni/C and Zn/C	71
4.13 The percentage of energy efficiency of formation of $\text{NH}_3$ over over Cu/C, $\text{Cu}_{0.85}\text{Ni}_{0.15}/\text{C}$ , and $\text{Cu}_{0.85}\text{Zn}_{0.15}/\text{C}$ . . . . .	72
4.14 FE(%) of $\text{NH}_3$ , $\text{NO}_2$ , and $\text{H}_2$ over (a) Cu/C, (b) $\text{Cu}_{0.85}\text{Ni}_{0.15}/\text{C}$ , and (c) $\text{Cu}_{0.85}\text{Zn}_{0.15}/\text{C}$	72
4.15 FE(%) of $\text{NH}_3$ , $\text{NO}_2$ and $\text{H}_2$ over (a) Ni/C and (b) Zn/C . . . . .	73
4.16 (a) Impedance spectra and (b) Tafel plots over Cu/C, $\text{Cu}_{0.85}\text{Ni}_{0.15}/\text{C}$ , and $\text{Cu}_{0.85}\text{Zn}_{0.15}/\text{C}$ . . . . .	73
4.17 LSV curves at different scan rates over (a) Cu/C (b) $\text{Cu}_{0.85}\text{Ni}_{0.15}/\text{C}$ and (c) $\text{Cu}_{0.85}\text{Zn}_{0.15}/\text{C}$ . . . . .	75
4.18 (a) Plot of peak current with the square root of scan rate following the Randles-Sevick equation, (b) plot of peak potential ( $E_p$ ) with the log of scan rate, and (c) Arrhenius plotting of the three MOF-derived nano catalysts . . . . .	75
4.19 Plot of the cathodic current against applied potential at different temperatures over(a) Cu/C, (b) $\text{Cu}_{0.85}\text{Ni}_{0.15}/\text{C}$ , and (c) $\text{Cu}_{0.85}\text{Zn}_{0.15}/\text{C}$ . . . . .	76
4.20 (a) Atomic orbital ( $d$ -orbital) projected density of states profiles of pristine Cu/C, $\text{Cu}_{0.85}\text{Ni}_{0.15}/\text{C}$ , and $\text{Cu}_{0.85}\text{Zn}_{0.15}/\text{C}$ (b) adsorption energies for different molecular species adsorptions on pristine Cu/C, $\text{Cu}_{0.85}\text{Ni}_{0.15}/\text{C}$ and $\text{Cu}_{0.85}\text{Zn}_{0.15}/\text{C}$ surfaces, with the adsorption schematics . . . . .	76
4.21 Energy minimized relaxed (111) surfaces of Cu/C, $\text{Cu}_{0.85}\text{Ni}_{0.15}/\text{C}$ , and $\text{Cu}_{0.85}\text{Zn}_{0.15}/\text{C}$	77

# Abbreviations

<b>eV</b>	<b>E</b> lectron volt
<b>keV</b>	<b>K</b> ilo electron volt
<b>mV</b>	<b>M</b> illivolt
<b>V</b>	<b>V</b> olts
<b>mA</b>	<b>M</b> illiampere
<b>A</b>	<b>A</b> mpere
<b>nm</b>	<b>N</b> anometre
<b>μm</b>	<b>M</b> icrometre
<b>cm</b>	<b>C</b> entimetre
<b>cm<sup>3</sup></b>	<b>C</b> ubic centimetre
<b>m</b>	<b>M</b> etre
<b>km</b>	<b>K</b> ilometre
<b>μL</b>	<b>M</b> icroliter
<b>mL</b>	<b>M</b> illiliter
<b>L</b>	<b>L</b> iter
<b>μg</b>	<b>M</b> icrogram
<b>mg</b>	<b>M</b> illigram
<b>g</b>	<b>G</b> ram
<b>T</b>	<b>T</b> emperature
<b>°C</b>	<b>D</b> egree centigrade
<b>K</b>	<b>K</b> elvin
<b>μmol</b>	<b>M</b> icromole
<b>mmol</b>	<b>M</b> illimole
<b>mol</b>	<b>M</b> ole
<b>s</b>	<b>S</b> econds

<b>min</b>	<b>Minutes</b>
<b>h</b>	<b>Hours</b>
<b>Å</b>	<b>Angstroms</b>
<b>°</b>	<b>Degree</b>
<b>mM</b>	<b>Millimolar</b>
<b>M</b>	<b>Molar</b>
<b>W</b>	<b>Watt</b>
<b>kWh</b>	<b>Kilo Watt hour</b>
<b>%</b>	<b>Percentage</b>
<b>ppb</b>	<b>Parts per billion</b>
<b>ppm</b>	<b>Parts per million</b>

# Chapter 1

## NO<sub>x</sub> and its Nefarious Impact

### 1.1 Introduction

In the endeavor to achieve greater ease and well-being, humans have harnessed local resources, transforming them into utilities that augment comfort and convenience thereby fostering a continuous pursuit of novel discoveries, innovations, and technological advancements. Historically, this endeavor extends to the early utilization of coal combustion as an energy source to satisfy the growing demands of evolving technologies. However, this trajectory of progress has been shadowed by the inadvertent generation of environmental pollution, in particular, the universal issue of air pollution continues to challenge the human race [1].

One of the dominant components of air pollution is NO<sub>x</sub>, predominantly consisting of nitric oxide (NO) and a smaller proportion of nitrogen dioxide (NO<sub>2</sub>). Practically all energy production processes worldwide contribute to the emission of NO<sub>x</sub>. Gaseous NO<sub>x</sub> mostly arises from the combustion of fossil fuels, including coal-powered furnaces and diesel engines [2], as well as from biomass combustion [3]. Therefore, emissions of gaseous NO<sub>x</sub> are classified into stationary and mobile sources. Stationary sources [4] encompasses emissions from thermal power plants, industrial boilers, and cement manufacturing facilities. Conversely, mobile sources [5] of NO<sub>x</sub> emissions largely originate from transportation systems, including automobiles, locomotives, airplanes, ships, etc. Over the past few decades, the escalation in the use of automobiles and industrial activities has led to a marked increase in atmospheric concentrations of NO<sub>x</sub> emissions. The chemistry of the troposphere is significantly influenced by NO<sub>x</sub> as the formation of tropospheric ozone increases radically which is the major component of smog. Also, NO<sub>x</sub> in

the atmosphere are captured by the moisture causing acid rain which has an adverse effect on the eco-system like polluting the water bodies. Global statistics reveal that the contribution of  $NO_x$  emissions varies significantly across different world regions. As per the International Energy Agency (IEA) Report 2021 and European Economic Area (EEA) Report 2022, mobile sources are the most significant contributors to  $NO_x$  emissions in India and the European Union countries, accounting for a substantial 40% and 37% of the total for the respective countries (Figure 1.1). In contrast, stationary sources play a major role in China [6], contributing to a significant majority of  $NO_x$  emissions, totaling 71%. These variations highlight the diverse sources and dynamics influencing  $NO_x$  emissions in different regions of the world.

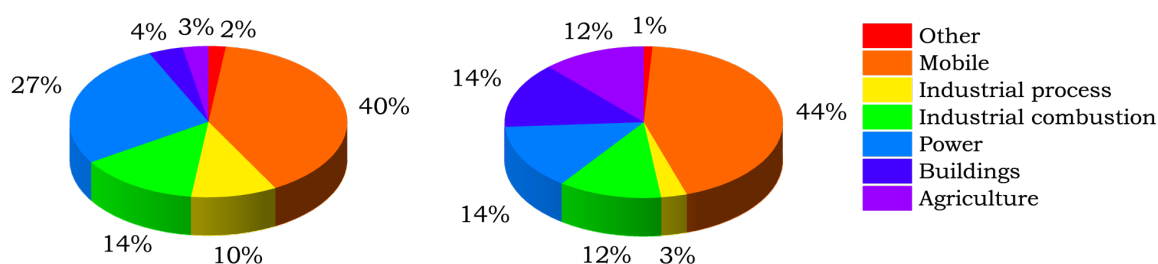
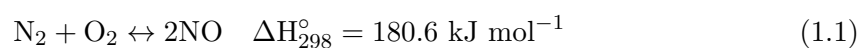


Figure 1.1:  $NO_x$  emission in (a) India in the year 2019 (IEA 2021) (b) Countries in European Union in the year 2022 (EEA Report 2022)

### 1.1.1 Formation of $NO_x$

Generally under normal atmospheric conditions, nitrogen and oxygen do not readily combine. However, when exposed to elevated temperatures, typically above 1000 °C, nitrogen and oxygen undergo chemical reactions leading to the formation of  $NO_x$ . Specifically, nitric oxide (NO) is produced when combustion occurs under lean conditions, characterized by a higher ratio of air to fuel. Conversely, when an excess of oxygen is present, NO can undergo transformation into  $NO_2$ . The intricate mechanisms of  $NO_x$  production during combustion have been extensively studied, with three major mechanisms proposed by Bosch and Janssen [7] to elucidate this process. They are:

1. The first kind, known as thermal  $NO_x$ , is produced when  $N_2$  is subjected to high temperatures and undergoes the oxidation process.



The Zeldovich mechanism [8] of chain reactions involving N\* and O\* activated atoms governs this reaction above 1000 °C:



Reaction (1.3) controls NO generation and tends to rise with temperature. Most engine conditions promote Zeldovich NO formation. Operating the engine under surplus air (fuel-lean) conditions can lower the combustion temperature in order to minimize NO<sub>x</sub> emissions, but most of these methods are ineffective.

2. The second type of NO<sub>x</sub> is referred to as fuel NO<sub>x</sub> [9] and is produced by the oxidation of nitrogen in fuels such as coal and heavy oils. Unlike thermal NO<sub>x</sub>, NO<sub>x</sub> generation is comparatively temperature independent at conventional combustion temperatures.
3. Prompt NO<sub>x</sub>, also known as Fenimore NO [10], is the third type of NO<sub>x</sub> and is formed when hydrocarbon fragments combine with ambient nitrogen to produce compounds like HCN and H<sub>2</sub>CN. The lean zone of the flame is where they can subsequently be oxidized to NO, and also further react with oxygen form NO<sub>2</sub> or N<sub>2</sub>O.

Rapid NO<sub>x</sub> production is independent of the kind of parent hydrocarbon and inversely proportional to the volume of carbon atoms present. With a rise in hydrocarbon radical concentration, more HCN is produced. With low temperatures, fuel abundance, and short residence duration, prompt NO<sub>x</sub> can build in large amounts.

### 1.1.2 Nefarious environmental effect of NO<sub>x</sub> and Consequent Regulations

The emissions of NO<sub>x</sub> from the aforementioned sources exert a range of detrimental effects on both the environment and human health. NO<sub>x</sub> are significant players in the photochemistry of both the troposphere and stratosphere, contributing to adverse consequences. Remarkably, the groundbreaking research of Paul J. Crutzen, Mario J. Molina, and F. Sherwood Rowland, which earned them the Nobel Prize in Chemistry in 1995, shed light on the formation and depletion of the ozone layer by NO<sub>x</sub> [11]. NO<sub>x</sub> emissions are responsible for several hazardous phenomena, including ozone layer depletion, ozone formation in the troposphere, the creation of peroxyacetyl nitrate (PAN), the generation of acid rain, and the amplification of global

warming potential, which contributes to climate change. Additionally, when inhaled at elevated levels, NO<sub>x</sub> can penetrate deep into the lungs, resulting in respiratory diseases such as coughing, dyspnea, wheezing, bronchospasm, and even pulmonary edema [12].

The formation of acid rain from gaseous NO<sub>x</sub> is another substantial concern, affecting ecosystems and organisms. Acid rain occurs when gaseous NO<sub>x</sub> compounds, high above the clouds, transform into HNO<sub>3</sub>, subsequently acidifying rain, fog, and snow due to their high solubility in water. This process has a significant impact on aquatic life and other living organisms. Groundwater containing high nitrate levels can lead to methemoglobinemia (blue baby syndrome) in toddlers and poses a significant carcinogenic risk [13]. The release of nitrates into water bodies also results from intensive agricultural activities, urban settlements, and industrial effluents. According to World Health Organization (WHO) guidelines, the concentration of nitrate in drinking water should not exceed 50 ppm as nitrate ion (equivalent to 11 mg L<sup>-1</sup> as nitrate-nitrogen), and nitrite levels should remain below 0.03 ppm [14].

In response to the environmental and health impacts of NO<sub>x</sub>, governments worldwide have enacted stringent regulations on NO<sub>x</sub> gas emissions as depicted in Figure 1.2. These regulations have been developed through a combination of political, social, and legal processes, with specific emission limits varying from one country to another due to differences in environmental conditions, fuel specifications, and equipment performance. India has adopted a system of emission standards known as Bharat Stage norms, which are equivalent to Euro emission standards for vehicles. Currently, Bharat Stage VI is implemented in the country. The regulatory emission standards are depicted in Figure 1.2. Emission concentration values are typically expressed in parts per million (ppm) or parts per billion (ppb), while emission factors are often measured in grams per kilometer (g km<sup>-1</sup>) or grams per kilowatt-hour (g kW<sup>-1</sup> h<sup>-1</sup>).

Challenged with increasing stringent rules against the emission of NO<sub>x</sub>, it has become paramount importance to create high-performance NO<sub>x</sub> removal methods. The obligation to fulfil NO<sub>x</sub> limits has resulted in the development of a variety of treatment methods. A variety of approaches, such as pre-combustion, combustion, and post-combustion, have been tried in order to reduce emissions of gaseous NO<sub>x</sub> [15]. The pre-combustion approach involves alterations to the design of furnaces and burners within the combustion unit, aimed at regulating temperature, optimizing the air-to-fuel ratio, and adjusting residence time. However, it is important to note that the NO<sub>x</sub> reduction achieved through pre-combustion and combustion procedures often falls below 50% [16]. In contrast, post-combustion methods [17] have proven highly effective and have led



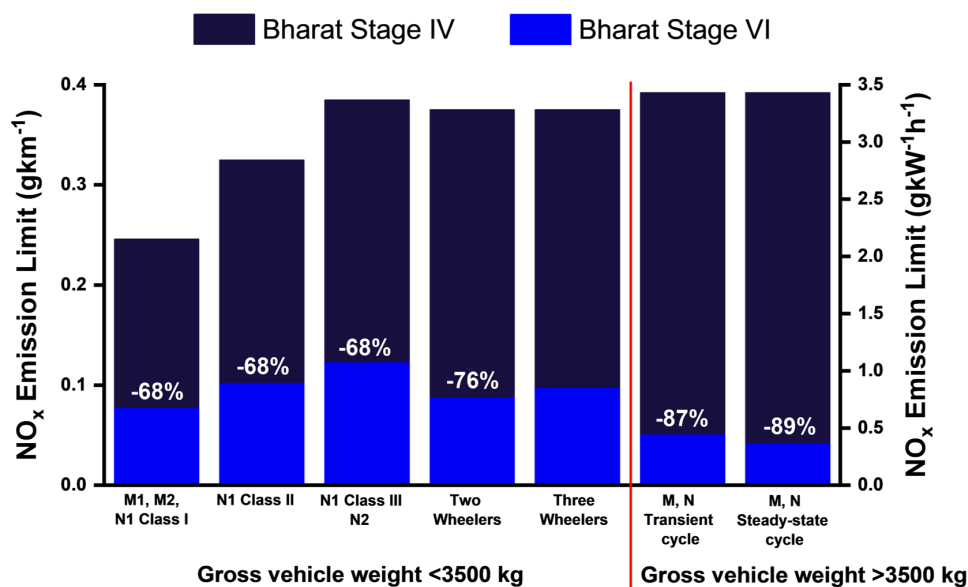


Figure 1.2: Regulatory emission standards implemented in India: Bharat Stage VI

to significant  $NO_x$  reduction rates. These post-combustion procedures include selective catalytic reduction (SCR), selective non-catalytic reduction (SNCR), electrochemical reduction, as well as wet scrubbing, adsorption, electron beam, and non-thermal plasma techniques. When it comes to reducing aqueous  $NO_x$ , conventional biological, physical, chemical, and electrochemical methods are being employed. Among these approaches, electrochemical reduction of nitrate stands out as particularly promising due to its utilization of environmentally friendly electrons as reductants, operation at ambient conditions, and the absence of a need for subsequent treatment [18]. For the efficient elimination of  $NO_x$ , catalysis is one of the techniques used to fulfill the mandated limits. Understanding the characteristic properties of the materials is of utmost importance when developing more efficient catalysts for  $NO_x$  abatement.

## 1.2 Catalysis for deNO<sub>x</sub>ification

$NO$  molecules possess unique electronic configurations, with unpaired  $\pi$  anti-bonding electrons exhibiting paramagnetic properties that offset the effects of  $\pi$  bonding electrons.  $NO$  has a dissociation energy of  $630 \text{ kJ mol}^{-1}$ , a bond order of 2.5, and an inter-atomic distance of 1.15 Å. Its unpaired electron in the  $2p^*$  orbital enables amphoteric bonding, allowing it to interact with surfaces in diverse ways. Despite the thermodynamic instability of gaseous  $NO_x$ , its high activation energy of  $364 \text{ kJ mol}^{-1}$  necessitates catalytic intervention. Intensive research on catalytic de $NO_x$  materials is underway to reduce this activation energy. This endeavor has

garnered significant attention globally, with the catalytic converter market expected to reach USD 73.1 billion by 2025, driving efforts to develop more effective engines and NO<sub>x</sub> procedures [19].

Studies in after-treatment catalyst technologies have identified three primary deNO<sub>x</sub> routes, influenced by mobile and stationary sources. The first involves NO decomposition using catalysts without reductants, but the high activation energy presents challenges. Various materials, including noble metals, zeolites, and metal oxides, have been explored with limited success. SCR is the second method, relying on reductants like H<sub>2</sub>, hydrocarbons, and NH<sub>3</sub> or urea to selectively reduce NO in the presence of oxygen. Urea/ammonia-SCR is commonly used for stationary sources, but its implementation in lean-burn engines presents complexities. The third technology, NO<sub>x</sub> storage and reduction (NSR) [20], captures NO<sub>x</sub> emissions under lean conditions and reduces it by using reducing agents under rich conditions. While NSR is promising for lean-burn vehicles, its mechanisms and interactions remain incompletely understood.

Escaped gaseous NO<sub>x</sub> contributes to acid rain when reacting with water, and consequently mixing with the water bodies leads to contamination with nitrates. The development of an energy-efficient technique to convert nitrate into a useful product is imperative, given the significant nitrate production from intensive agriculture and urban activities. Electrocatalytic reduction of nitrate to ammonia [21] presents a sustainable alternative to the energy-intensive Haber-Bosch process. Challenges include low yield and complex kinetics, but the use of electrons as a reductant, high nitrate solubility in water, and lower bond energy compared to N≡N make it an attractive option.

In subsequent sections, we delve into the current status of gaseous and aqueous deNO<sub>x</sub> catalysis, highlighting ongoing advancements in these crucial fields.

### 1.2.1 Gaseous NO<sub>x</sub>

The conversion of gaseous NO<sub>x</sub> into environmentally benign nitrogen using a catalyst presents a significant challenge, primarily because most abatement technologies discussed earlier are temperature-dependent processes. Among these technologies, NO abatement through decomposition typically requires the highest operating temperatures. Various reducing agents, including CO, NH<sub>3</sub>, urea, CH<sub>4</sub>, hydrocarbons, and H<sub>2</sub>, have been effectively employed for NO<sub>x</sub> reduction [22]. The H<sub>2</sub>-SCR process, first reported by Jones et al. [23], utilized Pt/Al<sub>2</sub>O<sub>3</sub> as a catalyst

and has since garnered increased interest as a means of reducing NO using H<sub>2</sub> as a reductant. Noticeably, in comparison to other reducing agents, H<sub>2</sub> stands out as it necessitates the lowest reaction temperature when employed as a reducing agent. Furthermore, when H<sub>2</sub> reacts with NO<sub>x</sub>, it can be converted into H<sub>2</sub>O without generating secondary pollution. This characteristic makes H<sub>2</sub> a particularly attractive and environmentally friendly choice for NO<sub>x</sub> reduction [24].

Catalysts are the central component system in a deNO<sub>x</sub> catalysis. Noble metal catalysts have exhibited exceptional catalytic activity for NO reduction. Noble metals like Pt, Pd, Rh dispersed on the metal oxides (e.g. CeO<sub>2</sub>, Al<sub>2</sub>O<sub>3</sub>, ZrO<sub>2</sub>, La<sub>2</sub>O<sub>3</sub>, BaO) [25, 26] have been demonstrated as the most class of materials studied for the deNO<sub>x</sub> technology. According to research by Stenger et al., [27], the activity of noble metals Pt, Pd, and Rh supported on Al<sub>2</sub>O<sub>3</sub> in H<sub>2</sub>-SCR followed the order of Pt>Pd>Rh, with Pt exhibiting the highest activity, followed by Pd and then Rh. This high activity of Pt and Pd in the selective catalytic reduction using H<sub>2</sub>-SCR process has made them focal points of discussion and extensive research in the field of precious metal catalysts. The predominance of research on Pt-based catalysts over Pd-based catalysts can be attributed to the superior activity of Pt-based catalysts, particularly at lower temperatures [28]. Pt supported on various metal oxides, including Pt/Al<sub>2</sub>O<sub>3</sub> [29], Pt/SiO<sub>2</sub> [30], Pt/MgO–CeO<sub>2</sub> [31], Pt/TiO<sub>2</sub>–ZrO<sub>2</sub> [32], and Pt/La<sub>0.5</sub>Ce<sub>0.5</sub>MnO<sub>3</sub> [33], have been reported to display high activity for the H<sub>2</sub>-SCR reaction. Additionally, zeolites have served as supports for Pt catalysts, for instance, a study by Yu et al. [34] found that Pt/ZSM-35 exhibited the best catalytic activity among Pt/ZSM-5, Pt/ZSM-35, and Pt/beta, achieving a NO<sub>x</sub> conversion of 80%. Due to the similarity with zeolites, MOFs are also been researched as support material. Xue et al. [35] synthesized Pt/MIL-96(Al) with different loading of Pt by hydrothermal method achieved excellent NO removal activity. The choice of the support materials is as important as choosing the active components. A significant amount of work has been published on discovering the properties and interaction of support materials with the active components [36, 37]. The studies also suggest that the incorporation of active components to the support materials plays a major difference in the overall performance. On the contrary, there is a restriction to the metal's dispersion due to the fact that the minute metal crystallites gradually lose their surface area and form larger agglomerations owing to the bonding that occurs between different types of metals. In addition, noble metals are incapable of reducing the most frequent oxide support, which is Al<sub>2</sub>O<sub>3</sub>, and as a result, Al<sub>2</sub>O<sub>3</sub> does not cause noble metals to become oxidized. Due to the relevance of reducible oxides like CeO<sub>2</sub> in exhaust catalysis, a lot of research effort has been put into finding ways to improve metal dispersion using these materials [38–40] on support materials like metal oxides

(CeO<sub>2</sub>, TiO<sub>2</sub>), perovskites (LaFeO<sub>3</sub>, BaCeO<sub>3</sub>), MOFs, Zeolites etc.

However, due to their high cost and limited availability, researchers are exploring alternative, non-noble metal catalysts. Developing non-noble metal catalysts, especially those achieving high N<sub>2</sub> selectivity and operating within a low-temperature range, presents significant challenges. The physicochemical properties of catalysts can be influenced by several factors, including their synthesis method, composition, and heat treatment processes such as calcination and reduction. Consequently, the characteristics of catalysts vary depending on their type and the specific conditions under which they are prepared and used. In the quest for cost-effective catalysts for NO<sub>x</sub> reduction, researchers have investigated materials such as metal oxides, zeolites, metal supported on metal oxide, perovskite, binary oxides, MOFs, and mullites. Non-noble metal catalysts possess unique catalytic characteristics and reactivity profiles that can be customized or tailored to suit specific reaction processes [41]. This adaptability makes them valuable alternatives to noble metal catalysts in various applications. Wang et al. [42] synthesized ordered mesoporous Cu-based catalyst supported on ceria doped with Fe, Mn, and Co. It was observed that CuCo/CeO<sub>2</sub> exhibited outstanding performance against NO reduction within the temperature range of 200 to 400 °C. Researchers attributed the superior efficiency in converting NO<sub>x</sub> to CuCo/CeO<sub>2</sub>, which is due to the presence of CoO<sub>x</sub> species on the catalyst's surface. These species effectively reduced Ce<sup>4+</sup> to Ce<sup>3+</sup>, resulting in the creation of additional oxygen vacancies. Väliheikki et al. [43] conducted a study on the effectiveness of W-promoted CeO<sub>2</sub>-ZrO<sub>2</sub> solids for NO<sub>x</sub> reduction. They utilized two catalysts with compositions as Zr-rich composition and Ce-rich composition designated as W-ZrCe and W-CeZr respectively. The research findings revealed that the W-ZrCe catalyst exhibited impressive NO<sub>x</sub> conversion rates ranging from 30% to 55%, along with N<sub>2</sub> selectivity between 85% and 92% at temperatures ranging from 250 to 350 °C demonstrated promising catalytic efficiency in reducing NO<sub>x</sub> emissions. Luo et al. [44] prepared by series of LaNi<sub>1-x</sub>Fe<sub>x</sub>O<sub>3</sub> perovskite catalysts with varying Fe content (x = 0.0, 0.2, 0.4, 0.7, and 1.0) using the sol-gel method. The research indicated that the addition of Fe into LaNiO<sub>3</sub> resulted in improved efficiency in NO<sub>x</sub> removal and increased stability of the perovskite structure. This enhanced activity can be primarily attributed to the facilitated reduction of Ni<sup>3+</sup> to Ni<sup>2+</sup> with the assistance of an appropriate Fe component.

### 1.2.2 Aqueous NO<sub>x</sub>

The interaction of atmospheric gaseous NO<sub>x</sub> with moisture or rainwater leads to its incorporation into water bodies, thereby introducing nitrate into aquatic life and impacting their ecosystem. This transformation holds considerable significance for the overall quality of water within these ecosystems, with far-reaching implications for their ecological health and balance. In response to the WHO target, various technologies have been developed for reducing nitrate content in drinking water. These technologies encompass biological denitrification [45], chemical/catalytic reduction [46, 47], ion-exchange/reverse osmosis [48], electrodialysis [49], among others. However, due to the high operating and maintenance costs for these removal systems, electrochemical nitrate reduction [50] stands out as the process utilizes only a compact installation footprint and mild operational conditions, positioning it as a promising decentralized denitrification technique. The ability to implement detailed control over the selectivity towards desired products holds considerable influence over the economic viability of nitrate reduction reaction. Markedly, the production of ammonia through this process can find application as fertilizer or in the production of fuels and chemicals, thus generating revenue i.e., turning waste into wealth.

The design and development of electrocatalytic materials with both high activity and selectivity are critical in the electrochemical reduction of nitrate. Various types of materials have been explored, including noble metals (such as Pt, Pd, Ir, Ru, and Rh) [51], transition metals (such as Cu, Sn, Fe, In, Co, Ni, and Ti) [52], as well as bimetallic species (including Cu<sub>2</sub>O–Cu@Ti and CuPd) alloys [53], single-atom catalyst (SAC) (like Cu-SAC, Fe-SAC) [54]. Among the transition metals, Cu and Cu-based catalysts [55] have emerged as highly promising candidates for the selective and active electrochemical reduction of nitrate to ammonia. This has generated significant attention in the scientific community, emphasizing the efforts to enhance the catalytic activity of Cu through various strategies.

Qin et al. [56] conducted research into the reactivity of different exposed facets of Cu<sub>2</sub>O electrocatalysts and found that the Cu (100) facet exhibited higher ammonia (NH<sub>3</sub>) yields compared to the Cu (111) facet. Fu et al. [57] studied the Cu nanosheets under environmental conditions and achieved an impressive NH<sub>3</sub> production rate and the Faradaic Efficiency (FE). The outstanding performance of Cu (111) nanosheets in nitrate reduction is ascribed to their ability to suppress the competing hydrogen evolution reaction (HER). The dual atom Cu-Ni SAC prepared by Wang et al. [58] exhibited remarkable performance when compared to individual Cu-NC and Ni-NC catalysts. It achieved a maximal NH<sub>3</sub> FE and a yield rate which is credited

to the presence of active centers of both Cu and Ni. Qiao et al. [59] designed an electrocatalyst featuring B-rich core-shell nickel boride nanoparticles, denoted as Ni<sub>3</sub>B@NiB<sub>2.74</sub>. This innovative electrocatalyst demonstrated exceptional performance and delivered a significant yield of NH<sub>3</sub>. Shou et al. [60] synthesized Co-doped Fe-MOF-74 derived Co-Fe@Fe<sub>2</sub>O<sub>3</sub> catalyst, where Co replaced some Fe sites within the Fe<sub>2</sub>O<sub>3</sub> structure. The catalyst exhibited notable catalytic activity and selectivity for the electrochemical reduction of nitrate ions to produce NH<sub>3</sub>. A mechanistic investigation unveiled that the superior catalytic performance of Co-Fe@Fe<sub>2</sub>O<sub>3</sub> could be attributed to the presence of Co as a dopant, which influenced the Fe *d* orbitals, resulting in alterations in the adsorption energy of intermediates and the free energies of the potential dependent step, while concurrently suppressing the competing HER.

### 1.3 Scope and objective of the work

Ongoing research and development in the realm of deNO<sub>x</sub> catalysis are yielding innovative catalyst designs. Presently, a significant challenge in this field revolves around the improvement of catalyst performance from lower to higher temperatures, all while maintaining selectivity and efficiency and stability at higher temperatures. In terms of energy and environmental aspects, understanding the reaction mechanism of catalyst and reactant at the molecular level is one of the challenges to unravel. The promising research avenues in this domain involve the exploration and development of novel catalysts that exhibit superior capabilities for NO<sub>x</sub> removal. Certainly, synthetic approaches hold noteworthy importance as they exert extensive influence over factors such as surface area, particle size, and the overall structure of the synthesized materials. The optimization of preparation conditions stands as a crucial step towards enhancing the performance of these materials. Moreover, efforts to develop effective methods and materials for improving the recyclability of catalysts are vital for sustainability. This can contribute to reducing waste and enhancing the economic feasibility of catalytic processes. In addition, the design of reactors that are both cost-effective and user-friendly is imperative for practical application in various industries.

For the electrocatalytic reduction reaction, the strategies employed often revolve around two key objectives: either fine-tuning the adsorption of reactants and intermediates or enhancing proton-electron transfer processes. To accomplish these objectives, it is imperative to gain an in-depth understanding of the intricate reaction pathways involved. Several parameters such as electronic structure and chemical composition, the geometry of the catalyst, promotion of

the active sites, pH of the electrolyte, recyclability, stability, and suppression of HER are very important for the high FE, selectivity, and better yield of the product. It is essential to tune the *d*-band center and surface potential of the catalyst to control the adsorption of reactants and intermediates. These factors play a pivotal role in influencing how reactants and intermediates interact with the catalyst surface. When the catalyst's active sites exhibit a high proton affinity, it can lead to a dominance of the competing HER on a significant portion of the active sites. Therefore, achieving the desired catalytic outcomes involves precisely adjusting the coverage of adsorbed hydrogen species ( $H_{ad}$ ) by carefully regulating the electronic structure of the catalyst. Based on the identified gaps in the existing literature, the objectives of this thesis encompass several key aspects related to thermal and electrocatalytic  $NO_x$  reduction and catalyst development. They include:

- Designing and developing novel, high-performance materials using innovative synthesis routes for the catalytic reduction of  $NO_x$ .
- Effectively dispersing active catalytic sites on materials with high surface areas to optimize catalytic activity.
- A comprehensive investigation of the structure-property relation of the synthesized materials to gain a deep understanding of the reaction mechanisms involved and the catalytic roles played by the materials, with a focus on establishing structure-property relationships.
- In-depth study of the catalytic reduction of  $NO_x$ , including the determination of kinetic parameters and the enhancement of  $NO_x$  conversion and product selectivity. Researching and identifying improved support materials and dopants to suppress HER that can enhance electrocatalytic performance.

These objectives collectively aim to contribute in catalyst development for thermal and electrocatalytic  $NO_x$  reduction, with a focus on achieving higher efficiency and selectivity in  $NO_x$  conversion processes into eco-friendly and value-added products. As advancements in technology persist, catalytic  $deNO_x$  techniques will continue to play a pivotal role in the ongoing pursuit of a cleaner, healthier, and more sustainable world.

To achieve the mentioned goals, we have worked on investigating different materials. The thesis covers the catalytic reduction of  $NO_x$  by thermal and electrocatalytic processes. Chapter 2 focuses on the dispersity, porosity, and surface area of the support material utilizing noble metal

---

as an active site for the low temperature gaseous NO<sub>x</sub> reduction. For the cost-effective route, we have studied non-noble material as the catalyst in Chapter 3. The active site is clearly addressed by investigating the synthesized catalyst in different routes. The detailed mechanism of the reaction and kinetic parameters are also studied with the help of experimental and computational methods. Chapter 4 deals with the reduction of aqueous NO<sub>x</sub> into a value-added product by indulging electrocatalytic reduction method by manipulating the electronic structure and studied the active site for suppressing the HER. The overall aspect of the study is concluded in Chapter 5.



## Chapter 2

# Low temperature catalytic reduction of NO over porous Pt/ZIF-8

### 2.1 Introduction

A plethora of literature is available on finding better deNO<sub>x</sub> materials [7, 61, 62]. Oxidic materials starting from rare earth oxides like CeO<sub>2</sub> [63, 64], ZrO<sub>2</sub>, transition metal oxides like TiO<sub>2</sub> [65, 66], Fe<sub>2</sub>O<sub>3</sub>, V<sub>2</sub>O<sub>5</sub>, WO<sub>3</sub> [67, 68], MnO<sub>x</sub> [69], Al<sub>2</sub>O<sub>3</sub> or their composites [70, 71] have been extensively studied for deNO<sub>x</sub> catalysis. The primary theme of these works has been to enhance the surface area and porosity of the oxidic support, and high dispersion of the active sites over the support for deNO<sub>x</sub> application. Mostly, noble metals are studied as active sites because of their high oxidizing and reducing powers [72–75].

With a very high porosity and high surface area, the zeolitic imidazolate frameworks (ZIFs), a subcategory of metal-organic framework materials have recently attracted significant attention from researchers [76–78]. ZIFs consist of transition metal ions and an imidazolate framework, where the metals play the role of silicon and the imidazolate anions form bridges that mimic the role of oxygen as in zeolites. Among the wide varieties of ZIFs, ZIF-8 with a sodalite topological structure demonstrated potential usage in different applications like gas storage and separation, electro- and photocatalysis, and chemical sensing, and has been at the forefront of scientific studies [79–83]. In ZIF-8, Zn<sup>2+</sup> is the metal ion with the 2-methyl imidazolate (HmIm) corner-sharing tetrahedral linker (Zn(HmIm)<sub>2</sub>) crystallizes in  $I\bar{4}3m$  cubic space group and possesses large cavity of  $\sim 11.6$  Å connected by the six-membered ring windows with the

aperture of  $\sim 3.4$  Å. Due to this large porosity, ZIF-8 owns a very high surface area and also shows high thermal and chemical stability. And therefore, here we choose ZIF-8 as support material and disperse noble metal Pt on the ZIF-8 surface as active sites for the catalytic  $\text{NO}_x$  reduction. Adsorption is a primary step before any catalytic reactions, and the surface basic imidazolate units may help to adsorb the NO on the surface. This will be an added advantage for the catalytic efficacy of Pt/ZIF-8 for NO reduction. To compare the catalytic performance, Pt/zeolite Y was considered as a benchmark material. The ammonium ion-exchanged zeolite  $\text{NH}_4\text{-Y}$  with faujasite topology was chosen due to the presence of basic  $\text{NH}_4^+$  groups in its surface mimicking imidazolate units in ZIF-8. Though there are discrete reports on the utilization of some metal-organic frameworks for  $\text{NO}_x$  adsorbent [84], to our knowledge, this is the first report of NO reduction over Pt/ZIF-8.

## 2.2 Materials and Methods

### 2.2.1 Synthesis of Catalysts

Zinc nitrate hexahydrate ( $\text{Zn}(\text{NO}_3)_2 \cdot 6\text{H}_2\text{O}$ ), ammonium hydroxide ( $\text{NH}_4\text{OH}$ ) and hydrazine hydrate ( $\text{N}_2\text{H}_4 \cdot \text{H}_2\text{O}$ ) were purchased from S D Fine Chem. Ltd. 2-methylimidazole (HmIm) and chloroplatinic acid hexahydrate ( $\text{H}_2\text{PtCl}_6 \cdot 6\text{H}_2\text{O}$ ) were procured from Sigma Aldrich. Zeolite Y was purchased from Alfa Aesar and was used as procured without any additional treatment. For ZIF-8 synthesis,  $\text{Zn}(\text{NO}_3)_2 \cdot 6\text{H}_2\text{O}$  and HmIm were used as metal precursor and linker, respectively and molar ratio between metal and linker was kept as 1:10. The metal and the linker solutions were separately made of 0.594 g of  $\text{Zn}(\text{NO}_3)_2 \cdot 6\text{H}_2\text{O}$  (1.996 mmol) and 1.63 g HmIm of (19.96 mmol) with of water and  $\text{NH}_4\text{OH}$ . Both the solutions were mixed with a magnetic stirrer for 15 min at 730 rpm for complete dissolution. Then the resultant solution mixture was heated up to 120 °C for 30 min with a ramp rate of 10 °C  $\text{min}^{-1}$  in a conventional heating oven. The obtained solid suspension was filtered, washed several times with deionized water, and dried at 70 °C for 12 h in a hot air oven. The white-colored solid product was ZIF-8. 1 wt.% Pt loaded ZIF-8 was synthesized by using the wet impregnation method. For the synthesis of 1% Pt loaded ZIF-8, 10.64 mg of  $\text{H}_2\text{PtCl}_6 \cdot 6\text{H}_2\text{O}$  was dissolved in 10 mL of water, 400 mg of ZIF-8 was added to the above solution, and was stirred vigorously for 15 min. An equivalent amount of hydrazine hydrate was added dropwise to this suspension, and stirring was continued for 2 h. The resultant solution was filtered, washed, and dried at 70 °C for 12 h in a hot air oven.

The obtained solid powder was 1% Pt/ZIF-8. For the synthesis of 1% Pt/zeolite Y similar wet impregnation procedure was followed.

### 2.2.2 Characterizations

The structural characterization of the synthesized materials was carried out with Rigaku Ultima IV X-ray diffractometer with Cu K $\alpha$  radiation ( $\lambda=1.5418 \text{ \AA}$ ) at a scan rate of  $1^\circ \text{ min}^{-1}$  with step size of  $0.01^\circ$  to record the X-ray diffraction pattern (XRD). The average crystallite size (D) was estimated using Scherrer's formula:  $D=0.9\lambda/\beta\text{Cos}\theta$ , where  $\lambda$  is the wavelength of the radiation,  $\beta$  is fullwidth at half-maximum, and  $\theta$  is the corresponding angle. Temperature-dependent *in-situ* XRD was used to evaluate the structural stability of the synthesized materials at elevated temperatures by heating the samples from 30 to 600  $^\circ\text{C}$  at  $10^\circ\text{C min}^{-1}$  under vacuum, and the patterns were recorded at a scan rate of  $1^\circ \text{ min}^{-1}$  with a step size of  $0.01^\circ$ . Thermogravimetric analysis (TGA) was used to study the effect of temperature on the synthesized materials and was performed using a Shimadzu DTG-60 from 30 to 900  $^\circ\text{C}$  temperature with a heating rate of  $10^\circ\text{C min}^{-1}$  under N $_2$  atmosphere.

Thermo Scientific K-ALPHA surface analysis spectrometer with X-ray source of Al K $\alpha$  radiation (1486.6 eV) was used to record X-ray photoelectron spectra (XPS) of the synthesized catalysts. Binding energies are reported with respect to C 1s at 284.8 eV. The surface morphology of the synthesized materials was studied by using Field Emission Scanning Electron Microscopy (FE-SEM, FEI-ApreoS) and high-resolution transmission electron microscopy (HR-TEM) (JEOL, JEM 2100). Microtrac BEL Corp mini-II surface area analyzer was used for measuring the surface area and pore size distribution of the synthesized materials. N $_2$  adsorption-desorption isotherms were measured at -196  $^\circ\text{C}$ . Prior to the sorption measurements, samples were degassed in vacuum at 300  $^\circ\text{C}$  for 1 h. Temperature programmed desorption (TPD) unit (from Mayura Analytical Private Limited, India) housing a thermal conductivity detector (TCD) was used for NO-TPD and H $_2$ -temperature programmed reduction (H $_2$ -TPR) studies over the synthesized catalysts.

The TPD unit contains a gas handling unit with a flow meter to monitor the flow of the gases, a controller, a furnace with a temperature programmer, and a data acquisition system. 100 mg of catalyst with 40–80 mesh size was packed in a continuous flow quartz micro-reactor with ceramic wool. The flow rate of NO was set at  $30 \text{ cm}^3 \text{ min}^{-1}$ . The NO was adsorbed on the catalyst for 45 min and desorption of NO was carried out by increasing the temperature from 30 to 400

$^{\circ}\text{C}$  with ramping of  $10\text{ }^{\circ}\text{C min}^{-1}$ . Prior to each experiment, the catalysts were degassed in He gas flow to minimize the contribution from the physisorbed species. The desorption profile of NO was recorded by TCD detector. For  $\text{H}_2$ -TPR experiments, 5 vol%  $\text{H}_2/\text{He}$  was passed over the 100 mg of catalyst with a total flow rate of  $30\text{ cm}^3\text{ min}^{-1}$ , and the temperature was raised from 30 to  $400\text{ }^{\circ}\text{C}$  with ramping of  $10\text{ }^{\circ}\text{C min}^{-1}$ . To probe the adsorbed NO species on the catalysts surface Fourier-transform infrared spectroscopy (FT-IR) was performed. The samples were made into pellets with KBr and  $10\text{ }\mu\text{L}$  of saturated  $\text{NaNO}_2$  solution was drop casted onto it. The FT-IR spectra of the pristine and  $\text{NaNO}_2$  adsorbed pellets were recorded with JASCO FT-IR-4200.

### 2.2.3 Catalytic Reduction of NO

For the NO reduction reaction, the synthesized catalysts were packed in the center of a micro-reactor (made of quartz tube of 4 mm diameter) by placing glass wool before and after the catalyst sample, and the reactor was inserted into a tubular furnace heated to the required reaction temperature through a temperature controller. A schematic of the reactor set-up is shown in Figure 2.1. The reaction temperature was measured by a chromel-alumel thermocouple dipped in the catalyst bed. 1:1 vol.% of NO/He and  $\text{H}_2/\text{He}$  gases were released from the cylinders

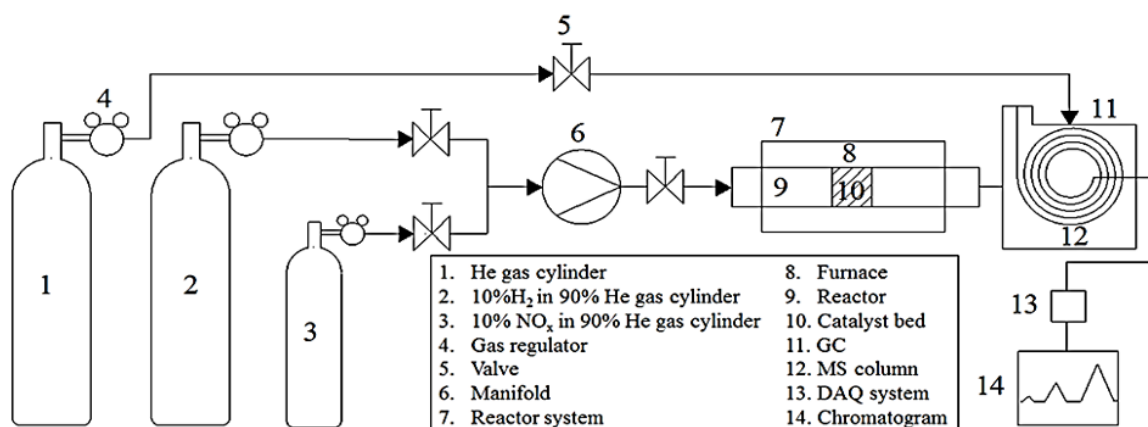


Figure 2.1: Schematic diagram of catalytic reactor

and the flow rate was measured by bubble flow meter. The total flow rate ( $\vartheta_f$ ) was  $30\text{ cm}^3\text{ min}^{-1}$  with the gas hourly space velocity (GHSV) of  $18,000\text{ h}^{-1}$ . The GHSV was calculated by using

the following formula:

$$\text{GHSV} = \frac{\text{Flow rate of gas passing through the reactor } (\vartheta_f) (\text{cm}^3 \text{ min}^{-1})}{\text{Volume of catalyst placed at the reactor bed } (\vartheta_w) (\text{cm}^3)} \quad (2.1)$$

where,  $\vartheta_w = \pi \times \text{length of the bed} \times (\text{radius of the bed})^2$ . All the gases were procured from M/S Bhuruka Gases Ltd., India with 10 vol.% NO in He, 10 vol.% H<sub>2</sub> in He, in this study. The outlet of the micro-reactor was connected to an auto-sampler of online gas chromatography (DGA I, Mayura Analytical Private Limited, India) to detect the product(s) during reduction. The gas chromatograph's oven, injector, and detector were kept at a constant temperature of 60 °C. The initial rate of the reaction was calculated with the formula: NO conversion ( $\mu\text{mol}$ )/(Time (s) x weight of catalyst (g)).

## 2.3 Results and Discussion

The X-ray diffraction (XRD) patterns in Figure 2.2(a) show the crystallinity and structural information of the ZIF-8 and Pt/ZIF-8. ZIF-8 and 1% Pt/ZIF-8 crystallized in phase pure body-centered cubic lattice with space group  $I\bar{4}3m$  [85, 86]. There was no Pt diffraction peak observed in the XRD pattern of 1% Pt/ZIF-8 concluding a very high dispersion of Pt over ZIF-8. The obscured reflection of Pt over ZIF-8 due to the very high dispersion of the metal is also reported in literature [87]. The XRD patterns of zeolite Y and 1 % Pt/zeolite Y are shown in Figure 2.2(b). The presence of sharp peaks validates the high crystalline nature of zeolite Y. 1% Pt/zeolite Y, however, showed a significant peak at 40° corresponding to Pt (111) peak suggesting agglomeration of Pt particles on zeolite Y surface. The average crystallite size of ZIF-8 and 1% Pt/ZIF-8 estimated using Scherrer's formula was found to be in the range of 50-55 nm, whereas zeolite Y and 1% Pt/zeolite Y samples showed an average crystallite size of 35-40 nm. As NO<sub>x</sub> reduction takes place at elevated temperatures, the thermal stability of the materials was examined by TGA and temperature-dependent *in-situ* XRD. Figure 2.2(c) shows the TGA profile of synthesized materials. ZIF-8 and 1% Pt/ZIF-8 showed initial weight loss of ~15% around 150 °C, which might be due to the removal of unreacted guest organic imidazole ligands [83]. With further heating till 500 °C, ZIF-8 gradually lost weight of ~20%, whereas Pt/ZIF-8 remained stable under the experimental conditions. Apparently, Pt loading enhanced the thermal stability of ZIF-8 compared to the pristine sample. There was sharp weight loss above 500 °C over both the samples, which could correspond to the combustion of organic

framework resulting in ZnO. On the other hand, both zeolite Y and 1% Pt/zeolite Y showed a similar amount ( $\sim 25\%$ ) of weight loss at lower temperature region and no further weight loss at elevated temperatures till 900 °C. The presence of Pt on zeolite Y did not show any additional

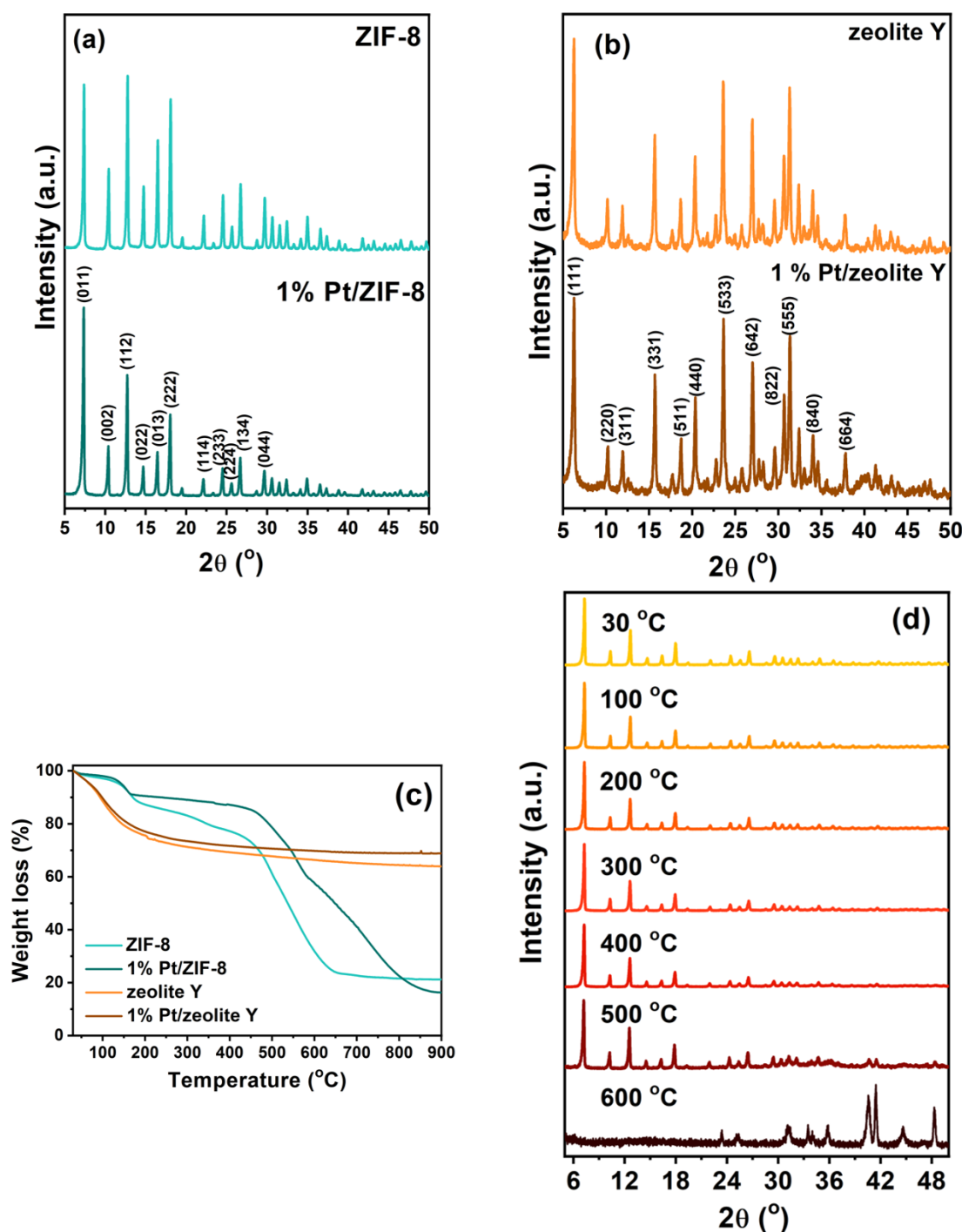


Figure 2.2: XRD profiles of (a) ZIF-8 and 1% Pt/ZIF-8, (b) zeolite Y and 1% Pt/zeolite Y, (c) TGA profiles of the synthesized catalysts, and (d) Temperature-dependent *in-situ* XRD profile of 1% Pt/ZIF-8

thermal stability like ZIF-8. The results indicate that the materials are stable enough for low temperature application. To further probe this result, temperature-dependent *in-situ* XRD was performed on 1% Pt/ZIF-8 (Figure 2.2(d)). The plot shows 1% Pt/ZIF-8 was stable up to 500 °C with a slight shifting of the peaks towards a lower angle indicating thermal expansion of the lattice parameters, as also reported from earlier publications [83, 88]. However, the thermal conversion of ZIF-8 to ZnO took place above 500 °C. This corroborates with the TGA findings.

The reduction of NO by H<sub>2</sub> was carried out with an equimolar mixture of 1:1 vol.% of NO and H<sub>2</sub> over Pt dispersed and pristine ZIF-8 and zeolite Y. A high concentration of NO and H<sub>2</sub> was used to demonstrate the activity of these catalysts even at high concentration, and the reactions were carried from room temperature to 110 °C (which is well within the thermal stability of the materials). The light-off curves for NO conversions are plotted against rising temperature in Figure 2.3. The pristine ZIF-8 showed a very poor conversion. Only 6% of the feed NO was reduced over pristine ZIF-8 within the experimental temperature window. Interestingly, with 1% Pt/ZIF-8, there was complete conversion of NO, and 100% NO conversion was achieved within

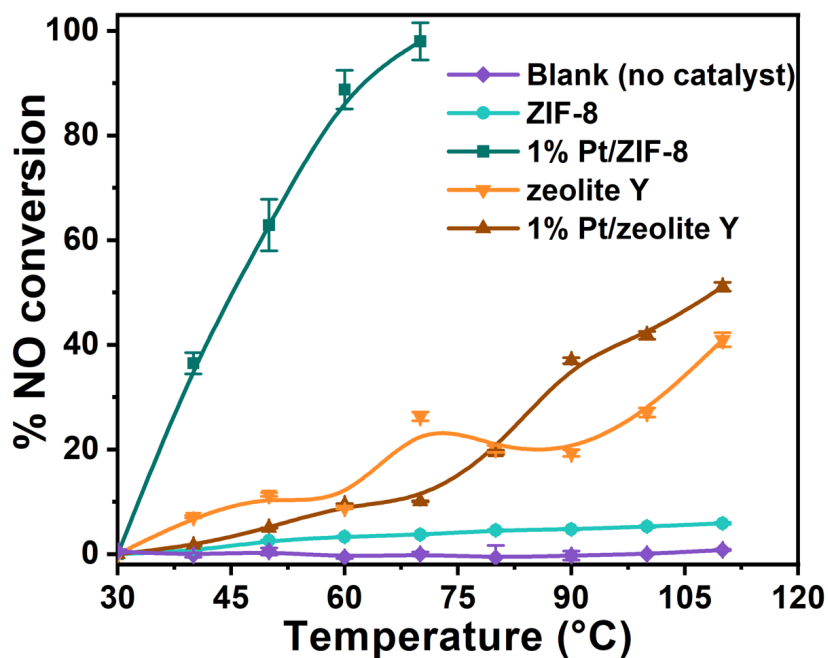


Figure 2.3: The reduction of NO by H<sub>2</sub> over the synthesized catalysts with equimolar mixture of 1:1 vol.% NO and H<sub>2</sub>

as low as 70 °C only. Evidently, Pt dispersion has significantly enhanced the catalytic efficacies of ZIF-8. The initial rate of NO reduction over 1% Pt/ZIF-8 was found to be  $0.24 \mu\text{mol g}^{-1} \text{s}^{-1}$ . On the contrary, Pt dispersion over zeolite Y did not make any significant change in the surface

of the pristine zeolite. NO conversion over zeolite Y and 1% Pt/zeolite Y was only 40 and 50%, respectively at 110 °C. This clearly suggests that either the nature of active sites of Pt over ZIF-8 and zeolite Y are different, or the unique interaction of the metallic active site Pt with the support ZIF-8 might have facilitated the reduction at a very low temperature. The interaction of NO with the Pt modified surface could also have played a significant role in lowering the  $T_{50}$  temperature of NO reduction over 1% Pt/ZIF-8.

To understand the surface interaction of NO with the catalysts, we have performed the NO-TPD experiments over all four catalysts (Figure 2.4(a)). The NO-TPD is one of the most conventional methods for understanding the surface sites for adsorption. The low temperature peak suggests a weak adsorption site, whereas the high temperature desorption peak suggests a strong NO adsorption site in the TPD profile. There is one major peak at 130 °C, and one minor peak at 300 °C of NO desorption over pristine and Pt-loaded zeolite Y, suggesting two different adsorption sites over zeolite Y. Apparently, Pt dispersion over pristine zeolite Y marginally increased the NO adsorption. On the contrary, Pt dispersion over ZIF-8 remarkably increased the NO adsorption as evidenced by the intensity of the low temperature peak getting doubled. A couple of other distinguishable differences between the ZIF-8 and zeolite Y catalysts observed are

1. NO adsorption sites are stronger over ZIF-8 than zeolite Y as the corresponding peaks are at elevated temperatures than zeolite Y
2. NO adsorption sites are more in number over ZIF-8 than zeolite Y as there are more than two peaks are observed in ZIF-8

The stronger and more number of adsorption sites for acidic NO over ZIF-8 surface could be due to the basic imidazolate units, which are absent on the zeolite surface. The NO-TPD results can be easily correlated with the light-off profiles of NO reduction. NO reduction could take place at such a low temperature over Pt/ZIF-8 as it possessed enormously higher NO adsorption sites than the pristine ZIF-8. On the other hand, Pt dispersion over zeolite Y did not influence either the NO adsorption or reduction. The high NO adsorption as well as low temperature reduction could be due to the particular nature of active Pt sites, or the unique interaction of the Pt with ZIF-8. Another factor that may determine the higher catalytic activity of Pt/ZIF-8 is facile  $H_2$  dissociation over the Pt-supported catalyst surface. The facile catalytic  $H_2$  dissociation would bring down the activation energy of the  $NO+H_2$  reaction and consequently would lower



the  $T_{50}$  temperature of NO reduction. Therefore, we have performed the  $H_2$ -TPR over the synthesized catalysts from room temperature to 400 °C, and the corresponding profile is plotted in Figure 2.4(b). Apparently, there is a substantial difference in the  $H_2$ -TPR peak maxima. The 1% Pt/ZIF-8 showed maxima only at 97 °C, whereas 1% Pt/zeolite Y showed it at 197 °C. The result indicates that the gaseous  $H_2$  is easily dissociated over Pt/ZIF-8 compared to that of Pt/zeolite Y, and this made Pt/ZIF-8 a lower temperature superior catalyst towards NO reduction.

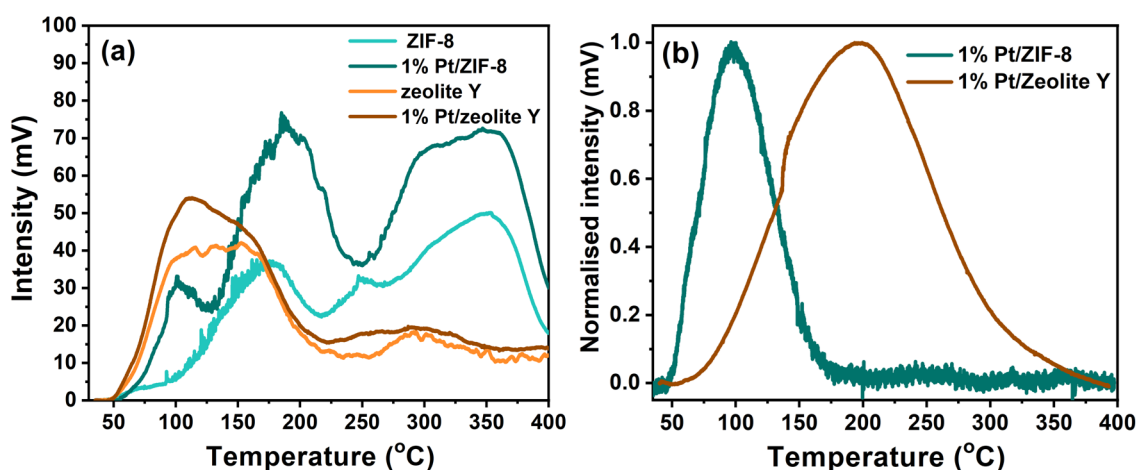


Figure 2.4: (a) NO-TPD profiles of the synthesized catalysts and (b)  $H_2$ -TPR profiles of 1% Pt/ZIF-8 and 1% Pt/zeolite Y

Next, we probed the surface of the synthesized catalysts thoroughly. The surface morphologies of the synthesized catalysts are shown in Figure 2.5. The micrographs of ZIF-8 (Figure 2.5(a)) and 1% Pt/ZIF-8 (Figure 2.5(b)) showed truncated cubes of ZIF-8 with average particle sizes of 350 nm. In 1% Pt/ZIF-8, the Pt particles were found finely and uniformly distributed over ZIF-8 cubes with an average size of 25 nm (Figure 2.5(c)). The remarkable increase in NO adsorption and reduction over Pt/ZIF-8 compared to ZIF-8 could be due to this very high dispersion of the fine Pt nanoparticles over ZIF-8 as revealed by the bright field TEM image in Figure 2.5 (c) and (d) and also on the edge of the truncated cubes of ZIF-8. The STEM-EDS mapping confirmed the 0.97% of Pt on ZIF-8. On the contrary, zeolite Y samples showed spherical particles, which are constructed by small flakes (Figure 2.5(e)). In the case of Pt/zeolite Y, the Pt particles are distributed over zeolite Y spheres (Figure 2.5(f)), however, the sizes of the surface Pt particles were found to be  $\sim 250$  nm, which is 100 times higher when compared to the Pt in Pt/ZIF-8. Due to this agglomerated particles of Pt in Pt/zeolite Y, showed a significant peak at  $2\theta=40^\circ$  in

XRD profiles as seen from Figure 2.2(c). The high distribution of Pt over ZIF-8 was further probed by STEM-EDS mapping in Figure 2.6.

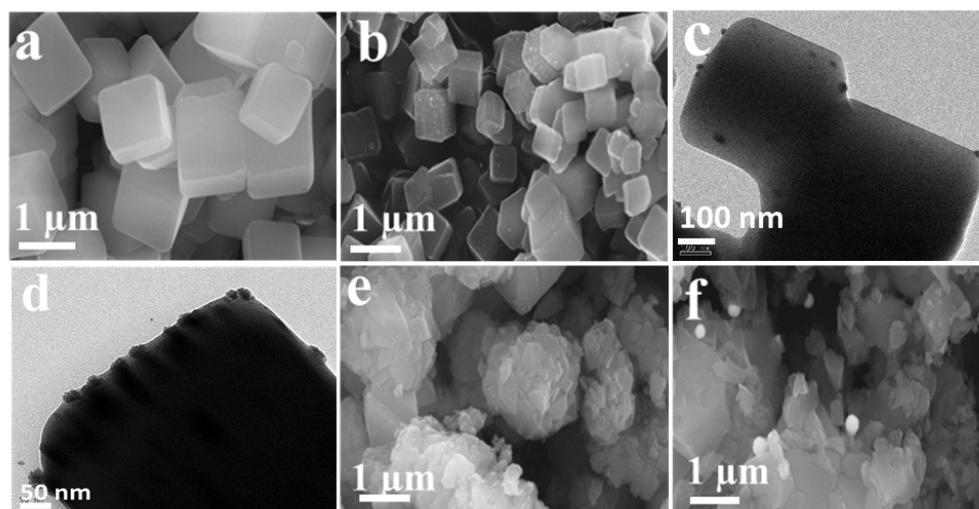


Figure 2.5: FE-SEM images of (a) ZIF-8, (b) 1% Pt/ZIF-8, (e) zeolite Y, (f) 1% Pt/zeolite Y, and (c,d) HR-TEM images of 1% Pt/ZIF-8

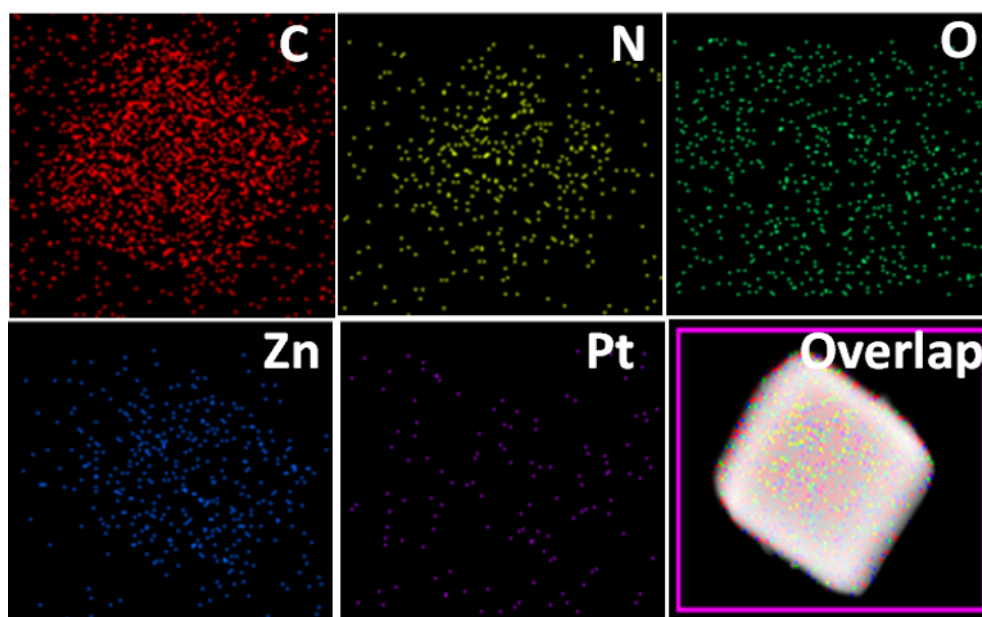


Figure 2.6: STEM-EDS mapping of 1% Pt/ZIF-8

The electronic nature of this surface active sites of Pt and other metallic sites like Zn and Al were explored by XPS, and the results are plotted in Figure 2.7. The core level spectra of Zn in ZIF-8 and 1% Pt/ZIF-8 showed two peaks at 1021 and 1044 eV corresponding to  $2p_{3/2}$  and  $2p_{1/2}$  of  $Zn^{2+}$ . In 1% Pt/ZIF-8, the Pt core level spectrum after deconvolution showed two peaks

confirming the existence of Pt(0) with respect to corresponding binding energies. Thus Zn is in 2+ oxidation and Pt is in zero valent metallic state in ZIF-8 samples. In the case of zeolite Y

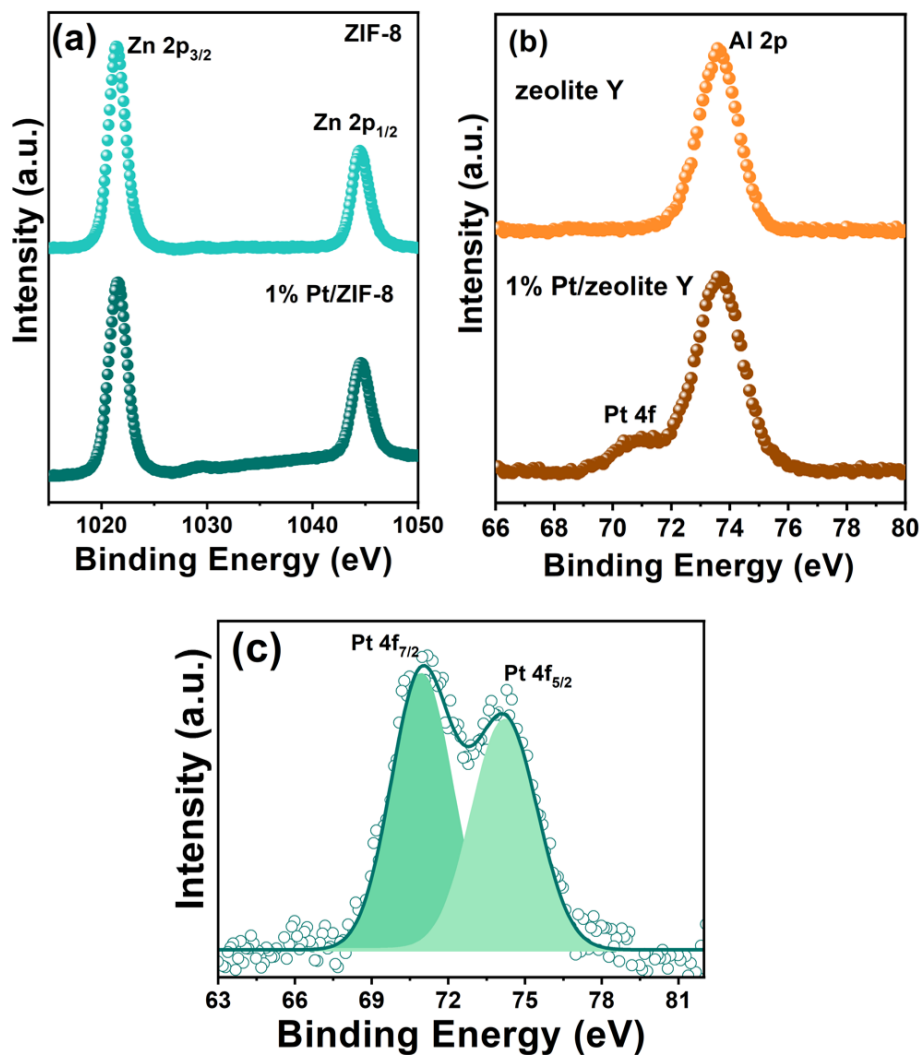


Figure 2.7: XPS (a) core level spectra of Zn in ZIF-8 and 1% Pt/ZIF-8, (b) core level spectra of Al and Pt in zeolite Y and 1% Pt/zeolite Y catalysts, and (c) core level spectra of Pt in 1% Pt/ZIF-8

samples, the binding energy of Al 2p appeared at 73.6 eV with a satellite of Pt 4f peak at 70.8 eV. The binding energy of Al 2p confirmed that the presence of aluminum in oxide form, and Pt existed as Pt(0) in the impregnation method of synthesis. Further, the surface area and porosity were studied by BET adsorption isotherms, and the isotherms are plotted in Figure 2.8. The synthesized catalysts showed type I adsorption isotherm, representing the microporous nature of the catalysts. BET surface areas are tabulated in Table 2.1. The surface area of

ZIF-8 and Pt/ZIF-8 was found to be 1468 and 1448  $\text{m}^2 \text{g}^{-1}$ , respectively, whereas zeolite Y and Pt/zeolite Y exhibited half the area of ZIF-8, and the obtained values were 755 and 702  $\text{m}^2 \text{g}^{-1}$ , respectively. The pore size distribution (PSD) is one of the most important properties, and one of the current standards for determining microscopic PSD experimentally is by using indirect molecular adsorption methods such as nonlocal density functional theory (NLDFT). The total pore volumes and pore diameters calculated by NLDFT are also tabulated in Table 2.1. The pore sizes of the synthesized ZIF-8 catalysts were found to be higher than those of zeolite Y samples. The Pt incorporation marginally reduced the surface area or porosity of the pristine materials.

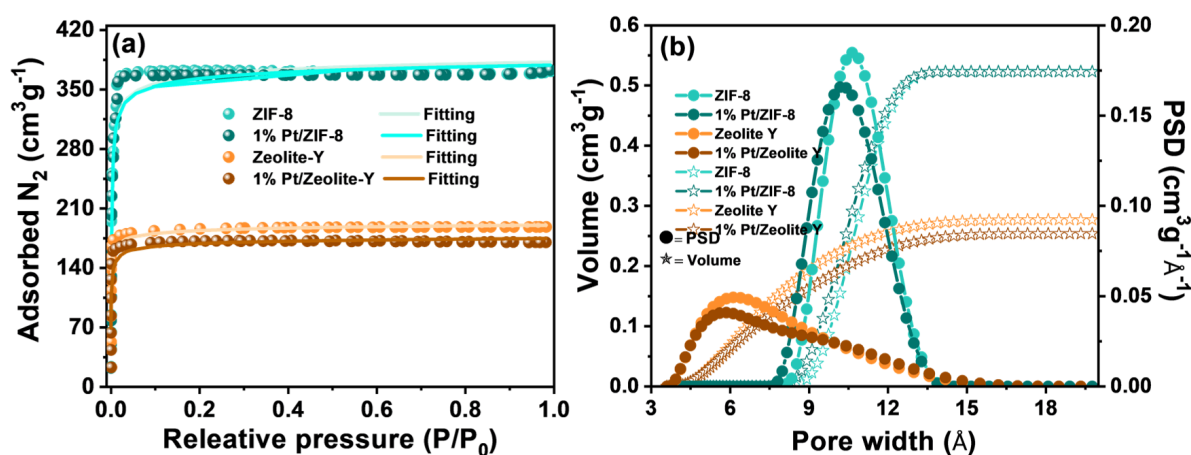


Figure 2.8: (a)  $\text{N}_2$  adsorption-desorption isotherms and (b) NLDFT pore size distribution plot of the synthesized catalysts

Table 2.1: Surface area, pore volume, and pore diameter of the synthesized catalysts

Sample	BET Surface Area ( $\text{m}^2 \text{g}^{-1}$ )	NLDFT pore Volume ( $\text{cm}^3 \text{g}^{-1}$ )	NLDFT pore Diameter ( $\text{\AA}$ )
ZIF-8	1468.3	0.410	10.65
1%Pt/ZIF-8	1448	0.388	10.28
Zeolite Y	755.8	0.133	6.19
1%Pt/Zeolite Y	702.2	0.108	5.81

The obtained results indicated that the metallic Pt is highly dispersed over the truncated cubic ZIF-8 surface resulting in a marginal decrease in the surface area and porosity of the pristine material. However, the high NO adsorption and facile  $\text{H}_2$  decomposition made Pt/ZIF-8 a superior low temperature NO reduction catalyst despite marginal loss of surface area and porosity. Next, we wanted to probe the mechanistic details of the efficient NO reduction over Pt/ZIF-8. Pt may easily oxidize NO to  $\text{NO}_2$  [61], which can be adsorbed on the basic surface of ZIF-8 as

observed in the NO-TPD experiments. Therefore, we have screened the adsorption frequency of  $\text{NO}_2^-$  over ZIF-8 and Pt/ZIF-8, and the FT-IR spectra are plotted in Figure 2.9(a). The peak at  $1638\text{ cm}^{-1}$  was observed for ZIF-8, which can be assigned to bridged  $\text{NO}_2$  species [89]. A shift of  $4\text{ cm}^{-1}$  was observed over 1% Pt/ZIF-8 indicating a stronger bridging bond between the surface and  $\text{NO}_2$  species compared to the pristine sample. Accordingly, a molecular mechanism is proposed in Figure 2.9(b).

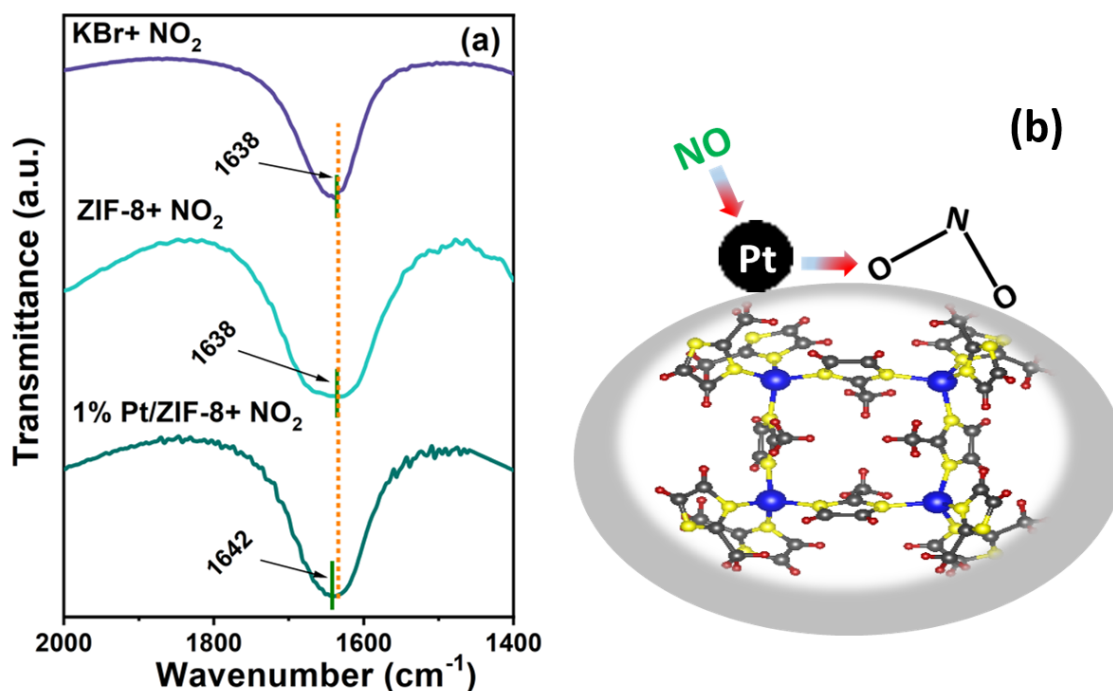


Figure 2.9: (a) FT-IR spectra of  $\text{NO}_2$  adsorption over ZIF-8 and 1% Pt/ZIF-8, and (b) a proposed molecular mechanism of NO reduction over 1% Pt/ZIF-8 surface

We further explored the recyclability performance of Pt/ZIF-8 catalyst, and the data up to four cycles are plotted in Figure 2.10. The catalyst activity was slightly decreased with each cycle as the  $T_{50}$  raised from  $45$  to  $77\text{ }^\circ\text{C}$  from the first to fourth cycle. The XRD profile of exhausted Pt/ZIF-8 in Figure 2.11(a) showed a slight shift in the peaks, which could be ascribed to the removal of guest imidazole resulting in a decrease in crystallite size. However, the morphology of the exhausted catalyst showed a similar morphology to the as prepared sample (Figure 2.11(b)). The elemental state of Pt is found as metallic after the thermal reduction of NO by  $\text{H}_2$  over 1% Pt/ZIF-8 with the presence of  $\text{Pt}^{2+}$  (Figure 2.11(c)), and the BET isotherms of the exhausted catalyst exhibited a marginally reduced surface area of  $1127.2\text{ m}^2\text{ g}^{-1}$ . The slight reduction of

the surface area of the exhausted catalyst could be due to the agglomeration of the fine particles due to thermal ageing.

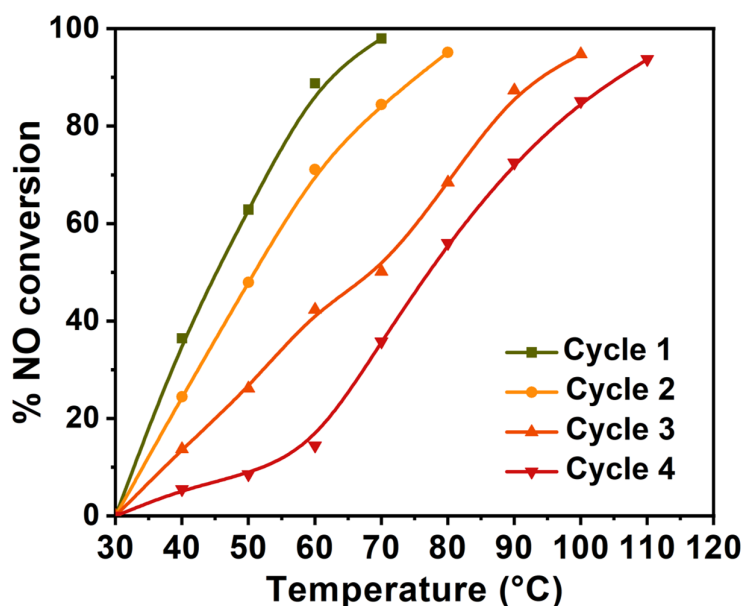


Figure 2.10: Recyclability of the reduction NO by H<sub>2</sub> over 1% Pt/ZIF-8

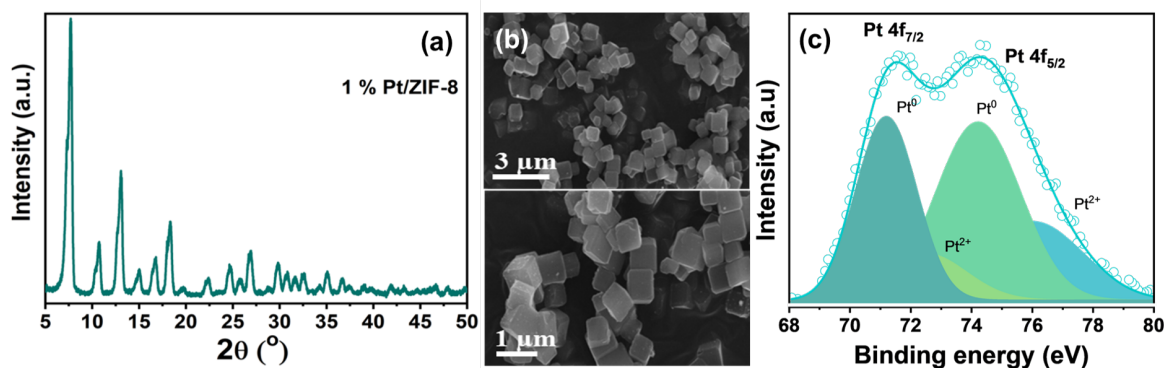


Figure 2.11: (a) XRD patterns of 1% Pt/ZIF 8 after reduction of NO by H<sub>2</sub>, (b) FE-SEM images of 1% Pt/ZIF 8 after reduction of NO by H<sub>2</sub>, and (c) Pt core level XPS Spectra of 1% Pt/ZIF 8 after reduction of NO by H<sub>2</sub>

## 2.4 Conclusion

ZIF-8 was meticulously synthesized, displaying remarkable characteristics of body-centered cubic. NO is primarily attributed to the presence of basic imidazolate units on its surface. TPR investigations revealed the low temperature H<sub>2</sub> dissociation over Pt/ZIF-8. The resulting ultra-high dispersion of metallic Pt nanoparticles on the high surface area porous ZIF-8 played a dual role. Firstly, it significantly amplified the NO adsorption capabilities of the catalyst, and

secondly, it efficiently facilitated the reduction of NO at notably low temperatures when compared to the pristine ZIF-8. Evidence from FT-IR spectroscopy results indicated the strong binding of adsorbed NO to Pt/ZIF-8 as opposed to the pristine sample. Furthermore, Pt/ZIF-8 surpassed the benchmark catalyst Pt/zeolite Y in terms of performance. Moreover, Pt/ZIF-8 demonstrated consistent recyclability, showcasing its potential as a highly effective and sustainable catalyst for NO reduction.

## Chapter 3

# Probing the surface active sites of $\text{Ce}_{1-x}\text{Ni}_x\text{O}_{2-\delta}$ for catalytic reduction of NO

### 3.1 Introduction

It is evident that extensive studies have been carried out with the supported metal catalysts for  $\text{NO}_x$  reduction [65, 90–93]. Researches have observed that noble metals dispersed on reducible oxidic supports are by far the choice of materials for low temperature selective  $\text{NO}_x$  reduction by  $\text{H}_2$  [94–97]. The existing literature establishes that the catalytic reaction follows a Langmuir–Hinshelwood type of mechanism involving the dispersed metal atoms as active sites, where the oxidizing molecule dissociates and combines with the reducing molecule. This boils down to the fact that the rate of catalytic conversion solely depends on the metal dispersion over oxide supports. Therefore, nanocrystalline metal dispersion is an important step in exhaust catalysis. However, there is a limit to metal dispersion as the small metal crystallites form bigger agglomerations due to metal–metal bonding and eventually lose their surface area. Further, the most commonly used oxide support  $\text{Al}_2\text{O}_3$  cannot be reduced by noble metals, and therefore noble metals do not get oxidized on  $\text{Al}_2\text{O}_3$ . To increase metal dispersion, reducible oxides like  $\text{CeO}_2$  have been the subject of intense research due to their importance in exhaust catalysis.

In this regard, the solid solutions of the noble and base metals in their ionic form substituted in the reducible oxides of  $\text{CeO}_2$  and  $\text{TiO}_2$  have been extensively studied by us, which indeed exhibited



much higher rates of catalytic conversion of NO under TWC and lean conditions compared to the same amount of noble metal particles dispersed over non-reducible oxides. [63, 64, 66, 98–104]. The substitutional aliovalent doped oxides, such as  $Ce_{1-x}M_xO_{2-\delta}$ ,  $Ce_{1-x-y}A_xM_yO_{2-\delta}$ , and  $Ti_{1-x}M_xO_{2-\delta}$  (M=Pt, Pd, Rh, Ru; A=Ti, Zr, Sn, Fe) created oxygen vacancy, which behaved as an active site of reaction in addition to the metal sites. Our group has proposed a metal ion-reducible support interaction that facilitated the catalytic activity through a dual site involvement in a modified Langmuir–Hinshelwood mechanism [105]. Other research groups also reported the involvement of surface oxygen vacancy in the reaction mechanism of  $NO_x$  reduction by  $H_2$  over  $Cu_2M_9CeO_x$  (M=Fe, Co, Ni) catalysts [106]. Lee et al. [107] demonstrated that the oxidized  $NiO_x/CeO_2$  catalyst due to the presence of oxygen vacancy as defect sites,  $Ni^{2+}$  oxidation state, and smaller crystallite size could enhance the catalytic activity in NO reduction. On the other hand, studies on NO reduction by CO over  $NiO/MO_x$  (M=Al, Ti, and Ce) catalysts have corroborated the crucial importance of oxygen vacancies on the oxidized and reduced  $CeO_2$  support surface for high activity and  $N_2$  generation, however, the effect of Ni oxidation state was not clear [108].

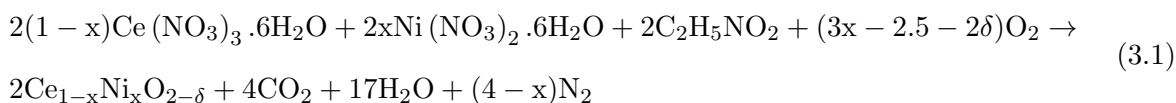
To address this unresolved issue of probing the active sites, the NO reduction by  $H_2$  over the solid solutions of  $Ce_{1-x}Ni_xO_{2-\delta}$  is investigated in this chapter, where the Ni is substituted in the fluorite lattice in its bivalent ionic form with adjacent oxygen ion vacancies.  $Ni^{2+}$  was chosen as a dopant due to the cheap and ease of accessibility of the metal compared to the precious metals. The ionic state and the oxygen vacancy were varied by reducing the catalysts in  $H_2$  atmosphere. The study indicated the importance of the surface hydroxyl species in addition to the oxygen vacancies in the catalytic NO reduction mechanism, which was further corroborated by DFT calculations. Based on the experimental observation and theoretical calculations we have developed a generalized kinetic model for the NO reduction mechanism by  $H_2$  gas over supported metal catalysts.

## 3.2 Materials and Method

### 3.2.1 Synthesis of Catalysts

The pristine  $CeO_2$  and the series of Ni doped  $CeO_2$  catalysts ( $Ce_{1-x}Ni_xO_{2-\delta}$ , where  $x=0.05, 0.1,$  and  $0.2$ ) were prepared by the low-temperature-initiated facile single step solution combustion synthesis method. This self-propagating combustion method utilizes the propellant chemistry

involving highly exothermic metathetical chemical reactions between oxidizer and fuel [109, 110]. Here, metal nitrates, Ce(NO<sub>2</sub>)<sub>3</sub>.6H<sub>2</sub>O (Sigma Aldrich, India) and Ni(NO<sub>2</sub>)<sub>3</sub>.6H<sub>2</sub>O (Sd Fine Chem Limited, India) were taken as oxidizer and glycine (Sigma Aldrich, India) was used as fuel. In the solution combustion synthesis, the initial reaction media being in the liquid state (e.g. aqueous solution) allows the mixing of the reactants on the molecular level, thus permitting precise and uniform formulation of the desired composition on the nanoscale. The high reaction temperature also ensures high product purity and crystallinity. The stoichiometric composition of the redox mixture was calculated based on the total oxidizing and reducing valences of the oxidizer and the fuel. In a typical synthesis of Ce<sub>1-x</sub>Ni<sub>x</sub>O<sub>2-δ</sub>, calculated amount of 0.05 mol of Ce(NO<sub>2</sub>)<sub>3</sub>.6H<sub>2</sub>O and Ni(NO<sub>2</sub>)<sub>3</sub>.6H<sub>2</sub>O were dissolved in a minimum volume of water in a 300 mL borosilicate dish. The dish containing the redox mixture was introduced into a muffle furnace maintained at 450 °C. Initially, the solution boiled with frothing and foaming and then underwent dehydration. At the point of complete dehydration, the surface ignited, burning with a flame with a temperature reaching about 1000 °C and yielding a voluminous solid product within a couple of minutes. The chemical reaction for Ce<sub>1-x</sub>Ni<sub>x</sub>O<sub>2-δ</sub>, is as follows:



The combustion process was instantaneous and due to the production of huge amounts of gases, the products were homogenous nano-crystalline materials with desired composition and structure. These as-prepared materials were screened for catalytic reduction of NO without any pre-treatment. The experimental setup for catalytic reactions is provided in the following sections. The catalytic reduction of NO was also carried out over reduced Ce<sub>1-x</sub>Ni<sub>x</sub>O<sub>2-δ</sub> materials. To synthesize the reduced Ce<sub>1-x</sub>Ni<sub>x</sub>O<sub>2-δ</sub>, (where x = 0.1), combustion synthesized as-prepared materials were heated under 10 cc min<sup>-1</sup> H<sub>2</sub> flow in a tubular reactor at 350 °C for 1 h of duration.

To benchmark the solution combustion synthesized catalysts, the homologous materials were also synthesized by physical mixing and wet impregnation methods. 10% NiO/CeO<sub>2</sub> was prepared by physical grinding of both the solution combustion synthesized individual oxides in their respective calculated amount for 2 h with an agate mortar and pestle. For the synthesis of 10% Ni/CeO<sub>2</sub> (IMP) by impregnation method, the calculated amount of Ni(NO<sub>2</sub>)<sub>3</sub>.6H<sub>2</sub>O was dissolved in 10 mL of water, the required amount of combustion synthesized CeO<sub>2</sub> was added to the above solution, and was stirred vigorously for 15 min. An equivalent amount of NaBH<sub>4</sub> was

added dropwise to this suspension, and stirring was continued for 2 h. The resultant solution was filtered, washed, and dried at 75 °C for 12 h in a hot air oven to obtain the 10% Ni/CeO<sub>2</sub> (IMP) catalyst.

### 3.2.2 Characterization

The structural analyses of the synthesized catalysts were carried out using powder XRD. The XRD patterns were recorded using Rigaku Ultima IV X-ray diffractometer with Cu K<sub>α</sub> radiation ( $\lambda=1.5418$  Å) at a scan rate of 0.5° min<sup>-1</sup> with step size of 0.02°. The average nanocrystalline diameters were calculated from the highest intense peak using Scherrer's formula. Rietveld refinements of the recorded XRD profiles were carried out with the Fullprof program by varying the parameters, such as scale factor, Miller indices, preferred orientation, zero point, half-width, asymmetry parameters of the peak shape, unit cell parameters, positional parameters, occupancy parameters for Ce, Ni and O atoms, isotropic thermal factors, and background intensity. HR-TEM micro images and the electron diffraction patterns were collected in the JEOL/JEM 2100 instrument using a 200 keV energy source. The surface area and morphology of the synthesized materials were studied by employing Microtrac BEL Corp mini-II surface area analyzer and FE-SEM by FEI-ApreoS respectively. Prior to the N<sub>2</sub> sorption measurements at 77 K, samples were degassed in a vacuum at 200 °C for 2 h. XPS of the catalysts were recorded in Thermo Scientific MultiLab 2000 with Al K<sub>α</sub> radiation (1486.6 eV) operated at 15 kV with 10 mA (150 W) to study the surface chemical species of the catalysts. The XPS spectra were analyzed using Avantage software and the binding energies were calibrated with respect to the carbon C1s spectra at 284.8 eV.

### 3.2.3 Catalytic Reduction of NO

All the synthesized catalysts were screened for NO reduction with H<sub>2</sub> in an indigenously built TPR system. The TPR housed a fixed bed quartz reactor with furnace and a gas chromatograph (GC) as shown in the block diagram of Figure 2.1. The quartz reactor had an inner diameter of 4 mm. The synthesized catalytic materials were made into a pellet and then were sieved with a 40-80 mesh size. The sieved materials were packed in the required weight in the quartz reactor and were sandwiched between ceramic wool plugs. The fixed bed reactor was inserted into a furnace heated to the required reaction temperature through a temperature controller, and the temperature was monitored by a K-type thermocouple dipped in the catalyst bed. The reaction

conditions were maintained with a total flow rate of  $10 \text{ mL min}^{-1}$  with GHSV of  $\sim 8000 \text{ h}^{-1}$  with 1% NO in He and 10%  $H_2$  in He procured from M/S Bhuruka Gases Ltd., India. The calculated amount of gas released from gas cylinders was regulated by pressure regulators followed by needle valves and was measured by bubble flow meters. The effluent gases from the micro-reactor were monitored using an auto-sampler of online GC (DGA I, Mayura Analytical Private Limited, India) equipped with a molecular sieve column to detect the product(s) in TCD during reduction. The gas chromatograph's oven, injector, and detector were kept at a constant temperature of  $60 \text{ }^\circ\text{C}$ .

### 3.2.4 Theoretical Calculations

Periodic DFT calculations were carried out using Quantum Espresso suite [111]. Perdew-Burke-Ernzerhof (PBE) under Generalized Gradient Approximation (GGA) [112] was used as the exchange-correlation functional, while the interaction between the outer electrons and the ionic core was represented by the projector augmented wave (PAW) method [29]. The electronic wavefunctions were expanded with a kinetic energy cutoff of 50 Ry and a charge density cutoff of 500 Ry. Electronic localization of highly correlated  $4f$  electrons of cerium was described by the inclusion of Hubbard potential in DFT+U calculations. We chose Hubbard parameter ( $U$ ) from the previous theoretical calculations as 5 eV [113]. Interactions between the crystal surface and the slab image were minimized by applying a  $15 \text{ \AA}$  vacuum above the surface. Geometry optimizations were executed by employing a convergence criterion of  $10^{-8}$  a.u. for self-consistency and  $10^{-6}$  a.u. for structural optimization. The Brillouin zone was sampled by a Monkhorst-Pack (MP) grid of  $2 \times 2 \times 1$ . The climbing-image nudged elastic band (CI-NEB) method [114] was used to find the minimum energy path during the surface reactions. We took a total of five images in this path, which included the initial and final configurations. The following formula was used for determining the adsorption energy of species (NO/H) over the surface:

$$\text{Adsorption Energy } (E_{\text{ad}}) = E(\text{CeO}_2/\text{NO}/\text{H}) - E(\text{CeO}_2) - E(\text{NO}/\text{H}) \quad (3.2)$$

$E(\text{CeO}_2/\text{NO}/\text{H})$ ,  $E(\text{CeO}_2)$  and  $E(\text{NO}/\text{H})$  are the energy of  $\text{CeO}_2$  along with the surface adsorbed species, the energy of ceria surface, and energy of the free species, respectively. The  $\text{CeO}_2$  (111) surface is the most stable surface in the ceria crystal structure [115], and all the calculations in this study were carried out over this surface.

### 3.3 Results and Discussion

#### 3.3.1 Structural, Surface and Electronic Properties

The powder XRD patterns of the as-prepared synthesized catalysts are plotted in Figure 3.1(a). The combustion synthesized pristine and the doped catalysts showed broad XRD peaks indicating a nano-crystalline nature of the materials. The short duration of the solution combustion synthesis and the formation of various gases during solution combustion synthesis inhibit particle size growth and favor the synthesis of nano-size powders with high specific surface areas. The crystallite sizes of the solution combustion synthesized materials calculated using Scherrer's formula were in the range of 7-9 nm. The pristine  $CeO_2$  crystallized in phase pure cubic fluorite structure with the space group  $Fm\bar{3}m$  (JCPDS: 34-0394) [64, 116]. Upon Ni doping,  $Ce_{0.95}Ni_{0.05}O_{2-\delta}$  and  $Ce_{0.9}Ni_{0.1}O_{2-\delta}$  did not show any additional diffraction peak corresponding to Ni or NiO phases as also observed in our previous studies [63, 100]. On the other hand, with a higher loading of 20% Ni in ceria, in Figure 3.1(a).  $Ce_{0.8}Ni_{0.2}O_{2-\delta}$  exhibited a very minor NiO peak at  $43.4^\circ$  (JCPDS: 04-0835) suggesting a precipitation of NiO phase. The enlarged profile is plotted in Figure 3.1(b). This is in agreement with the previous reports that showed a maximum solubility limit of Ni in fluorite  $CeO_2$  within the range of 12-15% [117, 118]. The pure phase solid solution of  $Ce_{0.9}Ni_{0.1}O_{2-\delta}$  was reduced with  $H_2$  at elevated temperatures, and the corresponding XRD pattern of the reduced  $Ce_{0.9}Ni_{0.1}O_{2-\delta}$  is also shown in Figure 3.1(a). The profile indicates a slight loss of crystallinity, however, no crystalline Ni or NiO was observed to precipitate as exsolution. The thermal stability of the solid solution was thus confirmed. It must be noted that the diffraction pattern of 10% NiO/ $CeO_2$  made by the physical mixing of the corresponding oxides exhibited the characteristic peaks corresponding to NiO phases as shown in Figure 3.1(c). The XRD pattern of 10% Ni/ $CeO_2$  (IMP) is also plotted in Figure 3.1(c).

To confirm the formation of a solid solution of as-prepared  $Ce_{0.95}Ni_{0.05}O_{2-\delta}$  and  $Ce_{0.9}Ni_{0.1}O_{2-\delta}$  via substitutional doping of Ni in  $CeO_2$  lattice, Rietveld refinement was carried out with the powder diffraction patterns. The refinement was not performed with the diffraction pattern of  $Ce_{0.8}Ni_{0.2}O_{2-\delta}$  as the material did not show the single fluorite phase. The refinement was carried out on the experimentally collected diffraction data by substituting  $Ni^{2+}$  in place of  $Ce^{4+}$  at the Wyckoff sites 4a and oxygen in 8c, and the observed, calculated, and difference XRD patterns of pristine  $CeO_2$  and  $Ce_{1-x}Ni_xO_{2-\delta}$  ( $x = 0.05$  and  $0.1$ ) are shown in Figure 3.1(d). The

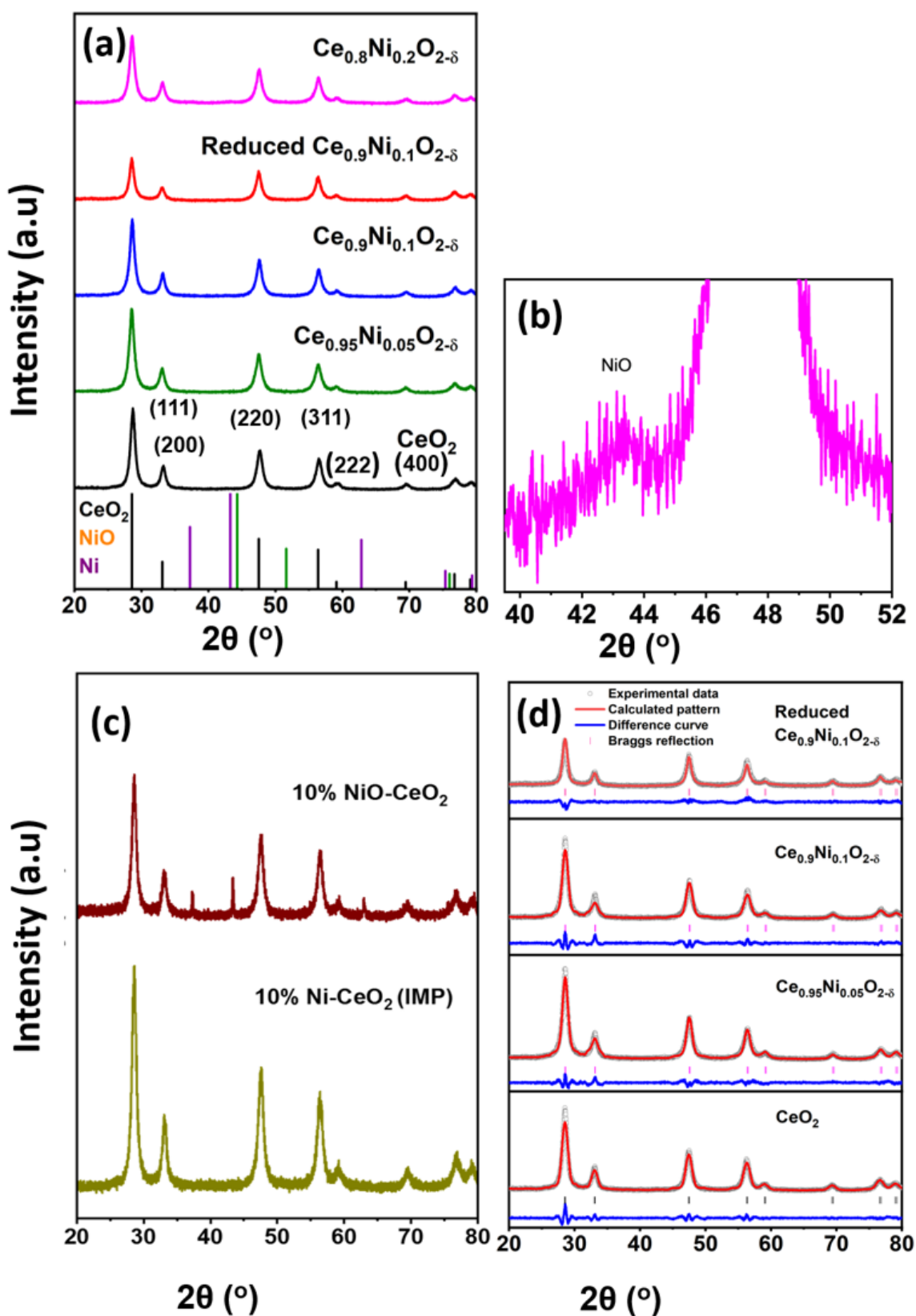


Figure 3.1: (a) XRD patterns of pristine  $CeO_2$  and as-prepared  $Ce_{0.9}Ni_{0.1}O_{2-\delta}$  ( $x = 0.05, 0.1, 0.2$ ) and reduced  $Ce_{0.9}Ni_{0.1}O_{2-\delta}$ , (b) Enlarged XRD profile of  $Ce_{0.8}Ni_{0.2}O_{2-\delta}$ , (c) XRD profile of 10% NiO/ $CeO_2$  and 10% Ni/ $CeO_2$  (IMP), and (d) Rietveld refined patterns of pristine  $CeO_2$  and as-prepared  $Ce_{0.9}Ni_{0.1}O_{2-\delta}$  ( $x=0.05$  and  $0.1$ ) and reduced  $Ce_{0.9}Ni_{0.1}O_{2-\delta}$

reliability factors  $R_{Bragg}$ , and  $\chi^2$  values provided in Table 3.1 represent a good fitting. The Shannon's ionic radii of six coordinated  $Ni^{2+}$  is 0.69 Å, whereas  $Ce^{4+}$  in  $CeO_2$  is of 0.87 Å [119]. Therefore, a substitutional solid solution would result in a contracted unit cell. The refined lattice parameters and the unit cell volumes of  $CeO_2$  and  $Ce_{1-x}Ni_xO_{2-\delta}$  ( $x=0.05, 0.1$ ) in Table 3.1 indeed indicate a slight shrink in the unit cell size of doped materials compared to the pristine one due to the lattice substitution of  $Ni^{2+}$  in  $CeO_2$ . With higher doping of smaller-sized  $Ni^{2+}$ , the fluorite lattice gradually shrunk as evidenced from Table 3.1.

Table 3.1: Rietveld refinement parameters of pristine  $CeO_2$  and  $Ce_{1-x}Ni_xO_{2-\delta}$  ( $x=0.05$  and  $0.1$ )

Sample	Lattice parameter $a = b = c$ (Å)	Cell volume (Å <sup>3</sup> )	$O_{occ}$	$R_{Bragg}$	$\chi^2$
$CeO_2$	5.4187	159.107	1.996	2.13	1.06
$Ce_{0.95}Ni_{0.05}O_{2-\delta}$	5.4111	158.441	1.952	1.74	1.17
$Ce_{0.9}Ni_{0.1}O_{2-\delta}$	5.4105	158.385	1.937	1.57	1.27
Reduced $Ce_{0.9}Ni_{0.1}O_{2-\delta}$	5.4152	158.805	1.862	5.98	1.08

Even though the X-ray scattering factor of oxygen is low compared to that of cerium, the refined oxygen occupancy obtained from the refinement can give us a trend in the variation of oxygen content. The decrease in oxygen content as a point defect is expected as a result of aliovalent substitutional doping. A decrease of oxygen occupancy ( $O_{occ}$ ) from 1.996 in pure  $CeO_2$  to 1.952 in  $Ce_{0.95}Ni_{0.05}O_{2-\delta}$  and 1.937 in  $Ce_{0.9}Ni_{0.1}O_{2-\delta}$  is evidently significant as shown in Table 3.1. This further confirms the ionic doping of  $Ni^{2+}$  in the  $CeO_2$  lattice. It must be noted that the Rietveld refinement of reduced  $Ce_{0.9}Ni_{0.1}O_{2-\delta}$  did exhibit an oxygen occupancy of 1.862. Apparently, the reducing atmosphere of  $H_2$  at elevated temperatures has created extra oxygen ion vacancy in the fluorite lattice compared to the as-prepared sample.

To corroborate the substitutional doping of Ni in the fluorite  $CeO_2$  matrix, the HR-TEM micrographs and the electron diffraction data of the as-prepared and reduced  $Ce_{0.9}Ni_{0.1}O_{2-\delta}$  were collected. The lattice fringe distance of 0.329 nm in  $Ce_{0.9}Ni_{0.1}O_{2-\delta}$  in Figure 3.2(a) was consistent with the (111) plane of the material as was also observed in powder XRD data. The electron diffraction data in Figure 3.2(b) showed the presence of characteristic planes corresponding to the cubic  $CeO_2$  structure. Any lattice fringes or planes related to NiO phase were not observed either in the TEM micrograph or in the electron diffraction pattern corroborating the formation of solid-solution through combustion synthesis. The average particle size of combustion synthesized  $Ce_{0.9}Ni_{0.1}O_{2-\delta}$  was  $\sim 35$  nm as observed from Figure 3.2(c). The reduced  $Ce_{0.9}Ni_{0.1}O_{2-\delta}$  did not show any significant change in the lattice fringe distances and in electron diffraction data, and there was no characteristic crystalline metallic Ni fringes observed (Figure 3.2(d, e)). The



average particle size of reduced  $Ce_{0.9}Ni_{0.1}O_{2-\delta}$  was  $\sim 25$  nm as observed in Figure 3.2(f).

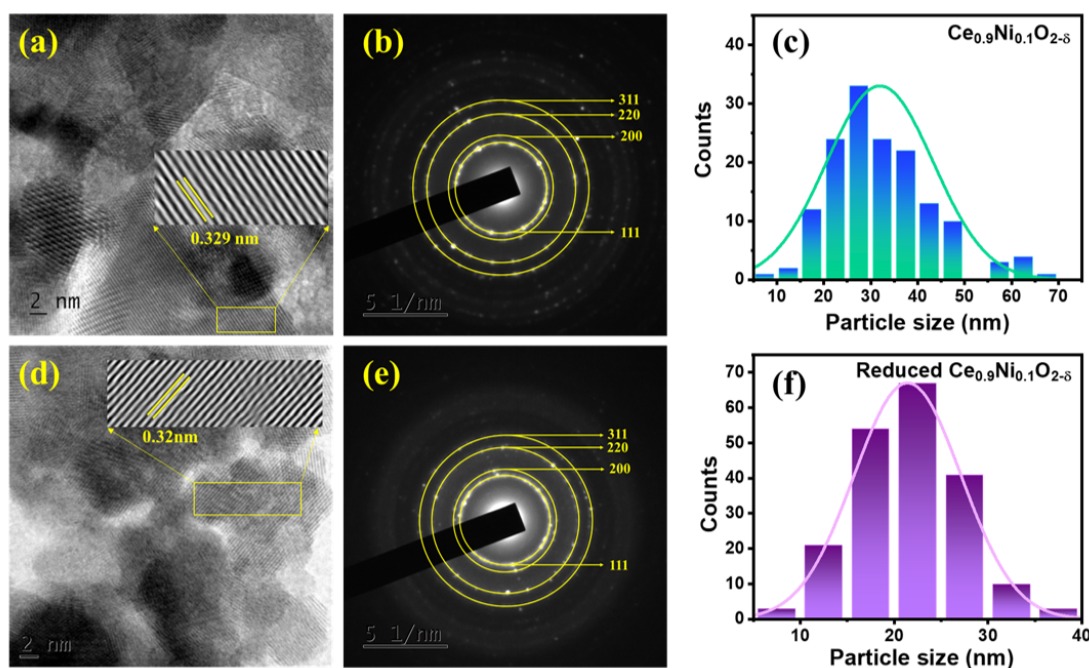


Figure 3.2: HR-TEM and particle size distribution of as-prepared and reduced  $Ce_{0.9}Ni_{0.1}O_{2-\delta}$

After a thorough structural characterization, we probed the surface of the synthesized catalysts. The electronic states of Ni and Ce can be extracted from core-level XPS spectra. The core level spectrum of Ce3d in pristine  $CeO_2$  ( $3d_{5/2}$  is labelled as v, and  $3d_{3/2}$  is labelled as u) in Figure 3.3(a) exhibits  $Ce^{4+}$  doublet peaks as v-u (882.2 and 902.6 eV), v''-u'' (888.6 and 910.2 eV), and v'''-u''' (898.1 and 916.5 eV) arising from  $Ce3d^94f^2O2p^4$ ,  $Ce3d^94f^1O2p^5$  and  $Ce3d^94f^0O2p^6$  final states, respectively [116, 120, 121]. Furthermore, the relatively well separated v'''-u''' peak from the rest of the spectrum with narrow and intense u''' delineates the presence of tetravalent  $Ce^{4+}$  in pristine  $CeO_2$ . The peaks labelled in the  $CeO_2$  spectrum as  $v_o-u_o$  (881.5 and 900.6 eV), and v'-u' (884.4 and 907.0 eV) are associated with  $Ce^{3+}$  species corresponding to  $Ce3d^94f^2O2p^5$  and  $Ce3d^94f^1O2p^6$  final states, respectively. Upon Ni doping, in as-prepared  $Ce_{0.9}Ni_{0.1}O_{2-\delta}$  and in reduced  $Ce_{0.9}Ni_{0.1}O_{2-\delta}$  the corresponding  $Ce^{4+}$  and  $Ce^{3+}$  peaks remained almost in the same position, however their respective intensities marginally varied (Figure 3.3(a)). The relative surface concentrations (C) of  $Ce^{3+}$  and  $Ce^{4+}$  was estimated from deconvoluted peak areas (S) by using the following equations:



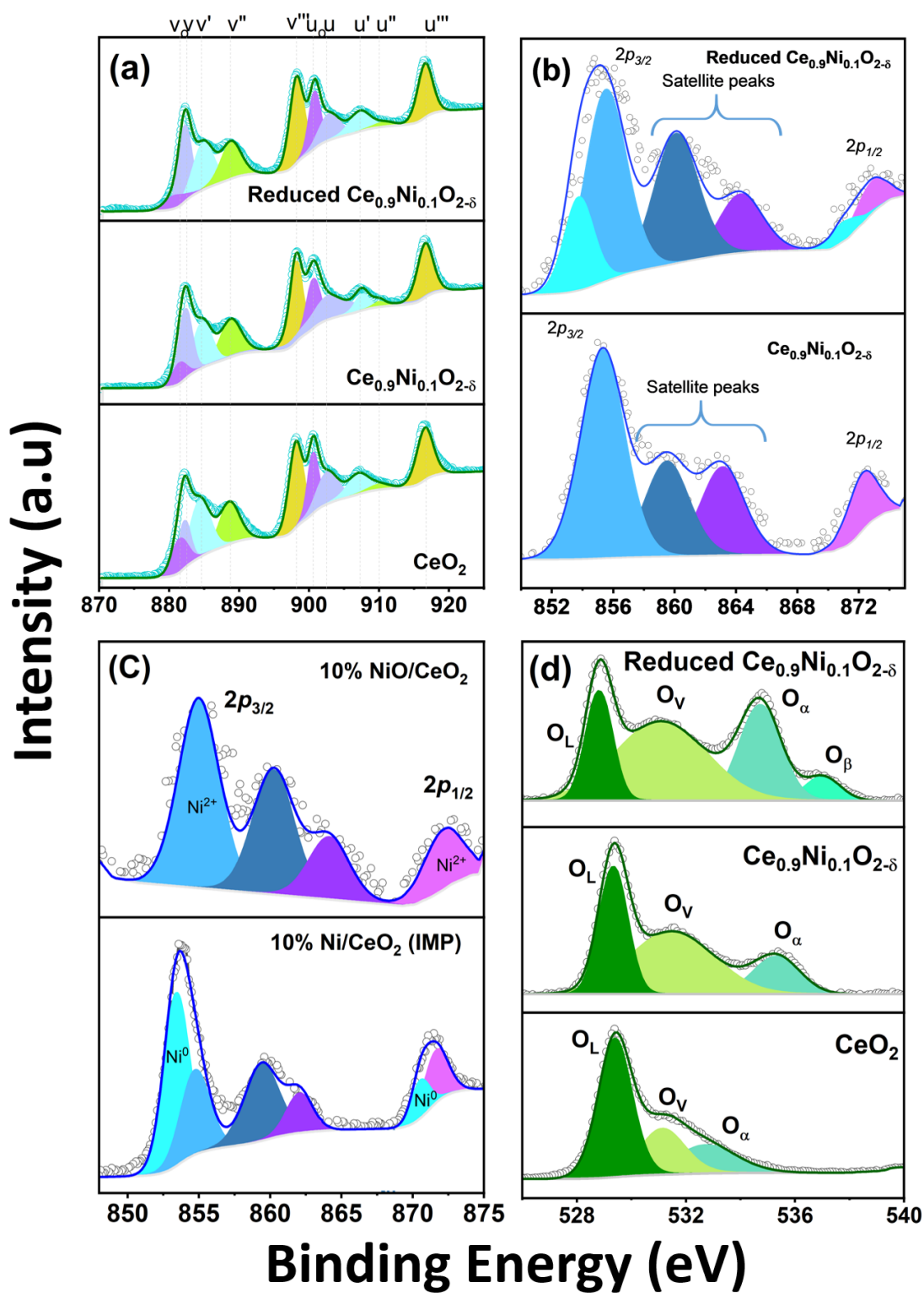


Figure 3.3: (a) Ce 3d core level spectra in pristine  $CeO_2$ , and as-prepared and reduced  $Ce_{0.9}Ni_{0.1}O_{2-\delta}$ , (b) Ni 2p core level spectra of as-prepared and reduced  $Ce_{0.9}Ni_{0.1}O_{2-\delta}$ , (c) Ni 2p core level spectra of 10% NiO/ $CeO_2$  and 10% Ni/ $CeO_2$  (IMP), and (d) O 1s core level spectra of pristine  $CeO_2$ , and as-prepared and reduced  $Ce_{0.9}Ni_{0.1}O_{2-\delta}$

$$S_{Ce^{4+}} = S_v + S_u + S_{v''} + S_{u''} + S_{v'''} + S_{u'''} \quad (3.3)$$

$$S_{Ce^{3+}} = S_{vo} + S_{uo} + S_{v'} + S_{u'} \quad (3.4)$$

$$C_{Ce^{4+}} = \frac{S_{Ce^{4+}}}{S_{Ce^{4+}} + S_{Ce^{3+}}} \quad (3.5)$$

Accordingly, the relative surface concentration of  $Ce^{4+}$  and  $Ce^{3+}$  are obtained to be 53.7% and 46.31% in pristine  $CeO_2$ , and 51.8% and 48.2% in as-prepared  $Ce_{0.9}Ni_{0.1}O_{2-\delta}$ . The reduced  $Ce_{0.9}Ni_{0.1}O_{2-\delta}$  exhibited a relative surface concentration of  $Ce^{4+}$  and  $Ce^{3+}$  to be 52.6% and 47.4%. Apparently, the elevated temperature reduction did not reduce much of  $Ce^{4+}$ . Figure 3.3(b) shows the Ni core level spectra, where the deconvolution indicates that the as-prepared  $Ce_{0.9}Ni_{0.1}O_{2-\delta}$  is comprised of bivalent  $Ni^{2+}$  with  $2p_{3/2}$  and  $2p_{1/2}$  at the binding energies of 855.4 eV and 871.7 eV, respectively [122]. These peaks are also accompanied by satellite peaks at 860.1 and 865.4 eV [123]. After reduction, reduced  $Ce_{0.9}Ni_{0.1}O_{2-\delta}$  did show a mixed Ni valency with 6.8% metallic  $Ni^0$ . However, it must be noted that the corresponding crystalline peaks due to  $Ni^0$  were obscured in the electron diffraction and XRD patterns may be due to its amorphous nature. The Ni core level spectra of 10% NiO/ $CeO_2$  and 10% Ni/ $CeO_2$  (IMP) are plotted in Figure 3.3(c). The Ni in 10% NiO/ $CeO_2$  clearly showed the presence of ionic  $Ni^{2+}$ , whereas a significant percentage of  $Ni^0$  was observed in 10% Ni/ $CeO_2$  (IMP) catalyst.

The O 1s deconvoluted core-level spectra of pristine  $CeO_2$  plotted in Figure 3.3(d) show three distinguishable peaks at 529.3 eV due to lattice oxygen ( $O_L$ ), at 531.5 eV due to adsorbed oxygen species in the defect sites ( $O_v$ ), and at 535.3 eV corresponding to hydroxyl species of surface-adsorbed water molecules ( $O_\alpha$ ). Clearly, the peak ratio of the surface oxygen vacancy ( $O_v$ ) to lattice oxygen ( $O_L$ ) has significantly enhanced in as-prepared  $Ce_{0.9}Ni_{0.1}O_{2-\delta}$  compared to the pristine  $CeO_2$ . The aliovalent doping of  $Ni^{2+}$  in the fluorite matrix has apparently created the oxygen vacancy as point defects [64, 99, 124]. The  $O_v/O_L$  was found to be highest in reduced  $Ce_{0.9}Ni_{0.1}O_{2-\delta}$  suggesting an enhanced surface bound oxygen vacancies upon high temperature reduction. It must be noted that the enhancement of oxygen vacancies upon reduction was also indicated in Rietveld refinement. An additional hydroxyl species of  $O_\beta$  at 537.0 eV was observed in reduced  $Ce_{0.9}Ni_{0.1}O_{2-\delta}$  [125]. It can be concluded from the XPS studies that the elevated temperature reduction could not significantly reduce  $Ce^{4+}$ , however has created amorphous  $Ni^0$  and surface oxygen vacancies along with additional hydroxyl species on the surface of reduced  $Ce_{0.9}Ni_{0.1}O_{2-\delta}$ .

The surface morphology of the pristine  $CeO_2$  and the as-prepared and reduced  $Ce_{0.9}Ni_{0.1}O_{2-\delta}$  catalysts were probed by FE-SEM. The FE-SEM micrographs of both pristine  $CeO_2$  and as-prepared  $Ce_{0.9}Ni_{0.1}O_{2-\delta}$  in Figure 3.4(a) and (b) exhibited spherical and agglomerated particles. The Ni doping apparently did not make any significant change in the morphology of the particles. The elevated temperature reduction also did not make any impact on the morphology of reduced  $Ce_{0.9}Ni_{0.1}O_{2-\delta}$  as observed from Figure 3.4(c). The BET surface area of the pristine  $CeO_2$ , as-prepared and reduced  $Ce_{0.9}Ni_{0.1}O_{2-\delta}$  were in the range of  $\sim 40 \text{ m}^2 \text{ g}^{-1}$  (Figure 3.4(d)).

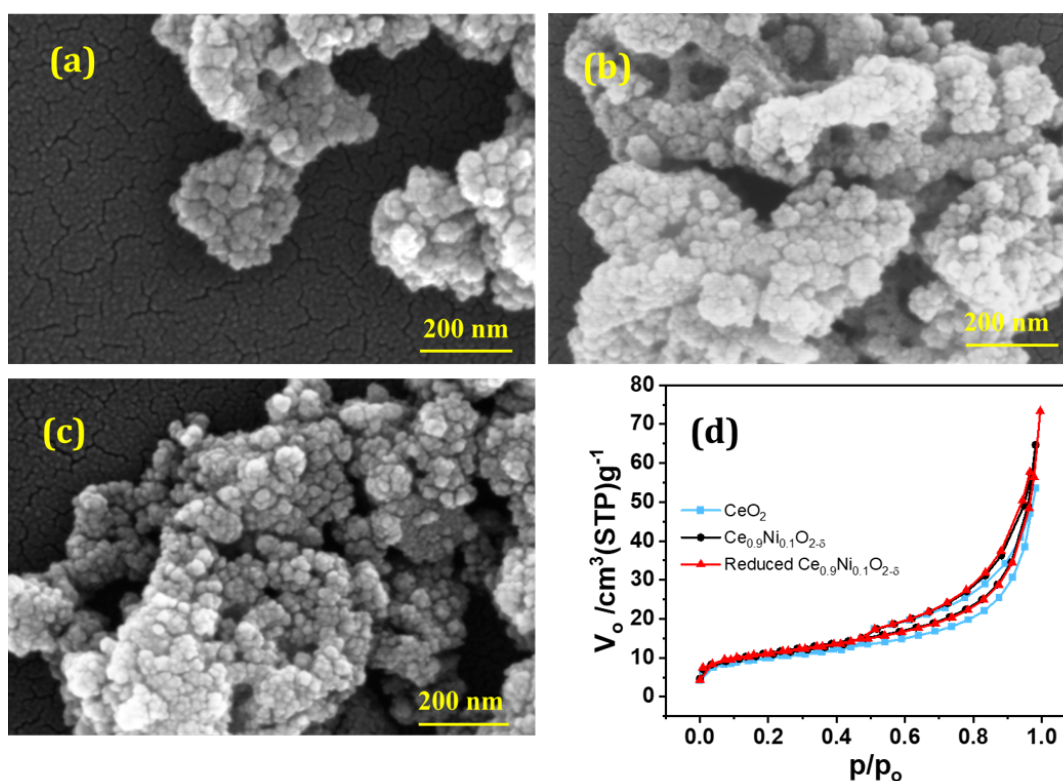


Figure 3.4: (a) FE-SEM of (a) pristine  $CeO_2$ , (b) as-prepared  $Ce_{0.9}Ni_{0.1}O_{2-\delta}$ , (c) reduced  $Ce_{0.9}Ni_{0.1}O_{2-\delta}$ , and (d)  $N_2$  sorption isotherms of pristine  $CeO_2$ , as-prepared and reduced  $Ce_{0.9}Ni_{0.1}O_{2-\delta}$

### 3.4 Catalytic performances

The catalytic activity of the solution combustion synthesized  $Ce_{0.9}Ni_{0.1}O_{2-\delta}$  materials towards NO reduction was evaluated with equimolar mixture of 1:1 vol% (5000 ppm each) of NO and  $H_2$ . The concentration of 5000 ppm taken for the study was higher compared to reaction conditions reported in the literature [126, 127]. The light-off curves in Figure 3.5(a) show the NO conversion

efficiency of as-prepared  $Ce_{0.9}Ni_{0.1}O_{2-\delta}$  ( $x = 0, 0.05, 0.1, 0.2$ ) as a function of temperatures. The

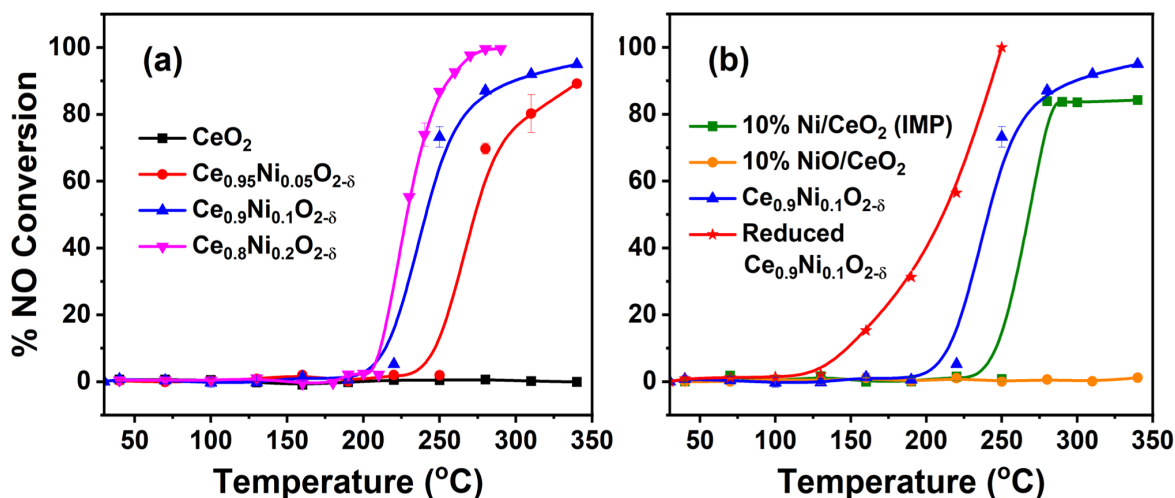


Figure 3.5: NO conversion efficiency plot as a function of temperature over the synthesized catalysts

profiles show that there was no catalytic reduction of NO over pristine  $CeO_2$  within the experimental temperature window, whereas the  $Ni^{2+}$  doped materials could reduce NO between 280-340 °C. The results clearly showed the importance of doping of  $Ni^{2+}$  and the corresponding oxide ion vacancies in the NO reduction reaction. The  $T_{50}$  of  $Ce_{0.95}Ni_{0.05}O_{2-\delta}$ ,  $Ce_{0.9}Ni_{0.1}O_{2-\delta}$  and  $Ce_{0.8}Ni_{0.2}O_{2-\delta}$  were at 272, 240 and 233 °C, respectively. Apparently, there was a significant lowering of  $T_{50}$  from  $Ce_{0.95}Ni_{0.05}O_{2-\delta}$  to  $Ce_{0.9}Ni_{0.1}O_{2-\delta}$ , whereas with higher than 10% of  $Ni^{2+}$  doping the catalytic efficacy did not improve substantially. For all practical purposes,  $Ce_{0.9}Ni_{0.1}O_{2-\delta}$  with 10% of  $Ni^{2+}$  doping can be considered as the optimum doping level for catalytic efficiency. It must also be noted that with 20% of  $Ni^{2+}$  doping,  $Ce_{0.8}Ni_{0.2}O_{2-\delta}$  did not show a single-phase fluorite structure. To further probe the role of lattice doped  $Ni^{2+}$  and oxygen vacancies in catalytic NO reduction, 10% Ni/CeO<sub>2</sub> (IMP) made by the impregnation method and 10% NiO/CeO<sub>2</sub> made by the physical mixing of the corresponding oxides were compared with as-prepared  $Ce_{0.9}Ni_{0.1}O_{2-\delta}$ , where the Ni atomic percentage was kept constant at 10% in all the catalysts. It should be noted that in 10% Ni/CeO<sub>2</sub> (IMP) and in 10% NiO/CeO<sub>2</sub>, the Ni was in mixed valent and bivalent states, respectively, and also on the surface of CeO<sub>2</sub> in comparison to  $Ce_{0.9}Ni_{0.1}O_{2-\delta}$ , where the bivalent  $Ni^{2+}$  is positioned in the fluorite lattice of CeO<sub>2</sub>. The light-off curves in Figure 3.5(b) show that there was absolutely no NO reduction over 10% NiO/CeO<sub>2</sub> within the experimental temperature window, whereas 10% Ni/CeO<sub>2</sub> (IMP) could reduce NO

with a  $T_{50}$  at 270 °C. This is 30 °C higher than the  $T_{50}$  value of NO reduction over as-prepared  $Ce_{0.9}Ni_{0.1}O_{2-\delta}$ . Also, only  $\sim 80\%$  of feed NO was reduced till 350 °C over 10% Ni/CeO<sub>2</sub> (IMP). This indicates that neither cationic Ni<sup>2+</sup> nor metallic Ni<sup>0</sup> outside the CeO<sub>2</sub> lattice is the active species for effective NO reduction under experimental conditions. Rather ionically doped Ni<sup>2+</sup> in the fluorite lattice in combination with the oxygen vacancies can effectively reduce NO with H<sub>2</sub>.

To further establish the importance of the oxygen ion vacancies, we have performed the NO reduction by H<sub>2</sub> over reduced  $Ce_{0.9}Ni_{0.1}O_{2-\delta}$ . The reduced  $Ce_{0.9}Ni_{0.1}O_{2-\delta}$  had higher concentration of oxygen vacancies and additional hydroxyl species than the as-prepared  $Ce_{0.9}Ni_{0.1}O_{2-\delta}$ . There was also a minimal presence of amorphous Ni<sup>0</sup> along with Ni<sup>2+</sup> in reduced  $Ce_{0.9}Ni_{0.1}O_{2-\delta}$ , whereas the oxidation state of Ce<sup>4+</sup> remained intact as was observed from the XRD and XPS studies. The light-off curve of reduced  $Ce_{0.9}Ni_{0.1}O_{2-\delta}$  showed a significant improvement of the reduction of NO with a  $T_{50}$  as low as 220 °C (Figure 3.5(b)). The NO reduction was initiated only at 130 °C and the complete reduction took place by 240 °C over reduced  $Ce_{0.9}Ni_{0.1}O_{2-\delta}$ .

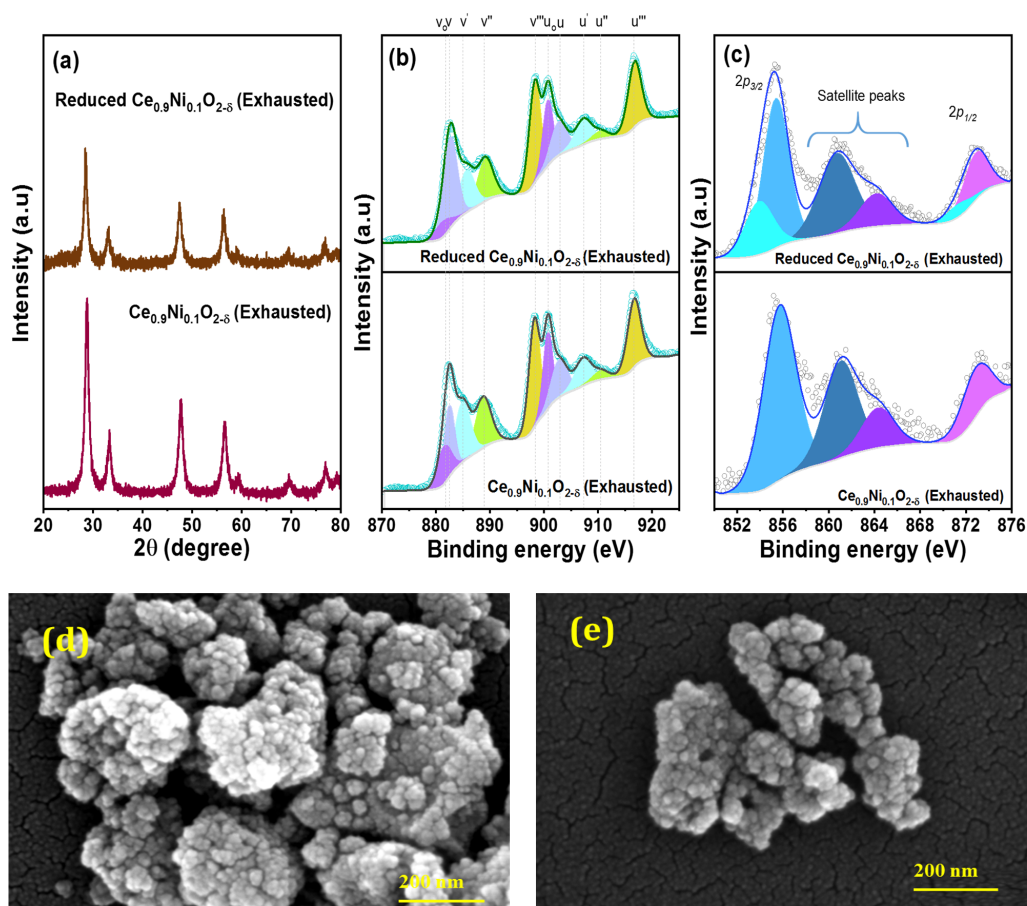


Figure 3.6: (a) XRD, (b) XPS, and (c) FE-SEM characterization of exhausted catalysts after NO reduction by H<sub>2</sub>

This indicates that the mixed valency of Ni and/or excess oxygen vacancies and additional hydroxyl species acted as active sites for the reduction of NO. The exhausted materials did not exhibit any observable difference in structure and in surface morphology as shown in XRD, XPS, and FE-SEM studies in Figure 3.6. To substantiate the differences between the catalytic efficacy of as-prepared and reduced  $Ce_{0.9}Ni_{0.1}O_{2-\delta}$ , we performed the catalytic NO reduction over the two sets of materials in the cycle. After the first catalytic NO reduction over as-prepared  $Ce_{0.9}Ni_{0.1}O_{2-\delta}$ , we reduced the catalyst at 500 °C for 1 h in  $H_2$  gas flow, and screened the reduced material for NO reduction. Following that the exhausted material was further oxidized at 500 °C for 1 h in  $O_2$  atmosphere for the second run of NO reduction. This cycle was continued two times. Figure 3.7 clearly shows the hysteresis in light-off curves with a prominent difference in  $T_{50}$  between the set of oxidized and reduced  $Ce_{0.9}Ni_{0.1}O_{2-\delta}$  materials. This corroborates the higher efficacy of reduced  $Ce_{0.9}Ni_{0.1}O_{2-\delta}$  over the as-prepared/oxidized  $Ce_{0.9}Ni_{0.1}O_{2-\delta}$  material.

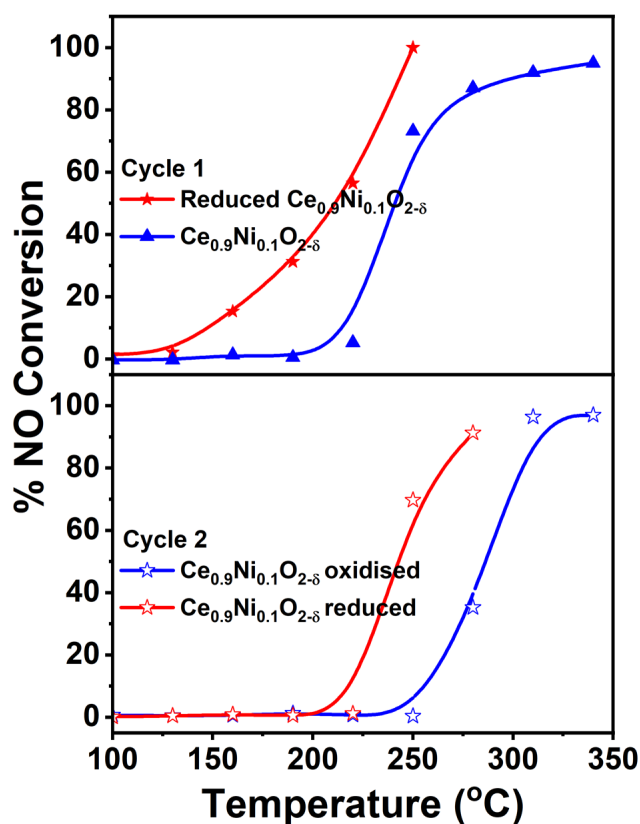


Figure 3.7: Cyclic NO reduction experiments on oxidized and reduced  $Ce_{0.9}Ni_{0.1}O_{2-\delta}$

The shift in temperature from cycle 1 to cycle 2 could be due to some deactivation in the exhausted catalyst. To probe the differences in surface, we ran the XPS of Ni  $2p$  and O  $1s$  core



level over the oxidized and reduced set of materials before the second cycle. Interestingly, we found that the metal Ni was completely in the bivalent state in the oxidized sample, and in the mixed valence state in the reduced sample before the second run of NO reduction as was also observed before the first cycle (Figure 3.8(a)). Further, the O 1s spectra exhibited the presence of the high amount of oxygen vacancy ( $O_V$ ) and the existence of the additional hydroxyl species of  $O_\beta$ , which were absent in the oxidized sample before the second cycle of NO reduction (Figure 3.8(b)). This apparently indicates that the as-prepared/oxidized  $Ce_{0.9}Ni_{0.1}O_{2-\delta}$  upon subsequent reduction can generate the mixed valences, higher oxygen vacancies ( $O_V$ ), and additional surface hydroxyl species ( $O_\beta$ ) repeatedly for better catalytic NO reduction. The repeated generation of active sites in consecutive cycles is a significant novelty of the material.

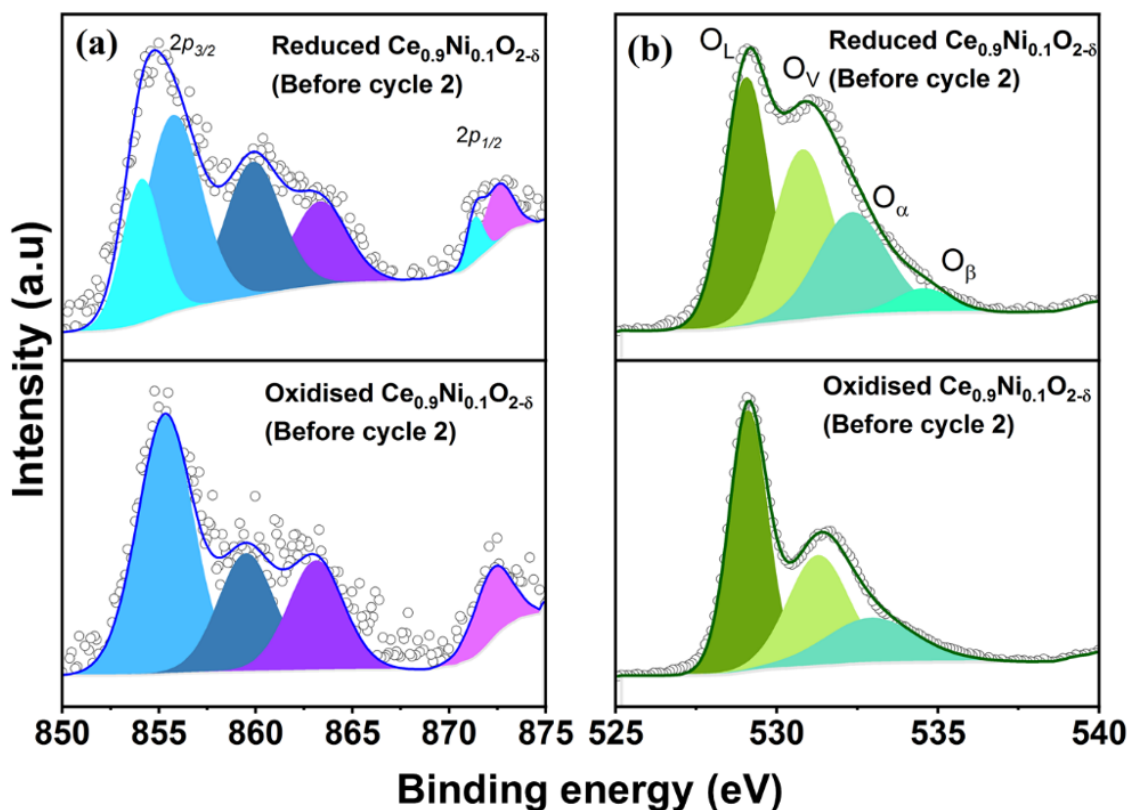


Figure 3.8: Ni 2p and O 1s core level spectra of oxidized and reduced  $Ce_{0.9}Ni_{0.1}O_{2-\delta}$  before Cycle 2

As the reduced  $Ce_{0.9}Ni_{0.1}O_{2-\delta}$  showed comparatively better catalytic activity than the analogous as-prepared one, we further evaluated the activation energy of NO reduction over the two catalysts. The experiments were performed by passing the constant flow of  $H_2$  and NO mixture

through the reactor over a different loading of catalysts varying from 25 to 100 mg while maintaining the same GHSV of  $\sim 8000 \text{ h}^{-1}$ . The slope from the plot of fractional conversion ( $X_{NO}$ ) vs. load of catalyst/molar flow rate of NO ( $W/F_{NO}$ ) gives the rate ( $-r_{NO}$ ) as per the equation  $W/F_{NO} = X_{NO}/(-r_{NO})$  (Figure 3.9). The obtained rate against temperature (in the range of 210 to 240 °C) plotted in the form of the Arrhenius equation in Figure 3.9(d) provided the activation energy ( $E_a$ ) over the respective catalysts. The  $E_a$  of  $121.5 \text{ kJ mol}^{-1}$  for reduced  $Ce_{0.9}Ni_{0.1}O_{2-\delta}$  and  $350.5 \text{ kJ mol}^{-1}$  for as-prepared  $Ce_{0.9}Ni_{0.1}O_{2-\delta}$  clearly indicated the higher catalytic efficacy of the reduced material over its oxidized analogue.

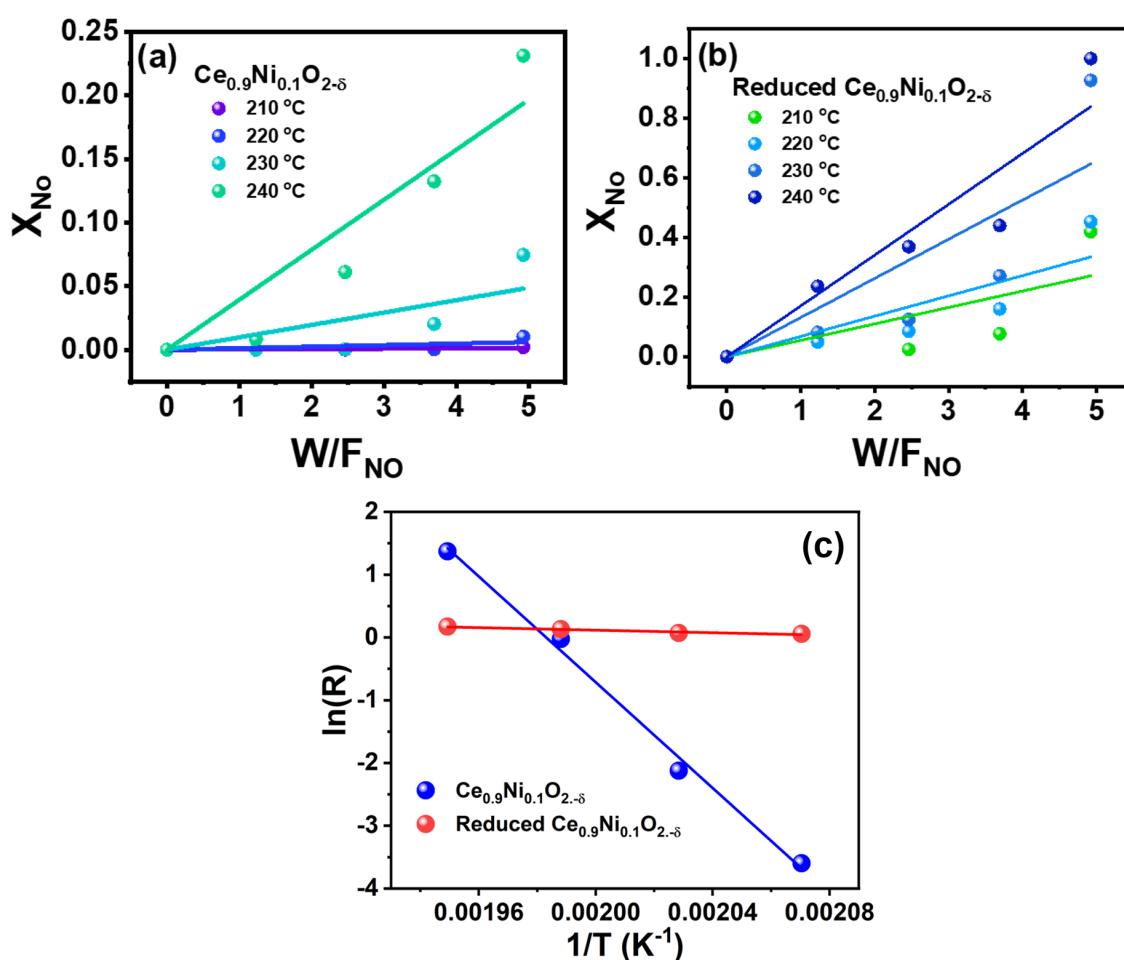


Figure 3.9: Partial pressure vs.  $W/F_{NO}$  plot over (a) as-prepared  $Ce_{0.9}Ni_{0.1}O_{2-\delta}$ , (b) reduced  $Ce_{0.9}Ni_{0.1}O_{2-\delta}$ , and (c) Activation Energy from Arrhenius plot



### 3.5 Mechanistic probe

The spectroscopic evidence rationalized that the mixed valency of Ni and/or excess oxygen vacancies and additional hydroxyl species were responsible for the higher catalytic efficacy of the reduced material compared to the as-prepared/oxidized  $Ce_{0.9}Ni_{0.1}O_{2-\delta}$ . Further, DFT calculations were carried out to probe the surface active sites, and to understand the molecular mechanism of NO reduction over the oxidized and reduced set of materials. The experimentally proved ionic substitution of  $Ni^{2+}$  in the fluorite structure of  $CeO_2$  must result in changes in its surrounding metal-oxygen bond lengths. Initial bond lengths between Ce and lattice oxygen were calculated to be  $\sim 2.34$  Å, which after  $Ni^{2+}$  substitution changed to a broad range of 1.85-3.8 Å. DFT calculated NO bond length was 1.17 Å, which were in agreement with previous reports [128]

Surface adsorption of reactants is the first step of any heterogeneously catalyzed reaction. Hence, we studied the adsorption of NO and  $H_2$  over the catalytic surface, as detailed in the text to follow. Two categories of adsorption configurations of NO over  $Ce_{0.9}Ni_{0.1}O_{2-\delta}$  were identified viz.,  $NO_2$ -like and NO-like. Optimized structures of different configurations hence obtained are shown in Figure 3.10(a)-(h). NO was observed to be adsorbed over the lattice oxygen at a distance of  $\sim 3.8$  Å from Ni forming  $NO_2$ -like species ( $NO_2$ -1, Figure 3.10(a)). The bond length of NO increased to 1.23 Å indicating the activation of NO on surface adsorption. The corresponding adsorption energy was -1.39 eV. In another configuration of  $NO_2$ -like species ( $NO_2$ -2, Figure 3.10(b)), NO interacted with the subsurface lattice oxygen, and O of NO occupied

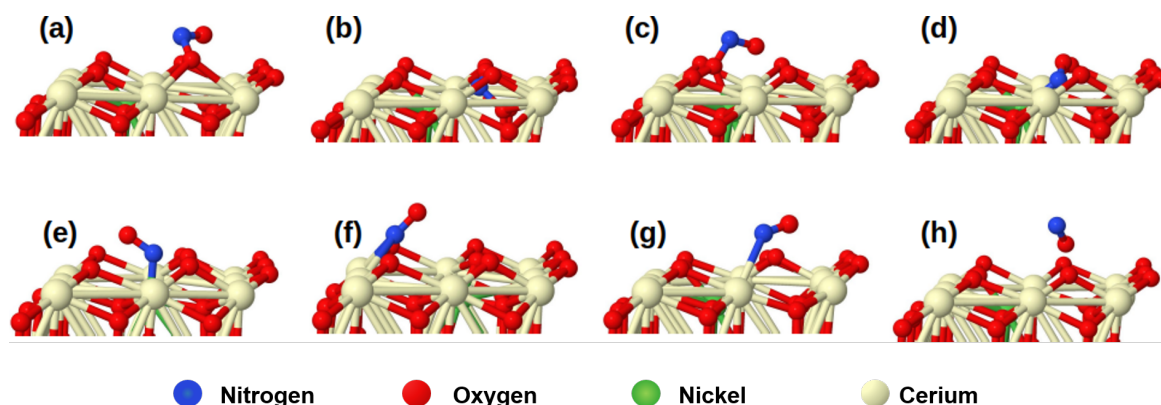


Figure 3.10: Adsorption configurations of NO over  $Ce_{0.9}Ni_{0.1}O_{2-\delta}$ : (a)  $NO_2$ -1, (b)  $NO_2$ -2, (c)  $NO_2$ -3, (d) NiNO-1, (e) NiNO-2, (f) Ce-bi-NO, (g) Ce-mono-NO, and (h)  $NO_v$

the oxygen vacancy. The adsorption energy of this configuration was -0.99 eV making it 0.4 eV less stable than the previous NO<sub>2</sub>-1 configuration. NO<sub>2</sub>-3 configuration (Figure 3.10(c)) had an adsorption energy of only -0.73 eV. An interesting observation from these NO<sub>2</sub>-like configurations were that adsorption energy decreased as the atomic distance between lattice oxygen and Ni decreased. The order of stability in these NO adsorption configurations was NO<sub>2</sub>-1 (Ni-O=3.93 Å) > NO<sub>2</sub>-2 (Ni-O=2.91 Å) > NO<sub>2</sub>-3 (Ni-O=1.9 Å). All of these NO<sub>2</sub>-like species had similar N-O bond lengths.

In the second type of adsorption configuration, i.e. NO-type, NO adsorbed over Ce, Ni, and oxygen vacancy with monodentate and bidentate configurations (Figure 3.10(d)-(h)). NO adsorbed over Ni (NiNO-1, Figure 3.10(d)) with O of NO near the oxygen vacancy. The corresponding adsorption energy was -0.76 eV. The NO<sub>2</sub>-2 configuration was similar to NiNO-1 configuration except that the distance between lattice oxygen (subsurface) to NO molecule was larger in the case of NiNO-1. Another adsorption configuration of NO on Ni (NiNO-2, Figure 3.10(e)) had a very small adsorption energy of -0.38 eV. This showed that adsorption over Ni and interaction with either lattice oxygen or oxygen vacancy resulted in higher interaction of NO with the catalyst surface.

Adsorption of NO over Ce exhibited both bidentate and monodentate configurations (Figure 3.10(f)-(g)). Bidentate adsorption (Ce-bi-NO) energy (-0.41 eV) was larger than the monodentate adsorption (Ce-mono-NO) energy (-0.25 eV) which further confirmed the contributions of surface environment to the stability of species. The least stable adsorption configuration (adsorption energy = 0.13 eV) was observed with NO when O of NO interacted with only the oxygen vacancy (NO<sub>v</sub>, Figure 3.10(h)). Hence, it is concluded from the adsorption energetics that NO over Ce<sub>0.9</sub>Ni<sub>0.1</sub>O<sub>2-δ</sub> favored the formation of NO<sub>2</sub>-like species with the involvement of lattice oxygen sites (configurations NO<sub>2</sub>-1; see Figure 3.10(a)). Therefore, in this first step of NO adsorption, the Ni and oxygen vacancy sites did not play the primary role as active sites.

For the reduction of NO with H<sub>2</sub>, the stoichiometry dictates the involvement of one more NO molecule. For the inclusion of the second NO, we chose NO<sub>2</sub>-1 configuration because it had the highest adsorption energy among all single NO molecule adsorption configurations over Ce<sub>0.9</sub>Ni<sub>0.1</sub>O<sub>2-δ</sub>. In this step, we found four different adsorption configurations of the second NO over NO-Ce<sub>0.9</sub>Ni<sub>0.1</sub>O<sub>2-δ</sub>, as shown in Figure 3.11(a)-(d). NO at this stage was also adsorbed over lattice oxygen and oxygen vacancy. In the first adsorption configuration, oxygen vacancy was occupied by N of NO with its oxygen interacting with Ce (2NO<sub>v1</sub>) resulting in an adsorption

energy of -0.56 eV. Depending on the interaction of the second NO with Ce, two adsorption configurations were identified viz.,  $2NO_{v2}$  (Figure 3.11(b)) in which N of NO interacted with Ce, and  $2NO_{v3}$  (Figure 3.11(c)) in which N of NO was directed away from Ce. The adsorption energies for the two configurations were -0.37 eV and -0.2 eV, respectively. Therefore, it can be concluded that the oxygen vacancy occupied by O of the second NO molecule resulted in lesser adsorption energy. Similar to the first NO adsorption, the second NO adsorption with  $2NONO_2$  configuration (Figure 3.11(d)) showed an adsorption energy of -0.44 eV. The bond length of NO was 1.19 Å. Hence, on comparison of adsorption energetics of the second NO molecule, it can be concluded that the NO molecule occupied the oxygen vacancy site as the most stable configuration, and therefore oxygen vacancy is one key active species in the second step of NO adsorption. Comparative energetics of various adsorptions are shown in Figure 3.12.

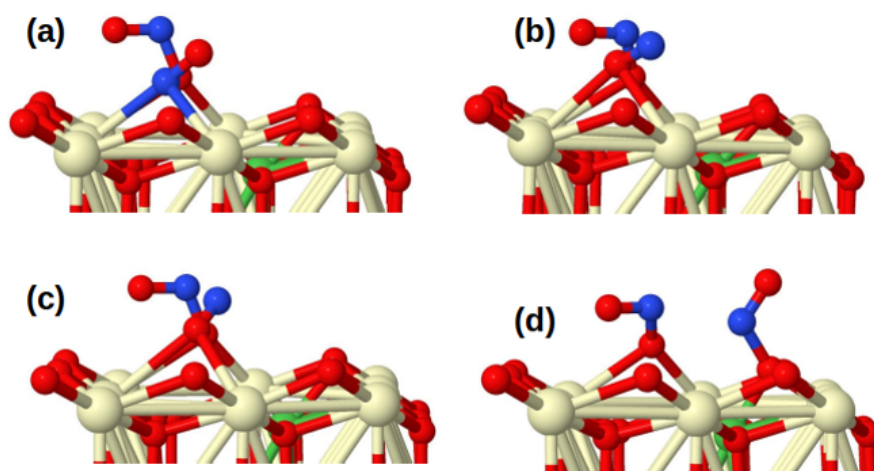


Figure 3.11: Adsorption configurations of second NO molecule over  $NO-Ce_{1-x}Ni_xO_{2-\delta}$ : (a)  $2NO_{v1}$ , (b)  $2NO_{v2}$ , (c)  $2NO_{v3}$ , and (d)  $2NONO_2$

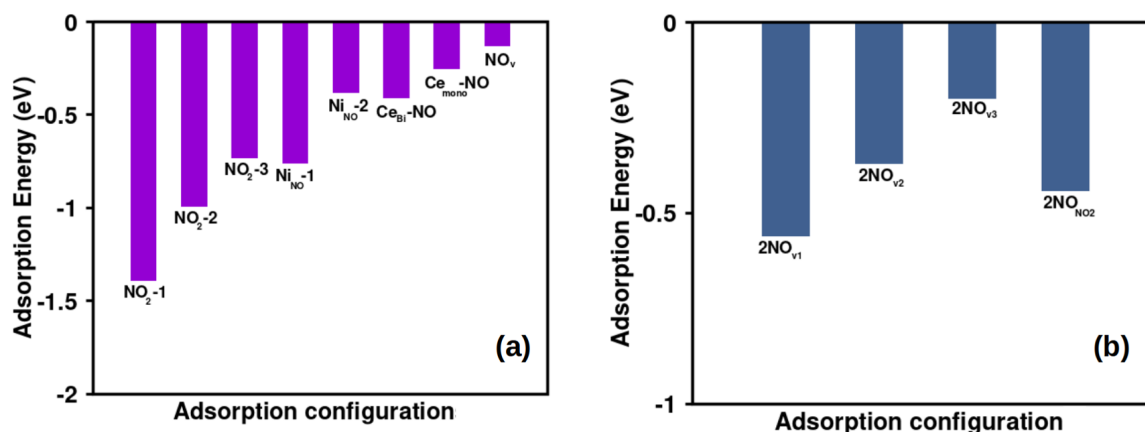


Figure 3.12: Adsorption energetics for NO over  $Ce_{1-x}Ni_xO_{2-\delta}$  (a) adsorption of first NO (b) adsorption of second NO

Molecular hydrogen adsorption was tested over  $Ce_{0.9}Ni_{0.1}O_{2-\delta}$  and no stable configuration was obtained. Atomic hydrogen adsorption over the surface formed surface hydroxyl species, which was the most stable when H coordinated with the lattice oxygen in the vicinity of Ni. The adsorption energy for this system was obtained as -0.9 eV. The optimized structure for the surface hydroxyl formed as a result of dissociative adsorption of  $H_2$  over the surface is shown in Figure 3.13. It must be noted that the reduced  $Ce_{0.9}Ni_{0.1}O_{2-\delta}$  did exhibit additional surface hydroxyl species ( $O_\beta$ ). Therefore, we may conclude that the surface hydroxyl species may act as an active site in the NO reduction reaction.

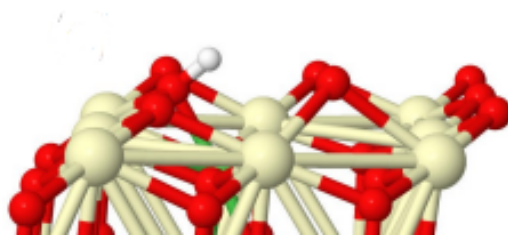


Figure 3.13: Adsorption configuration of surface hydroxyl over  $Ce_{1-x}Ni_xO_{2-\delta}$  formed by dissociative adsorption of  $H_2$

The above molecular mechanistic discussion concludes that the lattice oxygen, oxygen vacancy, and surface hydroxyl species played a crucial role in NO activation, whereas the mixed valences of Ni or Ce sites were not instrumental for the catalytic efficacy. The reduced  $Ce_{0.9}Ni_{0.1}O_{2-\delta}$  with a higher concentration of oxygen vacancies and surface hydroxyl species, therefore could demonstrate better NO activation vis à vis reduction ability compared to the oxidized material.

Furthermore, to assess whether N-O bond dissociation takes place during the reaction, we executed two NEB calculations to locate the transition states corresponding to two proposed pathways. The pathways included oxygen vacancy filling by O of NO and the formation of surface  $N_2O$  species from dual NO adsorption. In these calculations,  $NO_{2-1}$  and  $2NO_{v1}$  configurations were used because they were the energetically best adsorption configurations and also showed NO activation. Upon NO dissociation with  $NO_{2-1}$  configuration, oxygen vacancy was transferred from one site to the other by forming a new NO molecule with the lattice oxygen. The barrier required for this step was 1.29 eV. When  $2NO_{v1}$  was the initiating surface species, surface cis-ONNO type species was formed [129]. The reaction barrier for this step was only 0.88 eV. The comparative energetics along with optimized structures are shown in Figure 3.14. The analysis indicates that N-O bond dissociation took place during the reaction giving a surface  $N_2O$  species. We used these insights from DFT to develop mechanistic model of the reaction, as detailed in the following section.

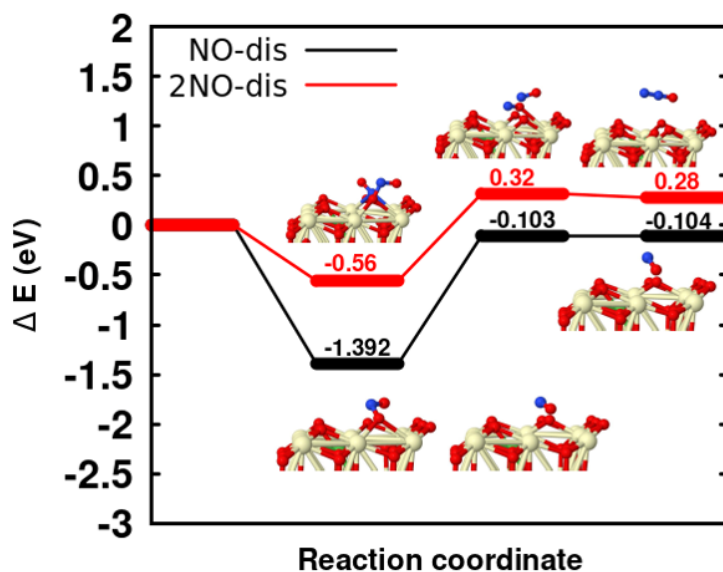


Figure 3.14: Comparison of energetics and the associated barriers for the formation of surface  $N_2O$  species

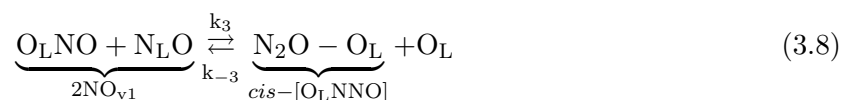
The generalized mechanism for  $NO_x$  reduction over  $Ce_{0.9}Ni_{0.1}O_{2-\delta}$  is proposed based on the DFT and XPS studies. As a first step, gas phase NO molecules adsorb reversibly on lattice oxygen ( $O_L$ ) and it was found to be the more stable and favorable site for adsorption as shown in Figures 3.10 and 3.12(a). The adsorbed species is indicated as  $O_LNO$  which corresponds to the adsorption configuration of  $NO_{2-1}$  shown in Figure 3.10(a).



The DFT simulations clearly showed another stable NO adsorption configuration over lattice vacancies with N being occupied in the lattice vacancy.



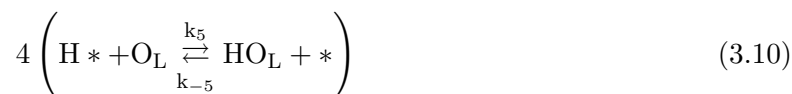
The two molecule adsorption configurations investigated using theoretical studies combining  $O_LNO$  and  $N_L O$  (indicated as  $2NO_{v1}$ ) were found to be stable as shown in Figures 3.11 and 3.12(b). The two molecule  $2NO_{v1}$  configuration was able to generate a transition state cis-(ONNO) type species, where one of the oxygen was lattice oxygen and it is indicated as  $N_2O - O_L$  species for the convenience of writing elementary steps.



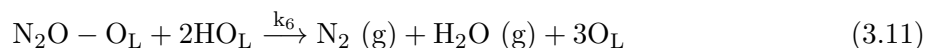
The dissociative adsorption of gas phase hydrogen is another favorable elementary step that takes place on surface Ni sites.



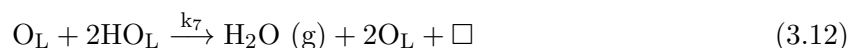
Chemisorbed H reacts with lattice oxygen ( $O_L$ ) and generates hydroxyl groups associated with lattice oxygen ( $HO_L$ ). The corresponding oxygen associated with hydroxyl groups ( $O_\alpha$  and  $O_\beta$ ) was found from O 1s spectra shown in Figure 3.3(c). Further, the adsorption configuration of  $HO_L$  groups was also confirmed using DFT studies as shown in Figure 3.13. Thus, the elementary step associated with hydroxyl groups was considered in the mechanism with the insight of XPS and DFT simulations.



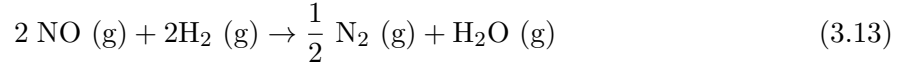
The stable intermediate  $N_2O - O_L$  reacts with  $HO_L$  group to generate  $N_2$  and  $H_2O$  by leaving the lattice oxygen sites vacant. From the light-off curves shown in Figure 3.5(a) and (b), the reduced  $Ce_{0.9}Ni_{0.1}O_{2-\delta}$  showed higher catalytic activity with 100% conversion at 240 °C, whereas as-prepared  $Ce_{0.9}Ni_{0.1}O_{2-\delta}$  showed merely 70% at the same temperature. It clearly indicates that the presence of lattice oxygen vacancies enhances the overall conversion of NO reduction. The DFT studies indicated that  $N_2O$  attached to lattice oxygen (cis-(ONNO) or  $N_2O - O_L$ ) as a transient state and surface chemical reaction was prominent with stable  $HO_L$  intermediate [129]. Thus, the surface chemical reaction of  $N_2O - O_L$  with  $HO_L$  is considered as a rate-limiting step. The role of lattice oxygen has also been investigated in our previous studies [65, 103, 130, 131].



Further,  $O_L$  reacts with  $HO_L$  and generates water by creating lattice oxygen vacancy.



The overall reaction after combining elementary steps (3.6) to (3.12) is,



By applying partial equilibrium for the reaction steps (3.6) to (3.8), the lattice coverages of intermediate species  $\text{N}_L\text{O}$ ,  $\text{O}_L\text{NO}$  and  $\text{N}_2\text{O-O}_L$  ( $\theta_{\text{N}_L\text{O}}$ ,  $\theta_{\text{O}_L\text{N}}$ , and  $\theta_{\text{N}_2\text{OO}_L}$ ) are obtained as follows:

$$\theta_{\text{O}_L\text{NO}} = K_1 P_{\text{NO}} \theta_{\text{O}_L}$$

$$\theta_{\text{N}_L\text{O}} = K_2 P_{\text{NO}} \theta_L$$

$$\theta_{\text{N}_2\text{OO}_L} = K_1 K_2 K_3 P_{\text{NO}}^2 \theta_L$$

The surface Ni sites facilitates  $\text{H}_2$  dissociation and the surface coverage of H ( $\theta_H$ ) is:  $\theta_H = K_4 P_{\text{H}_2}^{1/2} \theta_v$

Here,  $\theta_v$  is the coverage of vacant surface sites. As there are no surface groups other than adsorbed H, thus the surface site balance can be written as:

$$\theta_H + \theta_v = 1$$

Then,

$$\theta_H = \frac{K_4 P_{\text{H}_2}^{1/2}}{1 + K_4 P_{\text{H}_2}^{1/2}}$$

The partial equilibrium existing in the step (3.10) is:

$$K_5 \theta_H \theta_{\text{O}_L} = \theta_{\text{HO}_L} \theta_v$$

$$\theta_{\text{HO}_L} = K_4 K_5 P_{\text{H}_2}^{1/2} \theta_{\text{O}_L}$$

Here,  $\theta_{\text{O}_L}$  and  $\theta_{\text{HO}_L}$  are the coverages of lattice oxygen ( $\text{O}_L$ ) and  $\text{HO}_L$  species. By applying pseudo-steady state equilibrium for elementary steps (3.11) and (3.12), the variation in the coverage of lattice oxygen over time can be written as follows:

$$\frac{d\theta_{\text{O}_L}}{dt} = 0 = \frac{k_6}{3} \theta_{\text{N}_2\text{OO}_L} \theta_{\text{HO}_L}^2 - k_7 \theta_{\text{O}_L} \theta_{\text{HO}_L}^2 + \frac{k_7}{2} \theta_{\text{O}_L} \theta_{\text{HO}_L}^2$$

$$\theta_{\text{O}_L} = \frac{2k_6}{3k_7} K_1 K_2 K_3 P_{\text{NO}}^2 \theta_L$$

Here,  $\theta_L$  is the coverage of lattice oxygen vacancy. As all the lattice coverage expressions are derived, the vacant lattice coverage ( $\theta_L$ ) can be obtained by the lattice site balance given below:

$$\theta_{OLNO} + \theta_{NO_L} + \theta_{N_2OO_L} + \theta_{HO_L} + \theta_{O_L} + \theta_L = 1$$

$$\theta_L = \frac{1}{\left(1 + K_2 P_{NO} + K_1 K_2 K_3 P_{NO}^2 \left(1 + \frac{2k_6}{3k_7} + K_4 K_5 \frac{2k_6}{3k_7} P_{H_2}^{1/2}\right) + K_1^2 K_2 K_3 \frac{2k_6}{3k_7} P_{NO}^3\right)}$$

By considering elementary step (3.11) as rate-limiting step, the reaction rate is written as:

$$\text{Rate, } R = k_6 \theta_{N_2OO_L} \theta_{HO_L}^2$$

$$R = \frac{(K_1 K_2 K_3 k_6)^3 (2 K_4 K_5 / 3k_7)^2 P_{NO}^6 P_{H_2}}{\left(1 + K_2 P_{NO} + K_1 K_2 K_3 P_{NO}^2 \left(1 + \frac{2k_6}{3k_7} + K_4 K_5 \frac{2k_6}{3k_7} P_{H_2}^{1/2}\right) + K_1^2 K_2 K_3 \frac{2k_6}{3k_7} P_{NO}^3\right)^3}$$

As it is a complex nonlinear equation, rewriting in the reciprocal terms would make it easier to perform non-linear regression to find the kinetic parameters. At constant partial pressure of  $H_2$ , the overall reaction rate expression can be reduced as:

$$\frac{1}{R^{1/3}} = \left( \frac{A}{P_{NO}^2} + \frac{B}{P_{NO}} + 1 \right) C + D P_{NO}$$

Here,

$$A = \left( \frac{1.31}{K_1 K_2 K_3 k_6 P_{H_2}^{1/3}} \right) \left( \frac{k_7}{K_4 K_5} \right)^{2/3}$$

$$B = \left( \frac{1.31}{K_1 K_3 k_6 P_{H_2}^{1/3}} \right) \left( \frac{2k_7}{K_4 K_5} \right)^{2/3}$$

$$C = \left( \frac{1.31}{k_6 P_{H_2}^{1/3}} \right) \left( \frac{2k_7}{K_4 K_5} \right)^{2/3} \left\{ 1 + \frac{2k_6}{3k_7} + K_4 K_5 \frac{2k_6}{3k_7} P_{H_2}^{1/2} \right\}$$

$$D = \frac{0.7631 K_1}{(k_7 P_{H_2})^{1/3} (K_4 K_5)^{2/3}}$$

From the theoretical insights, the utilization of lattice oxygen was found to be prominent. Thus, the corresponding rate constant ( $k_7$ ) would also be prominent and possess a high order of magnitude. The last two terms contain  $k_7$  in the denominator and it can be a reasonable assumption to neglect the contribution compared to the first term. Then, the expression for C will be:



$$C \approx \left( \frac{1}{k_6 P_{H_2}^{1/3}} \right) \left( \frac{2k_7}{K_4 K_5} \right)^{2/3}$$

Arrhenius's theory was considered for expressing rate constant, whereas the mathematical form of equilibrium constant was expressed by transition state theory, as the elementary steps contain various intermediates. The generalized notations for rate and equilibrium constants are as follows:

$$k_i = k_{i0} \exp\left(\frac{-E_i}{RT}\right)$$

$$K_j = K_{j0} T \exp\left(\frac{H_j}{RT}\right)$$

$k_{i0}$  and  $K_{j0}$  are pre-exponential factors of irreversible and equilibrium elementary steps ( $i=(3.11)$  and  $(3.12)$ ;  $j=(3.6)$  to  $(3.10)$ ),  $E_i$  and  $H_j$  are the activation energy of  $i^{th}$  reaction step and enthalpy of  $j^{th}$  reaction step. The modified A, B, C, and D parameters are:

$$A = \left( \frac{1.31}{K_{10}K_{20}K_{30}k_{60}T^3P_{H_2}^{1/3}} \right) \left( \frac{k_{70}}{K_{40}K_{50}T^2} \right)^{2/3} \exp\left(\frac{-H_1 - H_2 - H_3 + E_6 - \frac{2}{3}(H_4 + H_5 - E_7)}{RT}\right)$$

$$= \frac{K_{A0}C}{T^3} \exp\left(\frac{-H_A}{RT}\right)$$

$$B = \left( \frac{1.31}{K_{10} K_{30}k_{60} T^2P_{H_2}^{1/3}} \right) \left( \frac{k_{70}}{K_{40} K_{50} T^2} \right)^{2/3} \exp\left(\frac{-H_1 - H_3 + E_6 - 2/3(H_4 + H_5 - E_7)}{RT}\right)$$

$$= \frac{K_{B0}C}{T^2} \exp\left(\frac{-H_B}{RT}\right)$$

$$C \approx \left( \frac{1.31}{k_{60}} \right) \left( \frac{k_{70}}{K_{40} K_{50} T^2P_{H_2}^{1/3}} \right)^{2/3} \exp\left(\frac{E_6 - 2/3(H_4 + H_5 - E_7)}{RT}\right)$$

$$\approx \frac{K_{C0}}{P_{H_2}^{1/3} T^{4/3}} \exp\left(\frac{H_C}{RT}\right)$$

$$D = \frac{0.7631 K_{10}}{(k_{70}P_{H_2})^{1/3} (K_{40} K_{50} T^2)^{2/3}} \exp\left(\frac{H_1 + E_1 - 2/3(H_4 + H_5)}{RT}\right)$$

$$= \frac{K_{D0}}{P_{H_2}^{1/3} T^{4/3}} \exp\left(\frac{H_D}{RT}\right)$$

Thus, the final rate expression is modified as follows:

$$\frac{1}{R^{1/3}} = \left( \frac{K_{A0} \exp\left(\frac{-H_A}{RT}\right)}{T^3} \frac{1}{P_{NO}^2} + \frac{K_{B0} \exp\left(\frac{-H_B}{RT}\right)}{T^2} \frac{1}{P_{NO}} + 1 \right) \frac{K_{C0} \exp\left(\frac{H_C}{RT}\right)}{P_{H_2}^{1/3} T^{4/3}} + \frac{K_{D0} \exp\left(\frac{H_D}{RT}\right)}{P_{H_2}^{1/3} T^{4/3}} P_{NO}$$

A Levenberg–Marquardt algorithm was implemented for the nonlinear regression of the temperature -dependent rate expression. The kinetic parameters were estimated for the data of  $\frac{1}{R^{1/3}}$  vs  $\frac{10^3}{P_{NO}}$  vs at a constant partial pressure of  $H_2$  ( $P_{H_2}=506.17$  Pa), the rate (R) and partial pressure of NO ( $P_{NO}$ ) are considered in  $\text{mmol}(\text{gcatol}\cdot\text{min})^{-1}$  and  $P_a$ . Figure 3.15 (a) and (b) shows the nonlinear regression fit for as-prepared and reduced  $Ce_{0.9}Ni_{0.1}O_{2-\delta}$  catalysts. The goodness of

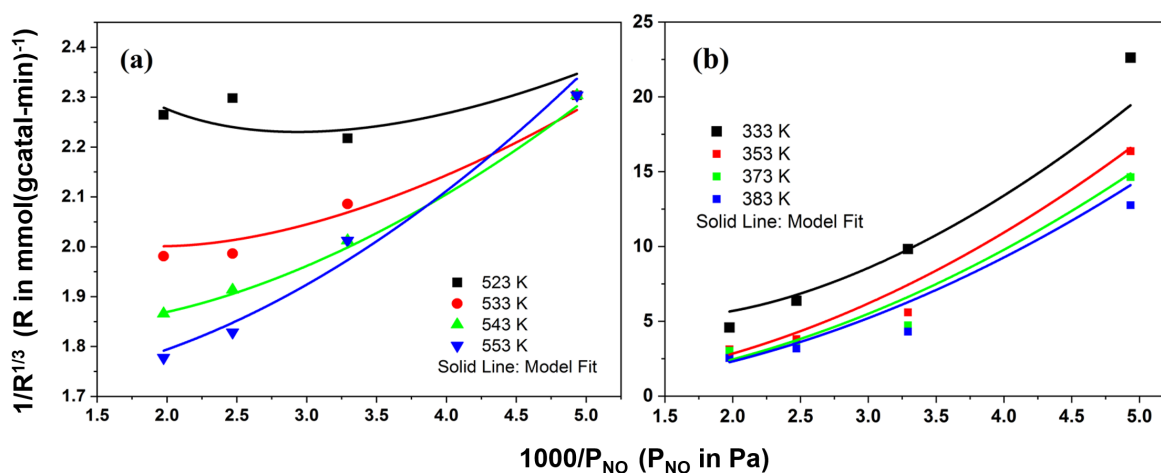


Figure 3.15: Reaction rate variation with respect to partial pressure of NO in terms of  $\frac{1}{R^{1/3}}$  vs  $\frac{10^3}{P_{NO}}$  plot at a constant partial pressure of  $H_2$  ( $P_{H_2}=506.17$  Pa) for (a) as-prepared and (b) reduced  $Ce_{0.9}Ni_{0.1}O_{2-\delta}$  catalysts

the fit was found to be 0.964 and 0.952 for both as-prepared and reduced  $Ce_{0.9}Ni_{0.1}O_{2-\delta}$  catalysts. Interestingly,  $K_{C0}$  parameter containing the rate-limiting step term was found to be  $2.149 \pm 0.012 \times 10^{-2}$  for reduced  $Ce_{1-x}Ni_xO_{2-\delta}$ , and  $3154 \pm 82$  for as-prepared  $Ce_{0.9}Ni_{0.1}O_{2-\delta}$ . This indicates the contribution of rate-limiting step due to the elementary step (3.11) is prominent for reduced  $Ce_{0.9}Ni_{0.1}O_{2-\delta}$  (as it contains  $k_{60}$  parameter in reciprocal term) than that of as-prepared material. The combined kinetic parameters are listed in Table 3.2. The developed kinetic model validates the experimental rates for both as-prepared and reduced. The parity plot shown in Figure 3.16 has the experimental and predicted rates corresponding to both as prepared and reduced  $Ce_{0.9}Ni_{0.1}O_{2-\delta}$  catalysts. The goodness of the fit for the parity plot was

obtained as 0.963, which further confirms the validity of the generalized reaction rate expression.

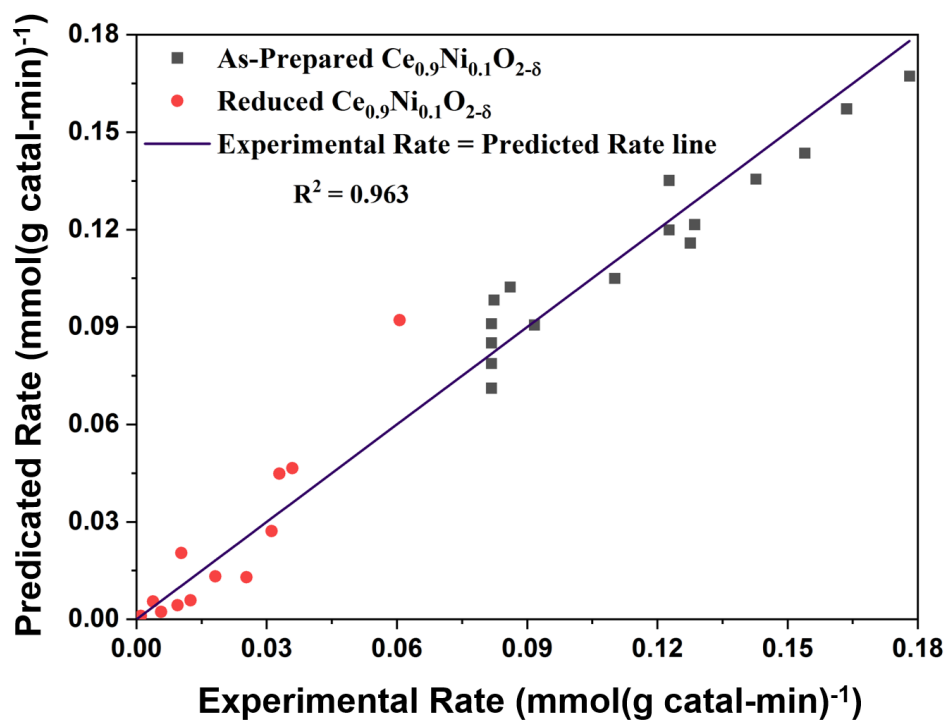


Figure 3.16: Parity plot to compare model-predicted and experimental reaction rates

Table 3.2: Kinetic parameters for as-prepared and reduced  $Ce_{0.9}Ni_{0.1}O_{2-\delta}$

Parameters	As-prepared $Ce_{0.9}Ni_{0.1}O_{2-\delta}$	Reduced $Ce_{0.9}Ni_{0.1}O_{2-\delta}$
$K_{A0}$	$(1.197 \pm 0.034) \times 10^{14}$	$(4.114 \pm 0.034) \times 10^{13}$
$K_{B0}$	$26747 \pm 145$	$(1.112 \pm 0.019) \times 10^6$
$K_{C0}$	$3154 \pm 82$	$(2.149 \pm 0.012) \times 10^{-2}$
$K_{D0}$	$(2.668 \pm 0.162) \times 10^{-19}$	$(8.189 \pm 0.121) \times 10^{-19}$
$H_A/R$	$9727 \pm 281$	$925.9 \pm 15.6$
$H_B/R$	$18656 \pm 1505$	$9382 \pm 372$
$H_C/R$	$483 \pm 22$	$52.91 \pm 2.21$
$H_D/R$	$26851 \pm 1248$	$17772 \pm 761$
$R^2$	0.964	0.952

### 3.6 Conclusion

Solid solutions of nanocrystalline  $Ce_{1-x}Ni_xO_{2-\delta}$  ( $x = 0.05, 0.1,$  and  $0.2$ ) were synthesized by a single step solution combustion synthesis method.  $Ce_{0.95}Ni_{0.05}O_{2-\delta}$  and  $Ce_{0.9}Ni_{0.1}O_{2-\delta}$  crystallized in a pure face-centered cubic fluorite structure with a perfect substitution of Ni in

Ce sites, whereas  $Ce_{0.9}Ni_{0.1}O_{2-\delta}$  exhibited precipitation of NiO phase due to the high amount of doping. The substituted Ni was in its bivalent ionic state and Ce was observed in a tetravalent state. The aliovalent doping created oxygen vacancies that were clearly evident from the XPS studies. Upon reduction at elevated temperatures, the core level O 1s spectra showed the formation of a higher amount of oxygen vacancy and newer surface hydroxyl species. The NO reduction over the as-prepared and reduced  $Ce_{1-x}Ni_xO_{2-\delta}$  apparently showed the importance of oxygen vacancies and surface hydroxyl species as active sites in the molecular mechanism. The periodic DFT calculations on NO and H<sub>2</sub> adsorption on (111) plane of CeO<sub>2</sub> corroborated the role of active sites as observed experimentally. The minimum energy path during the surface reactions was further calculated and based on the proposition a generalized kinetic model of NO reduction by H<sub>2</sub> was developed over  $Ce_{1-x}Ni_xO_{2-\delta}$  materials. The kinetic modeling identified the rate-limiting step of the NO reduction reaction. The investigation stands as a comprehensive study of identifying the active sites and understanding the molecular mechanism of NO<sub>x</sub> reduction over supported metal catalysts.

## Chapter 4

# Rags to Riches: Meliorating the Electrocatalytic Reduction of Nitrate to Ammonia over Cu-based Nano-alloys

### 4.1 Introduction

In spite of multiple investigations probing the  $\text{NO}_x\text{RR}$  mechanism, activity, and selectivity [52, 132–134] there is a significant scope to improve the sluggish kinetics and poor selectivity of this complex reaction process that involves eight electron and nine proton transfers [135]. Platinum group metals were measured to have  $\text{NO}_x$  reduction reaction ( $\text{NO}_x\text{RR}$ ) activities of  $\text{Rh} > \text{Ru} > \text{Ir} > \text{Pd} \approx \text{Pt}$  in acidic conditions at potentials ranging from 0 to 0.4 V vs RHE [132]. The transition metals are typically less active than precious metals, with the exception of Cu [136]. Electrocatalysis is a surface phenomenon, the high dispersion of the nano-sized transition metal active sites over conductive support can transform the transition metals into highly active catalysts. In this regard, one of the most popular approaches is to develop MOF derived nanocatalysts through high temperature pyrolysis process, where the uniform distribution of metals can be fabricated onto carbon support [137–139]. These materials showcased high dispersity of metals, modification of electronic structure by doping of heteroatoms, and stability owing to the metal-carbon interaction [140, 141].

Recently, Cu-based materials have been reported to be very active electrocatalysts for  $\text{NO}_x\text{RR}$  due to their suitable electronic structure and also have superiority over noble metals in terms of cost and abundance [142]. Still, the reports in the present literature highlight the thermodynamically favorable, however unselective HER as a primary challenge of  $\text{NO}_x\text{RR}$  over the pristine Cu-based catalysts. Therefore, to tackle the particular problem of HER and enhance the selectivity of the desired product ammonia, the catalysts should be designed meticulously [143]. Contextually, the bimetallic nano-alloy catalysts have shown exceptional electrocatalytic performances in  $\text{NO}_x\text{RR}$  [58, 144–146],  $\text{CO}_2\text{RR}$  [147], overall water splitting [148], electrochemical energy storage [149], OER [150], and as microbial fuel cell [151]. Introduction of another metal into the Cu lattice helps in better catalytic activity apparently due to the shift in the  $d$ -band center [152]. The  $d$ -band engineering facilitates the tailoring of the Fermi level position, which is correlated with the binding energies of the catalyst and the adsorbed intermediates [153].

Therefore, herein we report the synthesis of carbon-supported Cu-based nano-alloys, such as  $\text{Cu}_{0.85}\text{Ni}_{0.15}/\text{C}$  and  $\text{Cu}_{0.85}\text{Zn}_{0.15}/\text{C}$  from the corresponding bimetallic MOFs and their exploration for  $\text{NO}_x\text{RR}$  at neutral pH. The fundamental idea is to arrest the HER, enhancing the  $\text{NH}_3$  selectivity by tuning the  $d$ -bands near the Fermi level position to invoke a better  $\text{NO}_x\text{RR}$  catalysis. The study probes the detailed kinetics of  $\text{NO}_x\text{RR}$  over the nano-alloys of  $\text{Cu}_{0.85}\text{Ni}_{0.15}/\text{C}$  and  $\text{Cu}_{0.85}\text{Zn}_{0.15}/\text{C}$  in comparison to the pristine Cu/C and correlates the catalytic activity with the electronic structure derived from the first principle calculations.

## 4.2 Materials and Methods

### 4.2.1 Synthesis of Catalysts

For the synthesis of MOF materials, the metal precursors used were  $\text{Cu}(\text{NO}_3)_2 \cdot 3\text{H}_2\text{O}$ ,  $\text{Ni}(\text{NO}_3)_2 \cdot 3\text{H}_2\text{O}$ , and  $\text{Zn}(\text{NO}_3)_2 \cdot 6\text{H}_2\text{O}$  from S D Fine Chem. Ltd. (India), while the organic linker 1,3,5-benzene tricarboxylic acid (BTC) was purchased from Sigma-Aldrich. The solvents used for the synthesis were: N, N-dimethylformamide (DMF), isopropanol (IPA), and ethanol (EtOH) from S D Fine Chem. Ltd. (India). Nafion solution (Sigma-Aldrich) with the composition of 5 wt.% in a mixture of alcohol and water (containing 45% water) was used as a binder for the working electrode. Potassium dihydrogen orthophosphate ( $\text{KH}_2\text{PO}_4$ ) obtained from SRL Pvt. Ltd. was used as electrolyte and potassium nitrate ( $\text{KNO}_3$ ) from Sigma-Aldrich was used as the nitrate source. The products were analyzed using the following chemicals: sodium hydroxide ( $\text{NaOH}$ ) (SRL Pvt.

Ltd.), salicylic acid ( $C_7H_6O_3$ ) (S D Fine CHEM Ltd.), sodium citrate ( $Na_3C_6H_5O_7 \cdot 2H_2O$ ) (S D Fine Chem Ltd.), sodium hypochlorite pentahydrate ( $NaClO \cdot 5H_2O$ ) (TCI), sodium nitro-ferricyanide ( $C_5FeN_6Na_2O$ ) (S D Fine Ltd.), N-(1-Naphthyl)ethylenediamine dihydrochloride ( $C_{12}H_{14}N_2 \cdot 2HCl$ ) (Sigma-Aldrich), sulfanilamide ( $H_2NC_6H_4SO_2NH_2$ ) (Sigma-Aldrich), sulfamic acid ( $NH_2SO_3H$ ), HCl (37%) (Merck), *p*-(dimethylamino)benzaldehyde ( $(CH_3)_2NC_6H_4CHO$ ) (Sigma-Aldrich), and phosphoric acid ( $H_3PO_4$ ) (Sigma-Aldrich). The chemicals in the experiments were used without any further purification. The required solutions were made with ultrapure water (18.2 M $\Omega$  cm, Millipore Milli-Q).

Solvothermal method was implemented in the synthesis of mono-metallic and bimetallic MOFs. In a typical synthesis of Cu-BTC, 4.2 mmol of  $Cu(NO_3)_2 \cdot 3H_2O$  and 4.8 mmol of BTC were mixed in the 30 mL solution containing ultrapure water, EtOH and DMF in the ratio 1:1:1 and was stirred for 1 h. The blue-colored solution was transferred into 50 mL Teflon-lined stainless steel autoclave and the autoclave was then kept in a preheated oven at 120 °C for 24 h. The resultant product was filtered and washed with DMF and water several times. The blue-coloured filtrate was then kept in a vacuum oven at 80 °C to dry overnight. The bimetallic MOFs,  $Cu_{0.85}Ni_{0.15}$ -BTC, and  $Cu_{0.85}Zn_{0.15}$ -BTC MOF were synthesized in a similar manner with  $Ni(NO_3)_2 \cdot 6H_2O$  as Ni precursor and  $Zn(NO_3)_2 \cdot 6H_2O$  as Zn precursor according to their molar ratios. As per the previous report [138], only 15% of Ni and Zn could be incorporated into the pristine Cu-BTC. The as-prepared monometallic and bimetallic MOFs were converted into the nano-catalysts of Cu/C,  $Cu_{0.85}Ni_{0.15}$ /C and  $Cu_{0.85}Zn_{0.15}$ /C by heating the precursor MOFs at 500 °C in a reducing atmosphere, wherein 10%  $H_2$  balanced by He was continuously passed through the sample in a tubular furnace at a heating rate of 10 °C  $min^{-1}$  for 3 h.

#### 4.2.2 Characterizations

To affirm the as-prepared MOFs and MOF-derived nano-catalysts' structural information, XRD pattern was recorded using Rigaku Ultima IV diffractometer with Cu  $K_\alpha$  radiation ( $\lambda=1.5418$  Å) at a scan rate of 0.4°  $min^{-1}$  and with a step size of 0.01°. Using Scherrer's formula the average crystallite diameters were calculated for the nano-catalysts. The structural information of the nano-catalysts was further elucidated by using HR-TEM carried out using JEM 2100 with an operating voltage of 200 kV and a resolution of 2.4 Å. The morphology of the as-prepared samples was observed through FE-SEM using FEI-Apreo S. To study in detail about the surface chemical species of the prepared samples, XPS were procured with Thermo Scientific Multilab

2000 with Al  $K_{\alpha}$  radiation (1486.6 eV) operated at 15 kV. The XPS was plotted with respect to the C 1s with the binding energy of 284.8 eV.

The electrochemical measurements were carried out using OrigaFlex-OGF500 potentiostat at room temperature unless specified. The experiments were carried out in an air-tight single-compartment cell using three electrode system with the nano-catalyst drop casted on a glassy carbon electrode as the working electrode, Ag/AgCl (sat. KCl) as the reference electrode and Pt wire as the counter electrode. About 5 mg of the as-prepared nano-catalysts were dispersed into the mixture containing 0.5 mL IPA and 50  $\mu$ L Nafion and was ultra-sonicated for 2 h. 10  $\mu$ L of the catalyst solution was then drop casted onto the glassy carbon electrode. All three electrodes were dipped in solution containing 0.1M PBS and 1000 ppm  $KNO_3$  and the pH of the electrolyte was maintained at 7. Prior to the start of the electrochemical tests, the electrolyte was purged with Ar gas to remove the  $N_2$  and  $O_2$  from the cell for 15 min. Linear Scan Voltammetry (LSV) was obtained in the range of 0.6 to -1.4 V at different scan rates of 30 to 90  $mVs^{-1}$  to assess the catalytic activity for nitrate reduction. The electrochemical nitrate reduction of the catalysts was tested in the chronoamperometric mode for 2 h. The experiments were conducted with Ag/AgCl (sat. KCl) as reference electrode and potentials were converted to reversible hydrogen electrode (RHE) scale using the formula:  $E_{Ag/AgCl} + (0.0591 \times pH) + 0.197V$ . Electrical impedance spectra (EIS) measurements were carried out using a Biologic SP-150 CV instrument by applying AC voltage in the frequency range from 0.01 Hz to 100 kHz. To examine the ECSA of the catalysts were evaluated by chronoamperometry fast method.

The products were quantified using Jasco-V650 UV spectrophotometer. The concentration of  $NH_3$  after the reaction was determined by colorimetry with the help of the indophenol method. About 1M NaOH, 5 wt.% sodium citrate, and 5 wt.% salicylic acid were added to 2 mL of diluted electrolyte. After which 1 mL of 0.05M sodium hypochlorite and 0.2 mL of 1 wt.% sodium nitroferricyanide were added to the previous solution and the mixture was kept for 2 h at room temperature before measuring the absorbance at a wavelength of 660 nm. The calibration graph was plotted from different concentrations of  $NH_4Cl$  as the ammonia source. The nitrite ( $NO_2^-$ ) concentration was estimated by the Griess test. The reagent was prepared by adding 0.2 g N-(1-Naphthyl)ethylenediamine dihydrochloride, 4 g of sulfanilamide, 10 mL of phosphoric acid, and 50 mL of DI water. About 0.1 mL of the prepared reagent was added into the 5 mL of the dilute electrolyte solution and was kept still for 30 min at room temperature before measuring the absorbance at a wavelength of 540 nm. The calibration plot was prepared by using different concentrations of  $KNO_2$  as the  $NO_2^-$  source. The presence of  $N_2H_4$  in the electrolyte was also



tested by using Watt and Chrisp's method. The chromogenic reagent was prepared using 5.99 g of *p*-(dimethylamino)benzaldehyde, 30 mL of concentrated HCl, and 300 mL of CH<sub>3</sub>OH. The calibration plot was plotted using different concentrations of hydrazine hydrate solution. The gaseous product H<sub>2</sub> was measured using a portable Gas Chromatograph from Mayura Analytical Private Limited, India.

The performance of the catalysts was evaluated by the Faradaic efficiency of ammonia (FE<sub>NH<sub>3</sub></sub>) and nitrite (FE<sub>NO<sub>2</sub><sup>-</sup></sub>), Yield rate of ammonia (Y<sub>NH<sub>3</sub></sub>) and nitrite (Y<sub>NO<sub>2</sub><sup>-</sup></sub>), Conversion rate of nitrate (C<sub>NO<sub>3</sub><sup>-</sup></sub>), Selectivity of ammonia (S<sub>NH<sub>3</sub></sub>), Energy efficiency of ammonia (EE<sub>NH<sub>3</sub></sub>), which were calculated using the equations given below:

$$FE_{NH_3}(\%) = \frac{8 \times F \times C_{NH_3} \times V}{17 \times Q} \times 100\% \quad (4.1)$$

$$FE_{NO_2^-}(\%) = \frac{2 \times F^2 C_{NO_2^-} \times V}{46 \times Q} \times 100\% \quad (4.2)$$

$$Y_{NH_3} = \frac{C_{NH_3} \times V}{A \times t} \quad (4.3)$$

$$Y_{NO_2^-} = \frac{C_{NO_2^-} \times V}{A \times t} \quad (4.4)$$

$$C_{NO_3^-}(\%) = \left( 1 - \frac{C_t(NO_3^-)}{C_0(NO_3^-)} \right) \times 100\% \quad (4.5)$$

$$S_{NH_3}(\%) = \frac{n_t(NH_3)}{n_0(NO_3^-) - n_t(NO_3^-)} \times 100\% \quad (4.6)$$

$$EE_{NH_3}(\%) = \frac{(1.23 - E_{NH_3}^o) FE_{NH_3}}{1.23} \times 100\% \quad (4.7)$$

Here, C<sub>NH<sub>3</sub></sub> is the concentration of ammonia (ppm), C<sub>NO<sub>2</sub><sup>-</sup></sub> is the concentration of nitrite (ppm), V is the volume of electrolyte (mL), Q is the total charge passed through the electrode (C), F is the Faraday constant (96,485 C mol<sup>-1</sup>), A is the geometric area of the working electrode (cm<sup>2</sup>), t is the electrolysis time (h), n<sub>t</sub>(NH<sub>3</sub><sup>-</sup>) is the mole concentration of the ammonia formed at time t, n<sub>0</sub>(NO<sub>3</sub><sup>-</sup>) and n<sub>t</sub>(NO<sub>3</sub><sup>-</sup>) are the molar concentration of nitrate at the initiation of the reaction and at time t, respectively. E<sub>NH<sub>3</sub></sub><sup>o</sup> is the equilibrium potential of nitrate to ammonia (0.69 V). The kinetics of the electrochemical reactions were evaluated with the help of Tafel slopes, rate constants, and the activation energy. LSV curves acquired at different scan rates were used to inspect the reaction mechanism based on the relationship between the peak current density and

the scan rate. The activation energy was found from cyclic voltammetry curves at  $50 \text{ mV s}^{-1}$  scan rate at different temperatures from room temperature to  $105 \text{ }^\circ\text{C}$  with an interval of  $20 \text{ }^\circ\text{C}$ .

The DFT based first-principle calculations were performed in Atomixtix Tool Kit (ATK) and Virtual Nano Lab (VNL), commercially available simulation packages from Synopsys QuantumWise. The DFT calculations were performed using the linear combination of atomic orbitals (LCAO) basis sets, where  $k$  points in the Brillouin zone were sampled using the  $8 \times 8 \times 1$  Monkhorst-Pack grid with a density mesh cut-off energy of 100 Hartree. Initially, the pristine Cu was considered from the materials library of ATK, and a (111) surface was constructed from the bulk Cu in a bilayer configuration. The (111) surface of Cu was considered in  $(3 \times 1 \times 1)$  supercell configuration having 6 Cu atoms on its surface and with a vacuum of  $40 \text{ \AA}$  in the out-of-plane direction to eliminate the interaction of periodic images on the cleaved surface. The (111) surface of Cu was relaxed for minimum energy and minimum force per atom configuration through the geometry optimization technique using the Limited-memory Broyden Fletcher Goldfarb Shanno (LBFGS) algorithm with the pressure and force tolerance of  $0.0001 \text{ eV \AA}^{-3}$  and  $0.01 \text{ eV \AA}^{-1}$ , respectively. During geometry optimization, the GGA method with the PBE exchange-correlation functional was considered for DFT calculation. Next, one Cu atom on the supercell surface was consecutively substituted with Ni and Zn atoms to obtain Ni-doped and Zn-doped Cu surfaces with a composition of  $\text{Cu}_{0.85}\text{Ni}_{0.15}$  and  $\text{Cu}_{0.85}\text{Zn}_{0.15}$ . The doped surfaces were then relaxed following the procedure described before. In the next phase, following the reaction pathway of  $\text{NH}_3$  generation, the different intermediate species ( $\text{NO}_3$ ,  $\text{NO}_2$ ,  $\text{NO}$ ,  $\text{NH}_2\text{OH}$ , and  $\text{NH}_3$ ) were introduced on the pristine and doped surfaces with different molecular orientations. The individual adsorbed/adsorbent systems were then relaxed following a similar process. During the optimization, Grimme DFT-D3 dispersion correction was incorporated with the GGA-PBE method to account for the effects of the Van der Waals (VdW) interactions between the adsorbed and adsorbent. Moreover, the counterpoise (CP) correction was also considered to address the inherent Basis Set Superposition Error (BSSE) for two or more subsystems for the LCAO basis. The strength of molecular adsorption of different species on different surfaces was quantified from the adsorption energy ( $E_{\text{Adsorption}}$ ), which is defined as follows:

$$E_{\text{Adsorption}} = E_{\text{Surface\_Adsorbed}} - E_{\text{Surface}} \quad (4.8)$$

where,  $E_{\text{Surface}}$  and  $E_{\text{Surface\_Adsorbed}}$  are the ground state energies of the pristine/doped surfaces before and after adsorption, respectively. It is apparent that for stable adsorption,  $E_{\text{Adsorption}} < 0$

must be observed, whereas for good electrochemical activity, a moderate  $E_{\text{Adsorption}}$  value should be expected.

## 4.3 Results and Discussion

### 4.3.1 Structural, Surface and Electronic Properties

The powder XRD patterns and the corresponding FE-SEM micrographs of the as-prepared monometallic MOF Cu-BTC and the bimetallic MOFs  $\text{Cu}_{0.85}\text{Ni}_{0.15}\text{-BTC}$  and  $\text{Cu}_{0.85}\text{Zn}_{0.15}\text{-BTC}$  are provided in Figure 4.1. The diffractograms inferred a face-centered cubic structure of the synthesized MOFs, and the incorporation of Ni and Zn into the Cu- BTC MOF resulted in a clear formation of a solid solution framework. The MOF particles had an octahedral morphology

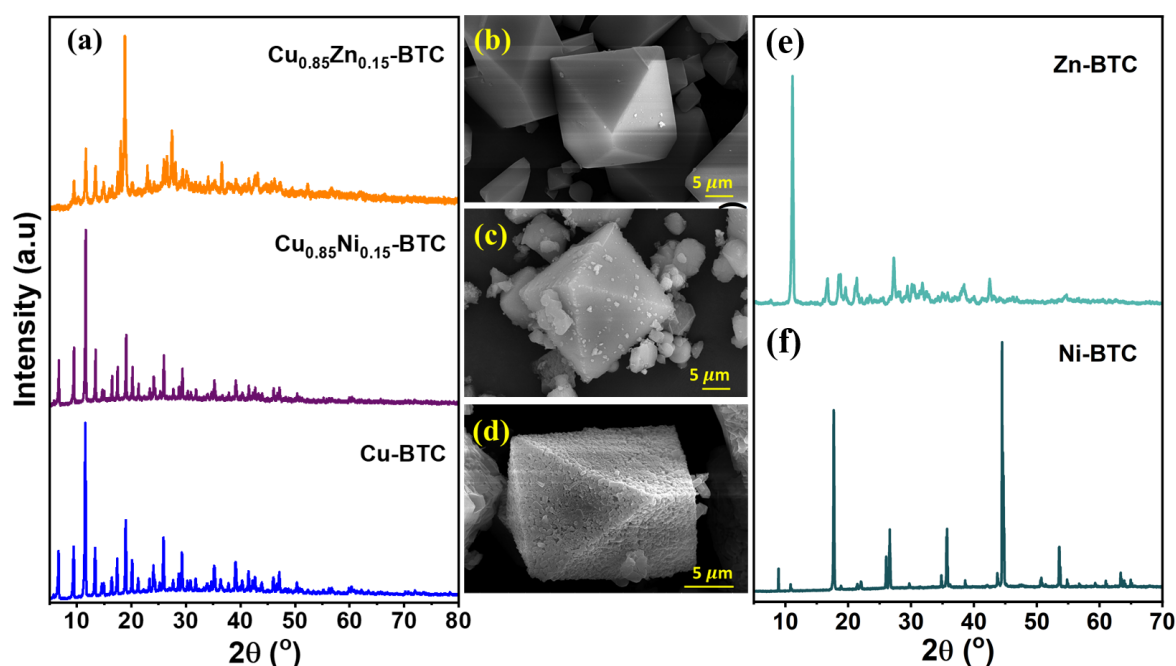


Figure 4.1: The powder (a) XRD patterns (b-d) the corresponding FE-SEM micrographs of the as-prepared monometallic MOF Cu-BTC, and the bimetallic MOFs  $\text{Cu}_{0.85}\text{Ni}_{0.15}\text{-BTC}$  and  $\text{Cu}_{0.85}\text{Zn}_{0.15}\text{-BTC}$ , and (e,f) XRD patterns of Zn-BTC, and Ni-BTC

with an average size of 16-21  $\mu\text{m}$ . The high temperature pyrolysis of the corresponding MOFs resulted in the monometallic and the bimetallic carbon-supported nano- alloy catalysts.  $\text{Cu/C}$ ,  $\text{Cu}_{0.85}\text{Ni}_{0.15}/\text{C}$  and  $\text{Cu}_{0.85}\text{Zn}_{0.15}/\text{C}$  crystallized in phase pure face-centered cubic structure with the space group  $Fm\bar{3}m$  (JCPDS No.:04- 0836) as can be observed in Figure 4.2(a), (d), and (g).

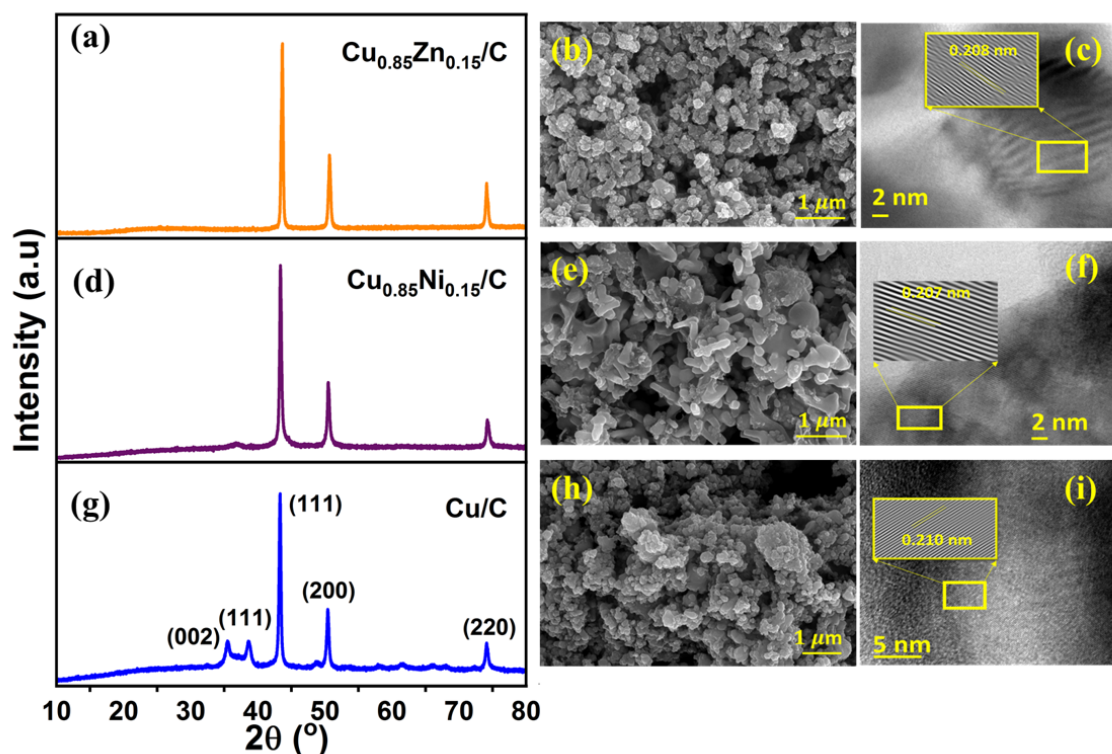


Figure 4.2: The powder XRD patterns and the corresponding FE-SEM micrographs of the as-prepared (a-c) Cu/C, (d-f) Cu<sub>0.85</sub>Ni<sub>0.15</sub>/C, and (g-i) Cu<sub>0.85</sub>Zn<sub>0.15</sub>/C

The diffraction peak corresponding to the support carbon was mostly obscured in all three patterns. The average crystallite size for all three nano-catalysts found from the (111) plane was in the range of 26-35 nm. Among the three materials, Cu/C exhibited the formation of crystalline CuO at  $2\theta=35.5^\circ$  (002) and  $2\theta=38.7^\circ$  (111). The FE-SEM micrographs of the monometallic and the bimetallic nano-alloy catalysts in Figure 4.2(b), (e), and (h) indicate the formation of irregularly shaped nanoparticles. The interplanar distances of  $d_{111}$  calculated from the HR-TEM micrographs of Figure 4.2(c), (f), and (i) matched well with the XRD patterns. The metals were observed to be distributed in a highly dispersed manner over the carbonaceous support (Figure 4.3). To unveil the structural information of the support carbon, Raman spectra were collected and the data are plotted in Figure 4.4. Apparently, the two distinct broad peaks of defect mediated D band and ordered graphitic G band were observed over all three nano-alloys. The D band is ascribed as defect activated band, which originates from the lattice mismatch of the graphite layers, whereas the G band is associated with a graphite-derived spectrum of  $E_{2g}$  mode of  $sp^2$  carbon atoms in a hexagonal lattice, justifying the presence of crystalline graphitic carbon. The relative intensity ratio of the D and G band ( $I_D/I_G$ ) was found to be highest in the case of Cu<sub>0.85</sub>Zn<sub>0.15</sub>/C, followed by Cu<sub>0.85</sub>Ni<sub>0.15</sub>/C, whereas the monometallic Cu/C exhibited

the lowest  $I_D/I_G$  ratio. The data suggest that  $\text{Cu}_{0.85}\text{Zn}_{0.15}/\text{C}$  possesses the highest concentration of defect carbon among the three catalysts. To compare the electrocatalytic activity and evaluate the performances pristine Zn-BTC and Ni-BTC MOFs were also synthesized and then reduced to monometallic alloys of Zn/C and Ni/C respectively.

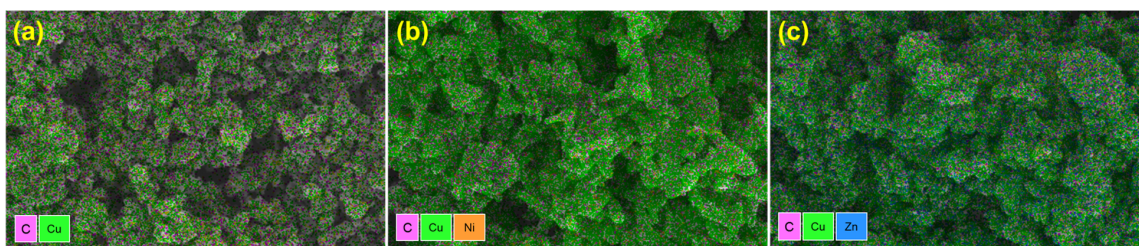


Figure 4.3: FE-SEM EDAX Mapping of (a)  $\text{Cu}/\text{C}$ , (b)  $\text{Cu}_{0.85}\text{Ni}_{0.15}/\text{C}$ , and (c)  $\text{Cu}_{0.85}\text{Zn}_{0.15}/\text{C}$

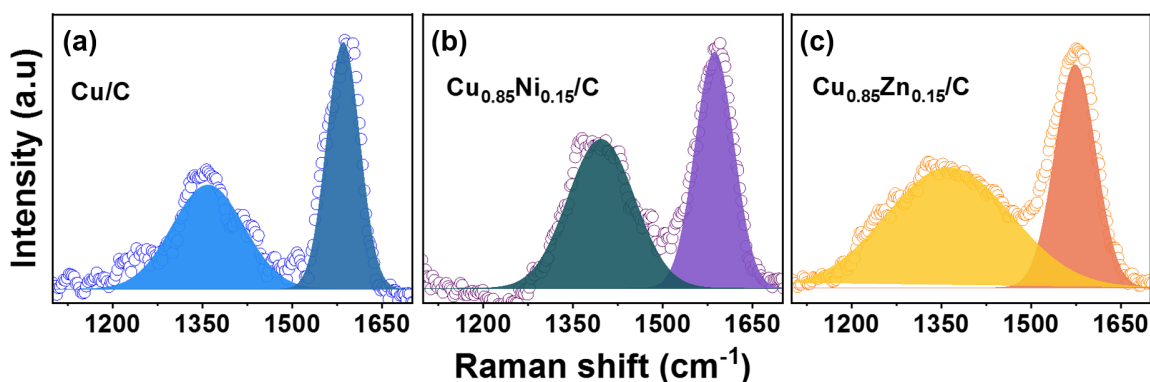


Figure 4.4: Raman Spectra of (a)  $\text{Cu}/\text{C}$ , (b)  $\text{Cu}_{0.85}\text{Ni}_{0.15}/\text{C}$ , and (c)  $\text{Cu}_{0.85}\text{Zn}_{0.15}/\text{C}$

The chemical composition and the elemental oxidation states of the MOF-derived nano-catalysts were studied in detail using XPS. The C 1s core level spectra in Figure 4.5(a) show four deconvoluted peaks. The peak at 284.6 eV can be assigned to the  $sp^2$  hybridized carbon, whereas peaks at 285.3 eV correspond to the  $sp^3$  hybridized carbon. On the other hand, the peaks at 286.5 and 288.7 eV can be assigned to the C-O and O-C=O species, respectively. The Cu 2p core level spectra of the monometallic and the bimetallic nano-alloys are presented in Figure 4.5(b). All the spectra showed two sets of spin-orbit coupled doublet peaks. The metallic copper  $\text{Cu}^0$  peaks were assigned at 932.72 and 952.48 eV, whereas the  $\text{Cu}^{2+}$  were assigned at 934.55 and 954.72 eV, respectively [152]. The major occurrence of zero-valent Cu was observed in all three nano-catalysts, and the surface relative composition of metallic  $\text{Cu}^0$  over  $\text{Cu}/\text{C}$ ,  $\text{Cu}_{0.85}\text{Ni}_{0.15}/\text{C}$  and  $\text{Cu}_{0.85}\text{Zn}_{0.15}/\text{C}$  were found to be 74.3, 77.7 and 79.1%. The presence of another metal apparently helped Cu to be in its metallic state. The shake-up satellite peak at 944.5 eV

confirmed the presence of bivalent Cu [153]. The bivalent Cu must be in an amorphous state as no crystalline Cu<sup>0</sup> were observed in the earlier diffraction experiments. Figure 4.5(c) shows the Ni 2*p* core level spectra of Cu<sub>0.85</sub>Ni<sub>0.15</sub>/C, whereas Figure 4.5(d) shows the Zn 2*p* core level spectra from Cu<sub>0.85</sub>Zn<sub>0.15</sub>/C. Whereas Ni was found to be present in almost equally bivalent and zero-valent states, Zn was predominantly in its metallic state [137].

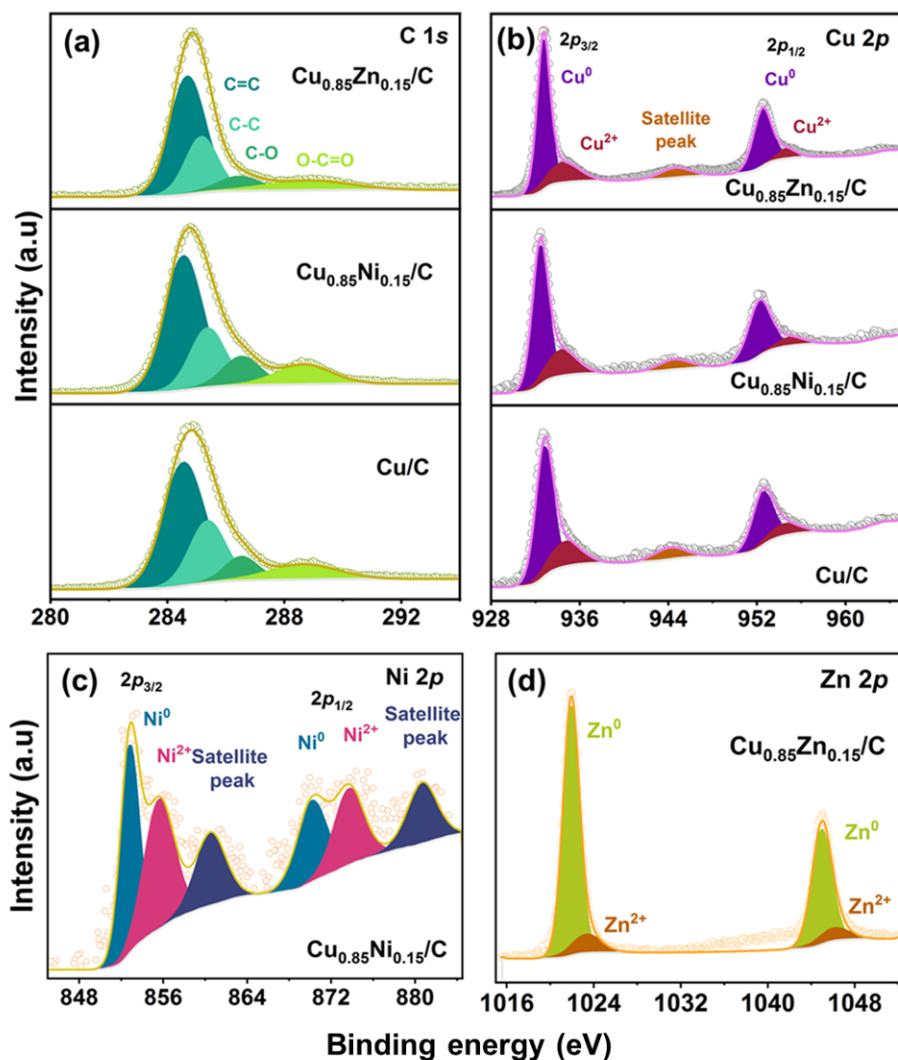


Figure 4.5: Core level XPS data of (a) C 1*s*, (b) Cu 2*p*, (c) Ni 2*p*, and (d) Zn 2*p* of Cu/C, Cu<sub>0.85</sub>Ni<sub>0.15</sub>/C, and Cu<sub>0.85</sub>Zn<sub>0.15</sub>/C

The electrochemically active surface area (ECSA) measured using the Cottrell equation, formulated as

$$i = \frac{nFAC_0\sqrt{D}}{\sqrt{\pi t}} \quad (4.9)$$

where *i* is the current (A), *n* is the number of electrons in the reduction or oxidation reaction of the analyte, *C*<sub>0</sub> is the initial concentration of the nitrate, *D* is the diffusion coefficient of



the nitrate ions ( $\text{cm}^2 \text{s}^{-1}$ ). Using equation 4.9, ECSA was found comparable over the three nano-catalysts, and the values were 1.18, 2.04, and 1.81  $\text{cm}^2$  for Cu/C,  $\text{Cu}_{0.85}\text{Ni}_{0.15}/\text{C}$  and  $\text{Cu}_{0.85}\text{Zn}_{0.15}/\text{C}$ , respectively (Figure 4.6(a)). The BET surface area analysis of the MOFs and the MOF derived catalysts are shown in Figure 4.6(b) and (c). From the surface area analysis data, the MOF-derived catalysts possessed a high surface area (Figure 4.6(c) and Table 4.1). Cu/C showed the highest surface area of 144.8  $\text{m}^2 \text{g}^{-1}$ , whereas  $\text{Cu}_{0.85}\text{Ni}_{0.15}/\text{C}$  and  $\text{Cu}_{0.85}\text{Zn}_{0.15}/\text{C}$  demonstrated a marginally lower value of 122.4 and 111.3  $\text{m}^2 \text{g}^{-1}$ , respectively.

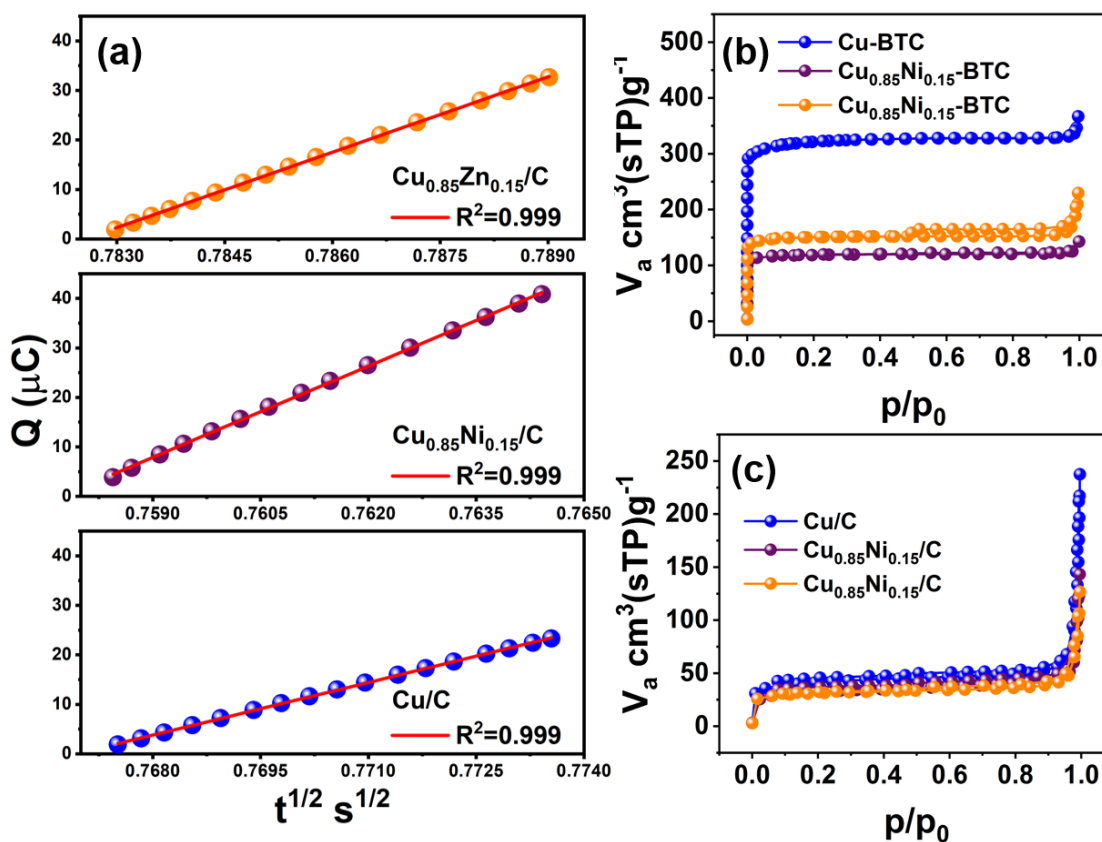


Figure 4.6: (a) ECSA of MOF derived nano-catalysts, and BET adsorption-desorption plot of (b) MOFs and (c) MOF derived nano-catalysts Cu/C,  $\text{Cu}_{0.85}\text{Ni}_{0.15}/\text{C}$ , and  $\text{Cu}_{0.85}\text{Zn}_{0.15}/\text{C}$

Table 4.1: BET surface area of MOFs and MOF-derived nano-catalysts

Electrocatalyst	BET Surface Area ( $\text{m}^2 \text{g}^{-1}$ )
Cu-BTC	1157.5
$\text{Cu}_{0.85}\text{Ni}_{0.15}$ -BTC	443.21
$\text{Cu}_{0.85}\text{Zn}_{0.15}$ -BTC	543.75
Cu/C	144.8
$\text{Cu}_{0.85}\text{Ni}_{0.15}/\text{C}$	122.37
$\text{Cu}_{0.85}\text{Zn}_{0.15}/\text{C}$	111.25

### 4.3.2 NO<sub>x</sub>RR

The electrocatalytic reduction of nitrate in aqueous medium was studied over the MOF-derived monometallic and the bimetallic nano-alloy catalysts. The LSV traces in the absence and in the presence of nitrate within the potential window of 0.5 to -1.5 V (vs. RHE) at a fixed scan rate of 50 mV s<sup>-1</sup> are shown in Figure 4.7(a)-(c). For comparison, the LSV traces of Ni/C and Zn/C are also plotted in Figure 4.7(d) and (e). With the potential continuing negatively, ubiquitously all three nano-catalysts show a steady increase in current density in the absence of nitrate. The sudden increase in the current density at higher negative potentials could be due to the HER. The enhanced cathodic current density in the presence of nitrate indicates the catalytic efficacy of the nanomaterials towards NO<sub>x</sub>RR. The onset potentials were recorded marginally different

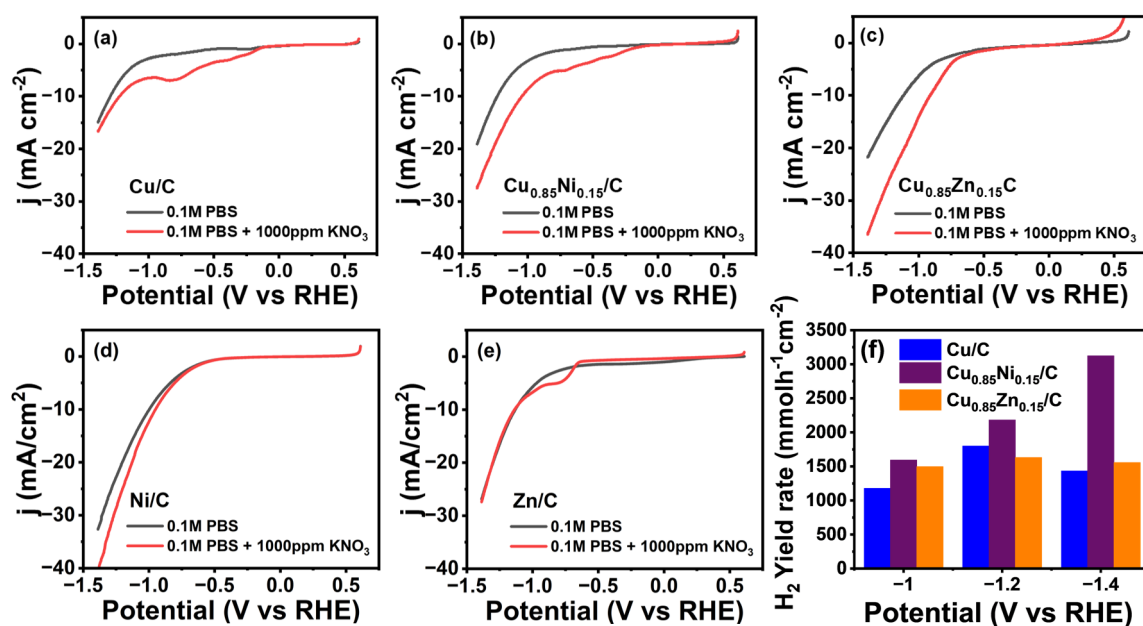


Figure 4.7: (a) LSV curves of electrocatalysts with and without nitrate ions over (a) Cu/C, (b) Cu<sub>0.85</sub>Ni<sub>0.15</sub>/C, (c) Cu<sub>0.85</sub>Zn<sub>0.15</sub>/C, (d) Ni/C, (e) Zn/C, and (f) Yield of H<sub>2</sub> over the Cu/C, Cu<sub>0.85</sub>Ni<sub>0.15</sub>/C and Cu<sub>0.85</sub>Zn<sub>0.15</sub>/C

over the three catalysts as can be seen from Figure 4.7(a)-(c). In fact, the onset potentials were at the slightly lower cathodic potential for pristine Cu/C and Cu<sub>0.85</sub>Ni<sub>0.15</sub>/C compared to Cu<sub>0.85</sub>Zn<sub>0.15</sub>/C, indicating the critical role of monometallic and the bimetallic nano-alloy catalysts in the activation of nitrate ions. The first minor peak at about -0.4 V could be due to the reduction of NO<sub>3</sub><sup>-</sup> to NO<sub>2</sub><sup>-</sup>, whereas the second major peak around -0.75 V was assigned to the reduction of NO<sub>2</sub><sup>-</sup> to NH<sub>3</sub> [154, 155]. Among the materials, the current density of Cu<sub>0.85</sub>Zn<sub>0.15</sub>/C



was found to be higher than the other two catalysts (particularly at higher potential) implying a higher catalytic  $\text{NO}_x\text{RR}$  efficacy over the nano-alloy. But as discussed, higher current density in LSV plot may not differentiate well between HER and  $\text{NO}_x\text{RR}$ . Therefore, controlled potential experiments were performed with the electrolyte in the presence of nitrate for 2 h over the three catalysts, and the evolved  $\text{H}_2$  was measured using the GC. The yield of  $\text{H}_2$  over the materials is plotted against applied cathodic potentials in Figure 4.7(f). Apparently,  $\text{Cu}_{0.85}\text{Ni}_{0.15}/\text{C}$  showed a higher yield of  $\text{H}_2$  than the  $\text{Cu}_{0.85}\text{Zn}_{0.15}/\text{C}$ . The data apparently unveils that the current density over  $\text{Cu}_{0.85}\text{Ni}_{0.15}/\text{C}$  is mostly responsible for high HER, whereas the lower  $\text{H}_2$  evolution in spite of high cathodic current density over  $\text{Cu}_{0.85}\text{Zn}_{0.15}/\text{C}$  indicate higher  $\text{NO}_x\text{RR}$  activity over the Zn containing nano-alloy catalyst. Representative chromatograms over  $\text{Cu}_{0.85}\text{Ni}_{0.15}/\text{C}$  in different potentials are provided in Figure 4.8.

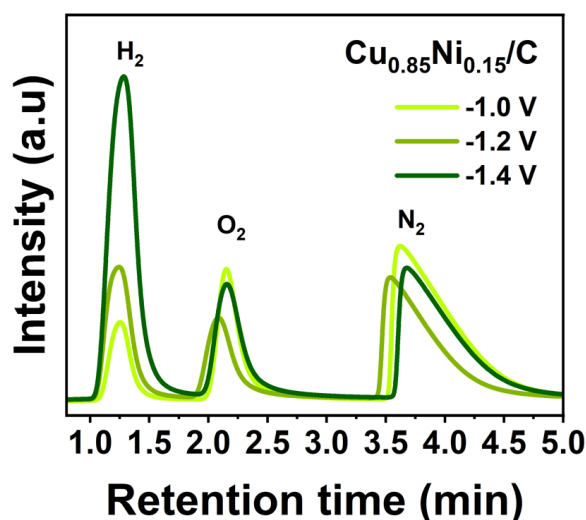


Figure 4.8: Representative GC chromatograms of  $\text{H}_2$  from  $\text{Cu}_{0.85}\text{Ni}_{0.15}/\text{C}$  after 2 h of chronoamperometric study

To corroborate the high  $\text{NO}_x\text{RR}$  activity over  $\text{Cu}_{0.85}\text{Zn}_{0.15}/\text{C}$ , the conversion of  $\text{NO}_3^-$  and the liquid products formed were identified after the 2 h of controlled potential experiments in the presence of nitrate over the three catalysts. Figure 4.9(a) shows representative UV-Vis spectra of nitrate concentration against different potentials. Only two reduction products, ammonia and nitrite were identified and the corresponding absorption spectra are plotted in Figure 4.9(b) and (c). Figure 4.10 shows the percentage conversion of  $\text{NO}_3^-$  against the applied potentials over the MOF-derived nano-alloy catalysts. Figure 4.11(a) shows the yield of  $\text{NH}_3$  against the applied cathodic potentials. Apparently, the yield of  $\text{NH}_3$  steadily increased with the increase in potentials over all the three nano-catalysts, and the highest yield of  $\text{NH}_3$  was found to be over

$\text{Cu}_{0.85}\text{Zn}_{0.15}/\text{C}$  compared to the other two catalysts. Particularly, at -1.2 and -1.4 V (vs. RHE) the yield of  $\text{NH}_3$  over  $\text{Cu}_{0.85}\text{Zn}_{0.15}/\text{C}$  was found to be as high as 1916.3 and 2143.6  $\mu\text{g h}^{-1} \text{cm}^{-2}$ , respectively. As  $\text{NO}_2^-$  was the second product, we also measured the yield of formation of  $\text{NO}_2^-$  over the catalysts at the same cathodic potentials, and the results are plotted in Figure 4.11(b). The overall yield of  $\text{NO}_2^-$  over the three catalysts was found to be significantly lower than that of  $\text{NH}_3$ . Interestingly, while pristine  $\text{Cu}/\text{C}$  showed a monotonic increase of yield of  $\text{NO}_2^-$  with the

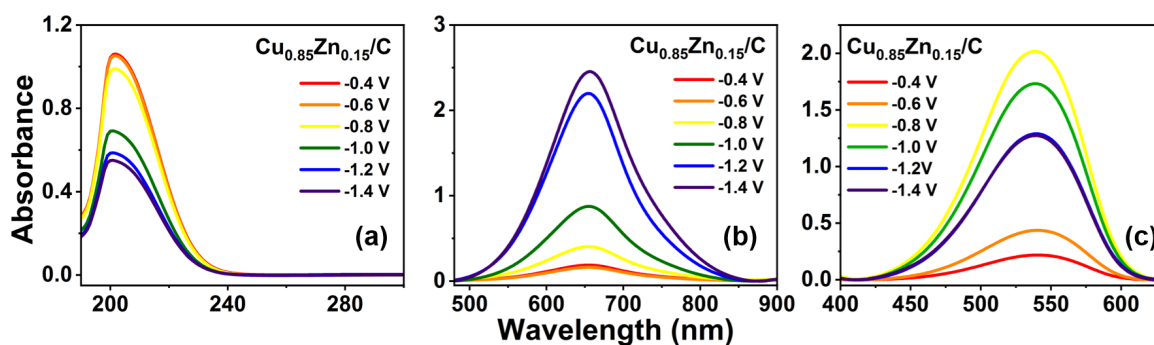


Figure 4.9: Representative UV-Vis absorption spectra of (a) nitrate concentration, (a) ammonia formed, and (b) nitrite formed against different potentials over  $\text{Cu}_{0.85}\text{Zn}_{0.15}/\text{C}$

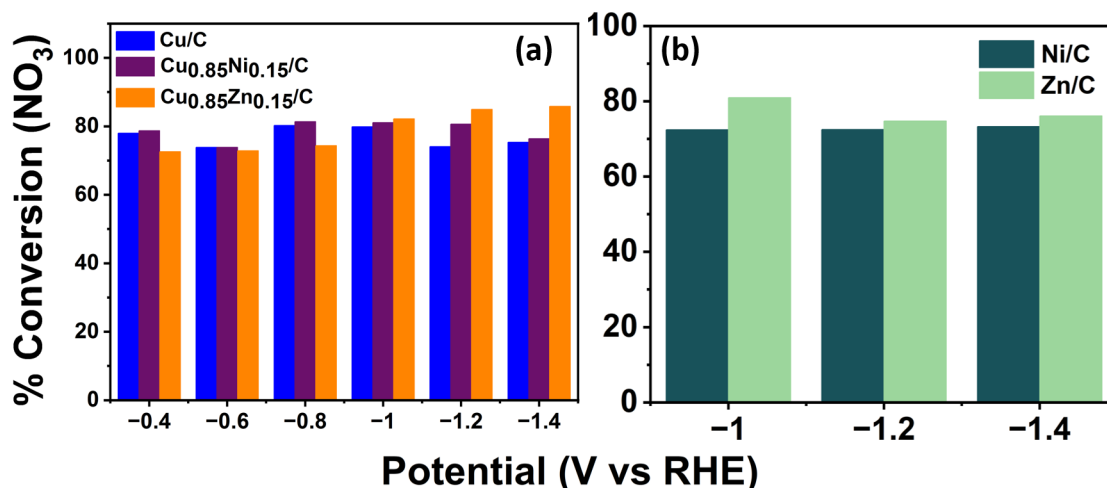


Figure 4.10: The degrees of conversion of  $\text{NO}_3^-$  against the applied potentials over (a) over  $\text{Cu}/\text{C}$ ,  $\text{Cu}_{0.85}\text{Ni}_{0.15}/\text{C}$ , and  $\text{Cu}_{0.85}\text{Zn}_{0.15}/\text{C}$ , and (b)  $\text{Ni}/\text{C}$  and  $\text{Zn}/\text{C}$

increase in cathodic potentials, the bimetallic nano-alloy  $\text{Cu}_{0.85}\text{Ni}_{0.15}/\text{C}$  exhibited the exact opposite trend. On the other hand,  $\text{Cu}_{0.85}\text{Zn}_{0.15}/\text{C}$  demonstrated a volcanic-type plot of yield in  $\text{NO}_2^-$  against the negatively increased potentials. The selectivity of  $\text{NH}_3$  was calculated, and the results in Figure 4.11(c) show the superiority of the nano-alloy  $\text{Cu}_{0.85}\text{Zn}_{0.15}/\text{C}$  over the other

two catalysts. As control experiments, the yield of  $\text{NH}_3$  and  $\text{NO}_2^-$  as well as the selectivity of  $\text{NH}_3$  over Ni/C and Zn/C were measured and plotted in Figure 4.12. It's apparent from the results that the pristine monometallic catalysts demonstrated very poor catalytic activity.

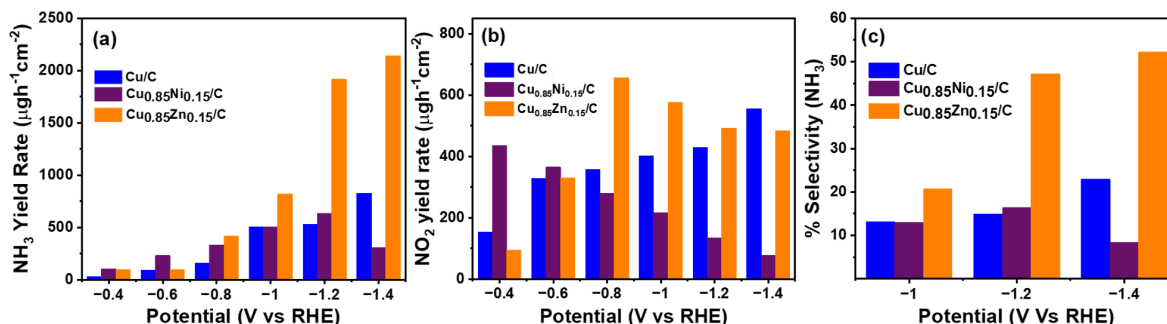


Figure 4.11: (a) Yield of  $\text{NH}_3$ , (b) Yield of  $\text{NO}_2^-$ , and (c) Selectivity of  $\text{NH}_3$  over Cu/C,  $\text{Cu}_{0.85}\text{Ni}_{0.15}/\text{C}$ , and  $\text{Cu}_{0.85}\text{Zn}_{0.15}/\text{C}$

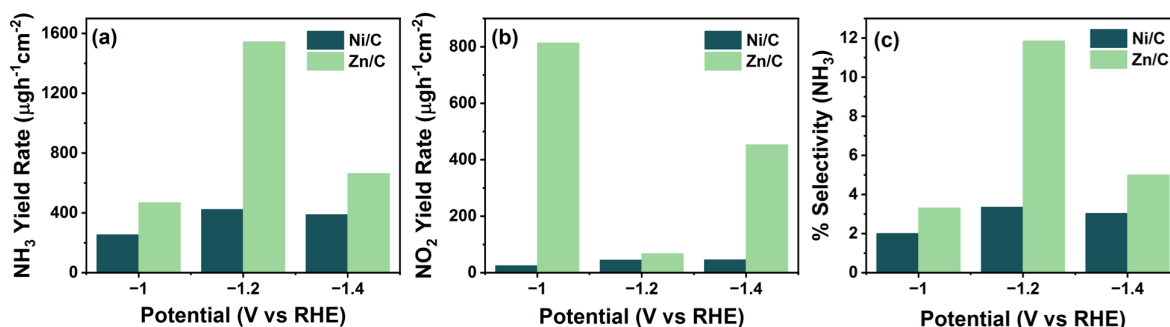


Figure 4.12: (a) Yield of  $\text{NH}_3$ , (b) Yield of  $\text{NO}_2^-$ , and (c) Selectivity of  $\text{NH}_3$  over Ni/C and Zn/C

Further, the  $\text{EE}(\%)$  and the  $\text{FE}(\%)$  of the two  $\text{NO}_x\text{RR}$  liquid products and  $\text{H}_2$  from HER were evaluated. Figure 4.13 shows the percentage of  $\text{EE}$  of formation of the desired product. Figure 4.14(a) shows that the  $\text{FE}(\%)$  of  $\text{NH}_3$  gradually decreases over pristine Cu/C nano-catalyst with an increase in cathodic potential. A similar trend of declining  $\text{FE}(\%)$  of  $\text{NH}_3$  with higher cathodic potentials was also observed over  $\text{Cu}_{0.85}\text{Ni}_{0.15}/\text{C}$  nano-alloy (Figure 4.14(b)). However, interestingly the  $\text{FE}(\%)$  of  $\text{H}_2$  steadily increased with an increase in cathodic potential indicating a significant HER over the  $\text{Cu}_{0.85}\text{Ni}_{0.15}/\text{C}$  catalyst. It should be noted that a minor contribution of  $\text{FE}(\%)$  of  $\text{NO}_2^-$  was observed at lower cathodic potential over the pristine Cu/C catalyst, however,  $\text{FE}(\%)$  of  $\text{NO}_2^-$  was obscured at higher potentials. This suggests that  $\text{NO}_2^-$  could be an intermediate product and can be further reduced to  $\text{NH}_3$  under more negative potentials [156]. The total  $\text{FE}(\%)$  of  $\text{NH}_3$ ,  $\text{NO}_2^-$  and  $\text{H}_2$  at around 80(%) indicate formation of  $\text{N}_2$  and/or

$\text{N}_2\text{H}_4$  as reduction products from the nitrate over pristine Cu/C and  $\text{Cu}_{0.85}\text{Ni}_{0.15}/\text{C}$  catalysts. The formation of gaseous  $\text{N}_2$  was not evaluated. However, the possible production of  $\text{N}_2\text{H}_4$  was evaluated by the Watt-Chrisp method, and no  $\text{N}_2\text{H}_4$  was detected over any sample. Figure 4.14(c) shows the highest FE(%) of  $\text{NH}_3$  over  $\text{Cu}_{0.85}\text{Zn}_{0.15}/\text{C}$  among the three catalysts. The highest

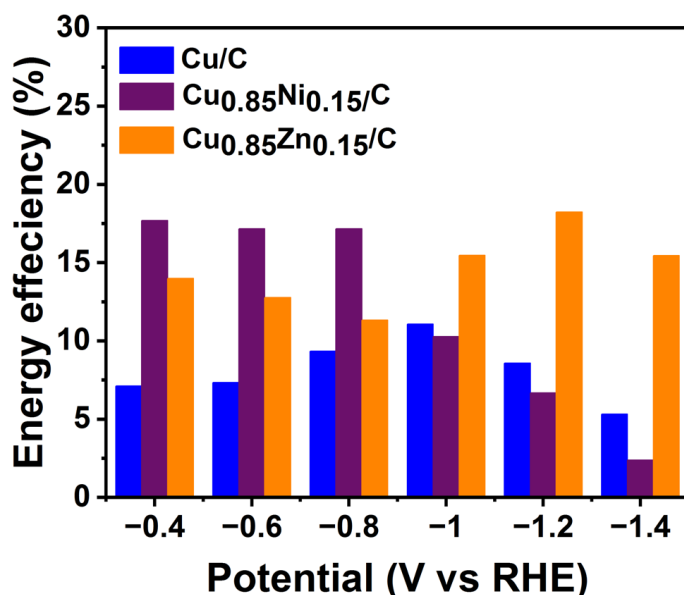


Figure 4.13: The percentage of energy efficiency of formation of  $\text{NH}_3$  over over Cu/C,  $\text{Cu}_{0.85}\text{Ni}_{0.15}/\text{C}$ , and  $\text{Cu}_{0.85}\text{Zn}_{0.15}/\text{C}$

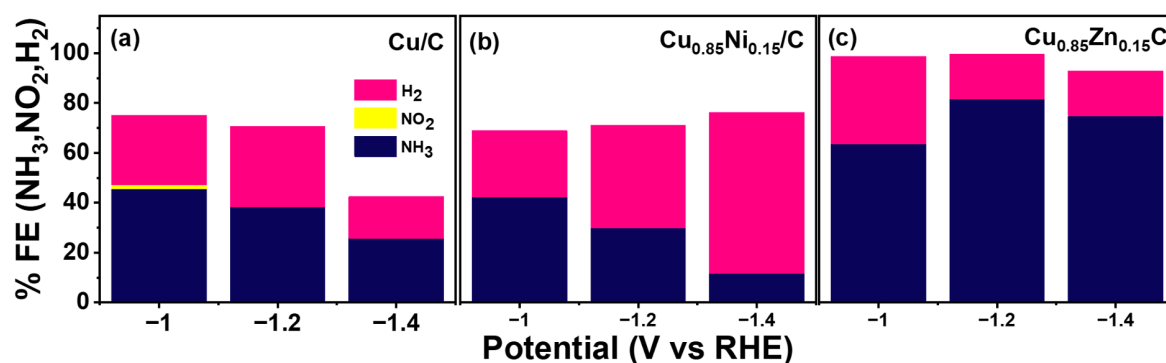


Figure 4.14: FE(%) of  $\text{NH}_3$ ,  $\text{NO}_2$ , and  $\text{H}_2$  over (a) Cu/C, (b)  $\text{Cu}_{0.85}\text{Ni}_{0.15}/\text{C}$ , and (c)  $\text{Cu}_{0.85}\text{Zn}_{0.15}/\text{C}$

FE(%) of  $\text{NH}_3$  around 82% was observed at -1.2 V. A minute FE(%) of  $\text{NO}_2^-$  was observed at lower cathodic potential and was obscured at higher potentials. Interestingly, the FE(%) of  $\text{H}_2$  was significantly low over  $\text{Cu}_{0.85}\text{Zn}_{0.15}/\text{C}$  indicating a low HER. The total FE(%) of  $\text{NH}_3$ ,  $\text{NO}_2^-$  and  $\text{H}_2$  over  $\text{Cu}_{0.85}\text{Zn}_{0.15}/\text{C}$  also indicated a very insignificant formation of gaseous  $\text{N}_2$ . The high

current density from LSV traces, the high yield of  $\text{NH}_3$  leading to higher selectivity, and the high FE(%) of  $\text{NH}_3$  compared to that of  $\text{H}_2$  conclusively established the superior electro-catalytic performance of  $\text{Cu}_{0.85}\text{Zn}_{0.15}/\text{C}$  towards reducing the nitrate to  $\text{NH}_3$ . It should be noted that the FE(%) of the desired products over monometallic  $\text{Ni}/\text{C}$  and  $\text{Zn}/\text{C}$  were insignificant (Figure 4.15).

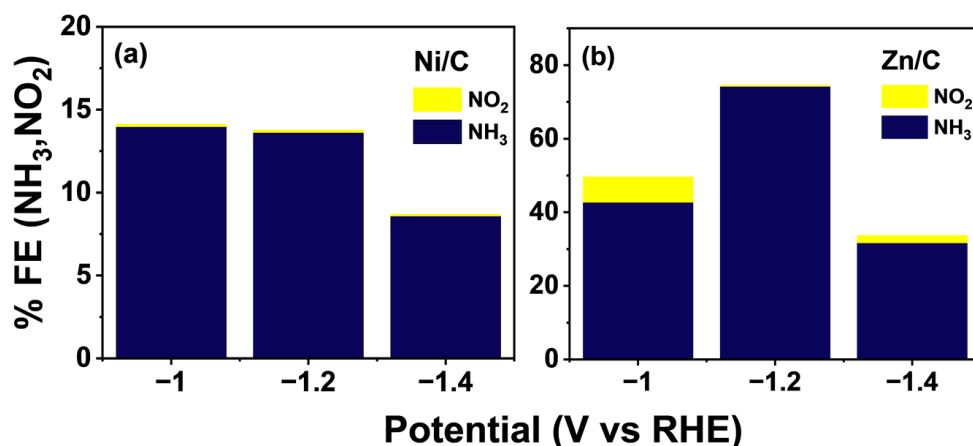


Figure 4.15: FE(%) of  $\text{NH}_3$ ,  $\text{NO}_2$  and  $\text{H}_2$  over (a)  $\text{Ni}/\text{C}$  and (b)  $\text{Zn}/\text{C}$

Previous research on electrocatalytic nitrate reduction, using *in-situ* electrochemical Raman spectra and XRD patterns, showed that the *in-situ* electrochemical reconstruction of the  $\text{Cu}/\text{Cu}_2\text{O}$  interface from pristine  $\text{CuO}$  aided in the electrocatalytic nitrate reduction [136]. However, our study did not reveal any crystalline  $\text{Cu}_2\text{O}$  in the exhausted catalyst. To have further insight into the reaction kinetics, charge transfer resistance, Tafel slope, rate constants, and activation energy were inspected over the three nano-catalysts. From the Nyquist plot in Figure 4.16(a), it

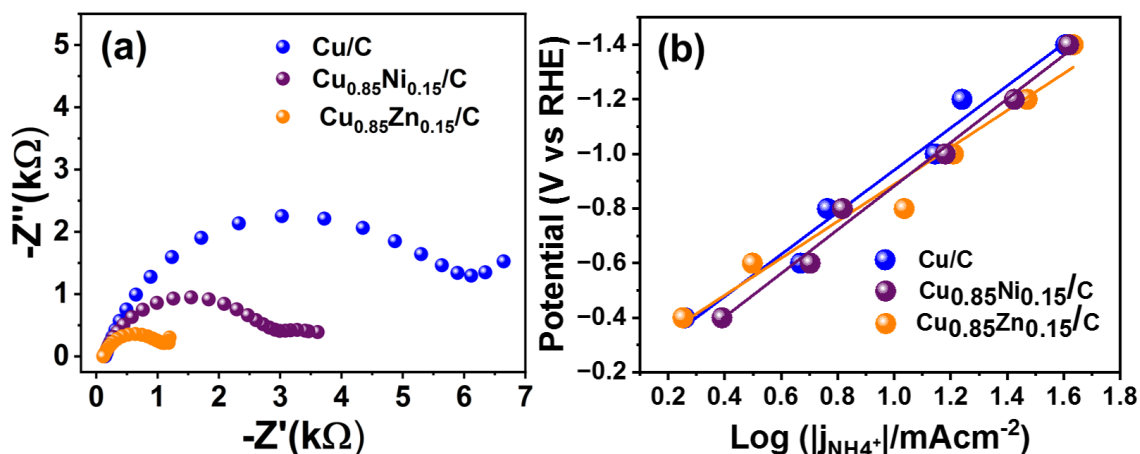


Figure 4.16: (a) Impedance spectra and (b) Tafel plots over  $\text{Cu}/\text{C}$ ,  $\text{Cu}_{0.85}\text{Ni}_{0.15}/\text{C}$ , and  $\text{Cu}_{0.85}\text{Zn}_{0.15}/\text{C}$

is apparent that though the three nanomaterials showed similar patterns of arcs, Cu<sub>0.85</sub>Zn<sub>0.15</sub>/C displayed the smallest semi-circle followed by Cu<sub>0.85</sub>Ni<sub>0.15</sub>/C and Cu/C. It can be concluded that Cu<sub>0.85</sub>Zn<sub>0.15</sub>/C possessed the lowest charge transfer resistance and consequently high electrical conductivity to exhibit better NO<sub>x</sub>RR catalytic activity than the other two nanomaterials. The Tafel slopes for the three catalysts Cu/C, Cu<sub>0.85</sub>Ni<sub>0.15</sub>/C and Cu<sub>0.85</sub>Zn<sub>0.15</sub>/C were found to be 79.86, 77.15 and 67.64 mV dec<sup>-1</sup>, respectively (Figure 4.16(b)). The obtained Tafel slopes being close to the theoretical value of 59 mV dec<sup>-1</sup>, indicate that the rate-determining step was not the initial electron transfer process, but the succeeding chemical process. The smaller Tafel slope as well as the smaller charge transfer resistance suggested the faster NO<sub>x</sub>RR reaction kinetics of Cu<sub>0.85</sub>Zn<sub>0.15</sub>/C towards high yield rate and FE(%) of NH<sub>3</sub>.

To reveal the details of the reaction process of NO<sub>x</sub>RR over the nano-catalysts, LSV curves were recorded at different scan rates to probe the electron transfer of the specific process (Figure 4.17). A linear relationship was observed between the square root of the scan rate and the peak current (Figure 4.18(a)) following the Randles-Sevick equation:

$$I_p = (2.99 \times 10^5) n(\alpha n)^{1/2} A C_o D_o^{1/2} \vartheta^{1/2} \quad (4.10)$$

In the equation  $I_p$  stands for the peak current,  $n$  is the number of electrons involved in the reduction process,  $\alpha$  is the charge transfer coefficient,  $A$  is the area (cm<sup>2</sup>) of the electrode,  $C_o$  is the bulk concentration of nitrate (mol cc<sup>-1</sup>),  $D_o$  is the diffusion coefficient (cm<sup>2</sup> s<sup>-1</sup>) and  $\vartheta$  stands for scan rate (V s<sup>-1</sup>). The linear relation indicates that the NO<sub>x</sub>RR over the three nano-catalysts is a diffusion-controlled process rather than a surface-controlled phenomenon [157]. The diffusion coefficient ( $D_o$ ) was found to be similar over Cu/C ( $8.4 \times 10^{-9}$  cm<sup>2</sup> s<sup>-1</sup>) and Cu<sub>0.85</sub>Ni<sub>0.15</sub>/C ( $4.4 \times 10^{-9}$  cm<sup>2</sup> s<sup>-1</sup>), whereas the value was found to be orders of magnitude higher with Cu<sub>0.85</sub>Zn<sub>0.15</sub>/C ( $8.4 \times 10^{-7}$  cm<sup>2</sup>s<sup>-1</sup>). Additionally, using the diffusion coefficients we calculated the rate constant ( $k_o$ ) of the NO<sub>x</sub>RR over the materials according to the following equation [158]:

$$E_p = E^f - \frac{RT}{\alpha n F} \left[ 0.784 + 2.303 \log \left( \frac{D_o^{1/2}}{k_o} \right) + 2.303 \log \left( \frac{\alpha n F \vartheta}{RT} \right)^{1/2} \right] \quad (4.11)$$

where,  $E_p$  is the peak potential (V),  $E^f$  is the formal potential (V),  $\alpha$  is the charge transfer coefficient,  $R$  is the universal gas constant (Jmol<sup>-1</sup>K<sup>-1</sup>) and  $T$  is temperature (K). From the plot of  $E_p$  vs. log scan rate (Figure 4.18(b)), the rate constants ( $k_o$ ) of the pseudo first-order kinetics of NO<sub>x</sub>RR over three catalysts were found out, and the values were  $1.02 \times 10^{-3}$  s<sup>-1</sup> over

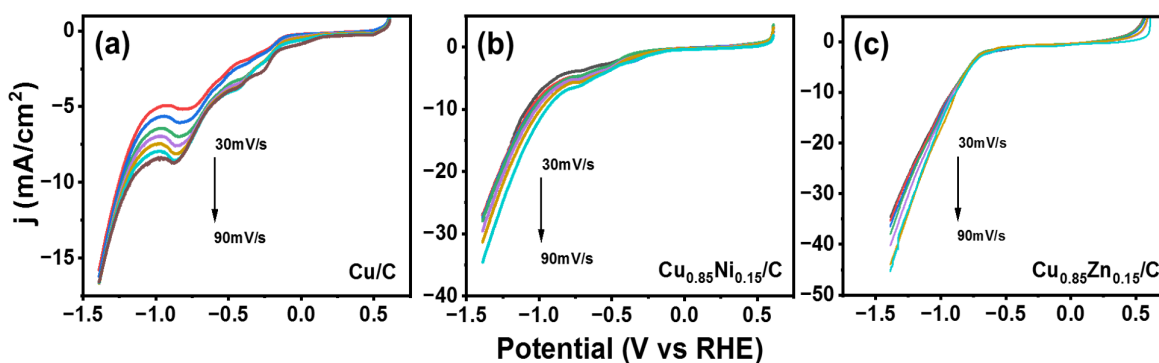


Figure 4.17: LSV curves at different scan rates over (a) Cu/C (b) Cu<sub>0.85</sub>Ni<sub>0.15</sub>/C and (c) Cu<sub>0.85</sub>Zn<sub>0.15</sub>/C

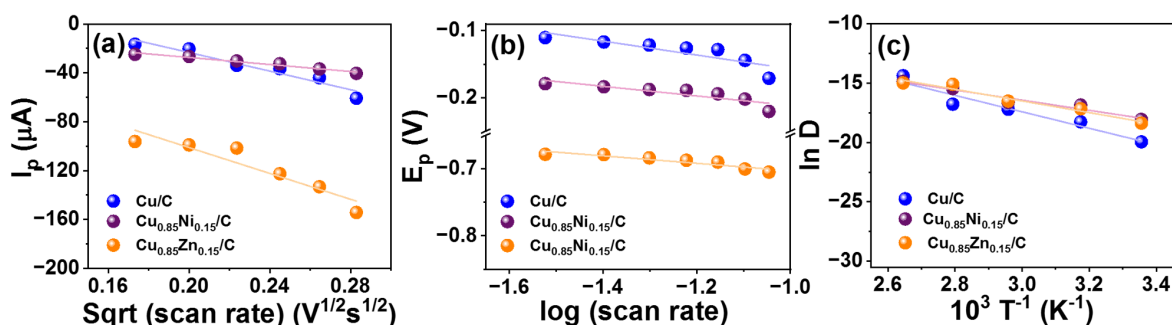


Figure 4.18: (a) Plot of peak current with the square root of scan rate following the Randles-Sevcik equation, (b) plot of peak potential ( $E_p$ ) with the log of scan rate, and (c) Arrhenius plotting of the three MOF-derived nano catalysts

Cu/C,  $2.16 \times 10^{-3} \text{ s}^{-1}$  over Cu<sub>0.85</sub>Ni<sub>0.15</sub>/C, and  $2.83 \times 10^{-3} \text{ s}^{-1}$  over Cu<sub>0.85</sub>Zn<sub>0.15</sub>/C. Apparently the Cu<sub>0.85</sub>Zn<sub>0.15</sub>/C nano-alloy catalysts with its higher NO<sub>x</sub>RR rate constant and consequently faster kinetics outperformed the other two materials. A plot of ln D vs. 1000/T as obtained in Figure 4.18(c) demonstrates a good correlation of the data to the Arrhenius relationship. Further, the apparent activation energy of the NO<sub>x</sub>RR over the MOF-derived catalysts was also evaluated. With increasing temperature, the cathodic peak potential of the reduction reaction gradually increased (Figure 4.19). The temperature dependence of the diffusion coefficient can be examined with the Arrhenius equation:

$$D = D_0 \exp(-E_D/RT) \quad (4.12)$$

where,  $E_D$  is the diffusional activation energy of the electroactive species.

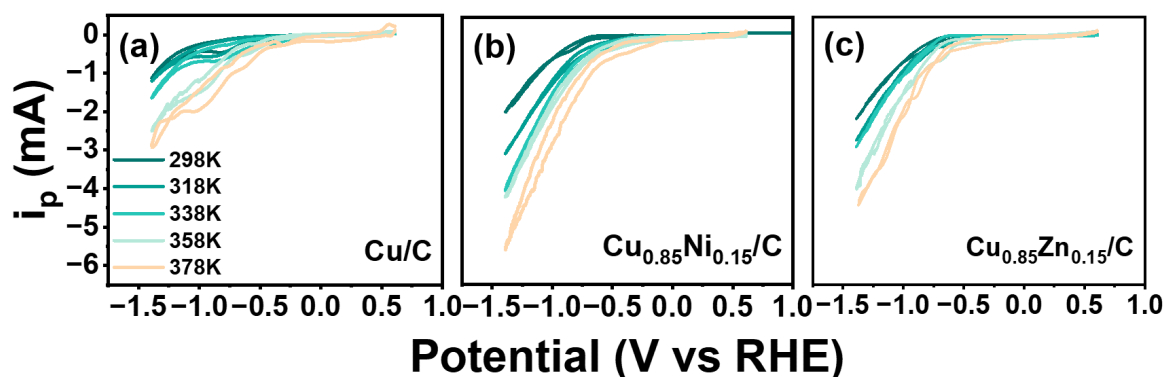


Figure 4.19: Plot of the cathodic current against applied potential at different temperatures over (a) Cu/C, (b) Cu<sub>0.85</sub>Ni<sub>0.15</sub>/C, and (c) Cu<sub>0.85</sub>Zn<sub>0.15</sub>/C

To rationalize the superiority of the catalyst Cu<sub>0.85</sub>Zn<sub>0.15</sub>/C in NO<sub>x</sub>RR in terms of the rate of the reaction as well as selectivity and FE(%) of NH<sub>3</sub>, we have studied the electronic states and the *d*-bands in detail with the help of DFT based the first principle calculations. The position of the *d*-band with respect to the Fermi level is important because it indicates the availability of electrons in the atom. Thus, the position of the *d*-band is strongly correlated to the binding energy of intermediates, and thereby often used as a metric for catalytic activity [159, 160]. As the XRD data show (111) plane as the most exposed facet of the as-synthesized face-centered cubic nanomaterials, in DFT calculations the same plane was considered as the effective reactive surface. The energy minimized relaxed (111) surfaces of Cu/C, Cu<sub>0.85</sub>Ni<sub>0.15</sub>/C and Cu<sub>0.85</sub>Zn<sub>0.15</sub>/C are depicted in Figure 4.20. Next, the electronic properties including the atomic orbital projected density of states (PDOS) were calculated using the GGA-PBE method, and the PDOS profiles are projected in Figure 4.21(a) with the emphasis on *d*-orbitals of the host and dopant atoms. The comparative *d*-orbital profiles indicate that the introduction of Ni

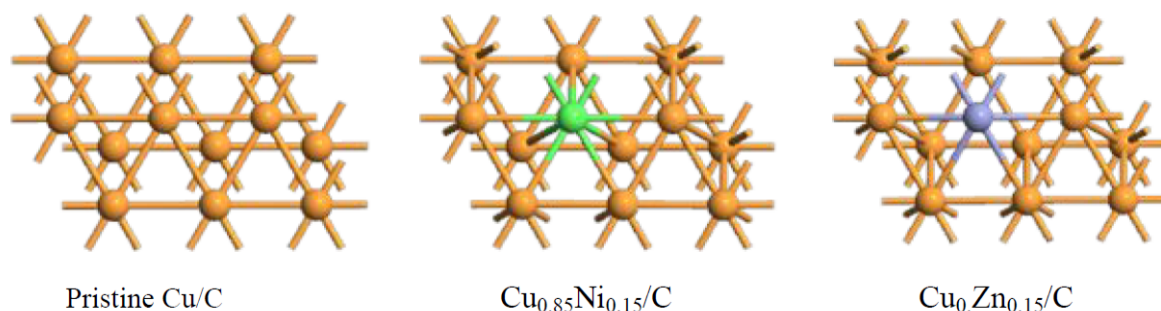


Figure 4.20: (a) Atomic orbital (*d*-orbital) projected density of states profiles of pristine Cu/C, Cu<sub>0.85</sub>Ni<sub>0.15</sub>/C, and Cu<sub>0.85</sub>Zn<sub>0.15</sub>/C (b) adsorption energies for different molecular species adsorptions on pristine Cu/C, Cu<sub>0.85</sub>Ni<sub>0.15</sub>/C and Cu<sub>0.85</sub>Zn<sub>0.15</sub>/C surfaces, with the adsorption schematics



doping increases the Cu  $d$ -orbital contribution near the Fermi level, whereas an exactly opposite trend can be observed after introducing Zn. Moreover, relatively larger and marginal  $d$ -orbital contributions can also be observed for Zn and Ni doping. These findings suggest that Ni doping in  $\text{Cu}_{0.85}\text{Ni}_{0.15}/\text{C}$  results in significantly larger overall  $d$ -orbital contributions near Fermi level compared to Zn doping in  $\text{Cu}_{0.85}\text{Zn}_{0.15}/\text{C}$ . The presence of such larger  $d$ -orbital contributions is highly suitable for strong atomic orbital overlap between the adsorbed species and adsorbent surfaces leading to stronger molecular adsorption. To verify this, the comparative adsorption energies of different intermediate species following the most probable reaction path have been considered for all three surfaces and are depicted in Figure 4.21(b). As nitrite was experimentally observed to as one of the intermediates, the  $e^-/\text{H}^+$  assisted reduction path was considered to be  $\text{NO}_3 \rightarrow \text{NO}_2 \rightarrow \text{NO} \rightarrow \text{NH}_2\text{OH} \rightarrow \text{NH}_3$ . Clearly, the  $\text{Cu}_{0.85}\text{Zn}_{0.15}/\text{C}$  has the lowest adsorption energy throughout the reaction pathways, which is in excellent agreement with the PDOS analysis. However, since all the intermediate species are rather strongly adsorbed in the metal surfaces (the lowest adsorption energy has a magnitude higher than 4.5 eV), the  $\text{Cu}_{0.85}\text{Zn}_{0.15}/\text{C}$  is expected to be the most favorable metal surface for electrochemical activities. This is also in good agreement with the experimental observations of this work.

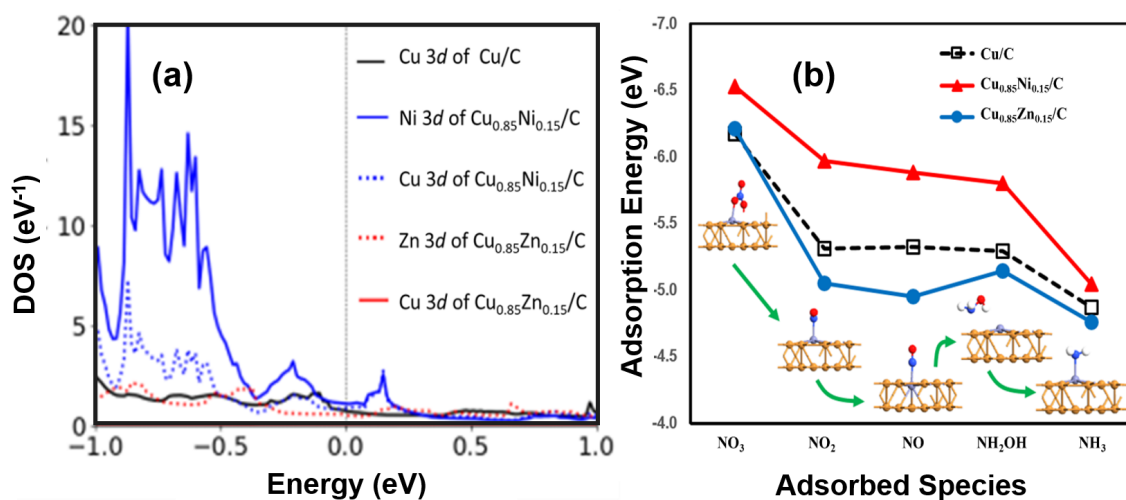


Figure 4.21: Energy minimized relaxed (111) surfaces of  $\text{Cu}/\text{C}$ ,  $\text{Cu}_{0.85}\text{Ni}_{0.15}/\text{C}$ , and  $\text{Cu}_{0.85}\text{Zn}_{0.15}/\text{C}$

## 4.4 Conclusion

The pristine Cu/C and the nano-alloys of Cu<sub>0.85</sub>Ni<sub>0.15</sub>/C and Cu<sub>0.85</sub>Zn<sub>0.15</sub>/C synthesized from the corresponding monometallic and bimetallic MOFs crystallized in a phase pure face-centered cubic lattice with a very high dispersion of the active sites over the carbonaceous supports. The carbonaceous support of Cu<sub>0.85</sub>Zn<sub>0.15</sub>/C possessed the highest concentration of defect carbon among the three catalysts. The XPS analyses revealed that the support carbon of all the three nano-catalysts contained the *sp*<sup>2</sup> and *sp*<sup>3</sup> hybridized carbon, along with C-O and O-C=O species. The active sites of metals were majorly found in their zero valent oxidation state. The detailed catalytic studies over the nano-catalysts unveiled that the Cu<sub>0.85</sub>Zn<sub>0.15</sub>/C possessed a superior NO<sub>x</sub>RR activity owing to the higher FE(%), higher yield, and higher selectivity of NH<sub>3</sub>. The higher NO<sub>x</sub>RR rate constant also indicated a faster kinetics over Cu<sub>0.85</sub>Zn<sub>0.15</sub>/C compared to the other two nanomaterials. On the other hand, Cu<sub>0.85</sub>Ni<sub>0.15</sub>/C exhibited an efficient unselective HER over the material. The first principle calculation revealed that the alteration in *d*-band in Cu<sub>0.85</sub>Zn<sub>0.15</sub>/C near the Fermi level played a major role in influencing the interaction of nitrate and other reaction intermediates with the optimized surface of the nano-alloy catalyst and thereby improved the catalytic efficacy.

## Chapter 5

# Understanding the Catalytic Materials in NO<sub>x</sub> Removal: A Summary and Conclusion

### 5.1 Insight into the Catalytic Materials

Catalysis plays a pivotal role in modern science and technology, enabling the development of more competent and sustainable processes across various fields. In recent research efforts, scientists have focused on enhancing catalytic materials to address critical challenges such as environmental pollution and energy conversion. This summary encapsulates a comprehensive exploration of catalytic materials and their applications in NO<sub>x</sub> removal in our laboratory, showcasing the versatile nature of catalyst design and modification. This research encompasses a range of catalytic materials for deNO<sub>x</sub>ification and converting it into environmentally friendly and useful products as well the insights into their catalytic mechanisms and efficiency improvements. Investigating the catalytic mechanisms involved in NO<sub>x</sub> reduction is essential for optimizing catalyst performance. Understanding the surface reactions, reaction kinetics, and the role of active sites on the catalyst can lead to the development of more efficient and selective catalysts. In the first study, we harnessed the potential of metal-organic frameworks with high surface area and porosity. This study delved into the catalytic reduction of NO<sub>x</sub> using metallic Pt dispersed on a ZIF-8 MOF whereby the high surface area and the porosity of the MOF materials played a pivotal role in the NO<sub>x</sub> conversion. These properties of ZIF-8 were instrumental for

NO adsorption and the dispersed Pt effectively converted NO at a low temperature. The ZIF-8 was prepared using the direct wet chemistry method and the Pt was dispersed by impregnation method. As against the traditional Pt/Zeolite, the Pt/ZIF showed exceptional conversion at a lower temperature than the previous. All these catalytic performances can be devoted to the material properties of Pt/ZIF-8. Moving to the second investigation, the focus shifted to understanding the plausible mechanism using the solid solutions of Ce<sub>1-x</sub>Ni<sub>x</sub>O<sub>2-δ</sub> as catalysts for NO reduction. Also, to explore a better non-noble catalyst, we chose Ce and the transition metal Ni to synthesize the catalyst. The different synthetic routes were implemented to prepare the catalysts to study the unveiled role of oxygen vacancies and surface hydroxyl species in catalysis. The importance of the synthetic procedure and the reducibility of the catalyst were conveyed through this research.

After carefully investigating the material properties and importance of the preparation method for the catalytic material for gaseous NO<sub>x</sub>, we explored materials for the catalytic reduction of aqueous NO<sub>x</sub>. The third study explored electrocatalytic nitrate reduction, from which the concept of waste to wealth was achieved. The electro-catalysts prepared by a two-step process converted pollutant nitrate into valuable ammonia products. Here, the employment of nano-alloys of Cu doped with Ni and Zn to fine-tune the electronic structure and surface interactions, led to enhanced selectivity and yield in nitrate reduction. This innovative approach opens new possibilities for environmentally friendly technologies.

In sum, these three studies underscore the importance of catalysts in addressing one of the global challenges i.e., NO<sub>x</sub> abatement. We have successfully improved NO<sub>x</sub> reduction by carefully engineering the catalyst materials. These findings have implications for environmental remediation, energy conversion, and sustainable chemistry, highlighting the importance of understanding the underlying mechanisms of catalysis and the potential of fine-tuning catalyst properties. Overall, this research contributes valuable insights to the field of catalysis and offers promising avenues for future studies and applications.

## 5.2 Future scope of the work

The work presented in this thesis integrates a noteworthy contribution to the field of ambient and low-temperature NO<sub>x</sub> abatement catalysis. The research has provided a comprehensive understanding of material properties through the manipulation of synthesis procedures and their

relationship with the reaction mechanism. Looking ahead, there are several promising avenues for future research and development. Some potential areas of focus include:

1. Designing catalysts with a wide temperature window, high activity, and resistance to SO<sub>2</sub>, moisture, alkali, and heavy metals.
2. Laboratory-scale research to industrial-scale implementation with considerations of scalability and cost-efficiency.
3. To gain a more comprehensive understanding of the reaction mechanisms and the kinetics with the help of *in-situ* characterization techniques.
4. Engineering of electrocatalysts and electrolytes in concordance with the pH for better selectivity, durability, yield, and suppression of H<sub>2</sub> evolution.

Overall, the results and understanding gained from this thesis open up exciting possibilities for advancing the field of NO<sub>x</sub> abatement catalysis. By addressing the challenges of cost-effectiveness and environmental impact, while optimizing selectivity and scalability, future research can contribute significantly to achieving cleaner and more sustainable air quality.

# Bibliography

- (1) Lasek, J. A.; Lajnert, R. *Applied Sciences* **2022**, *12*, 10429.
- (2) Masera, K.; Hossain, A. K. *Renewable and Sustainable Energy Reviews* **2023**, *178*, 113235.
- (3) Ozgen, S; Cernuschi, S; Caserini, S *Renewable and Sustainable Energy Reviews* **2021**, *135*, 110113.
- (4) Ye, B.; Jeong, B.; Lee, M.-j.; Kim, T. H.; Park, S.-S.; Jung, J.; Lee, S.; Kim, H.-D. *Nano Convergence* **2022**, *9*, 51.
- (5) Granger, P.; Parvulescu, V. I. *Chemical Reviews* **2011**, *111*, 3155–3207.
- (6) Zhang, J. J.; Samet, J. M. *Journal of Thoracic Disease* **2015**, *7*, 3.
- (7) Roy, S.; Hegde, M. S.; Madras, G. *Applied Energy* **2009**, *86*, 2283–2297.
- (8) Hu, E.; Huang, Z.; Zheng, J.; Li, Q.; He, J. *International Journal of Hydrogen Energy* **2009**, *34*, 6545–6557.
- (9) Galbiati, M. A.; Cavigiolo, A.; Effuggi, A.; Gelosa, D.; Rota, R. *Combustion Science and Technology* **2004**, *176*, 1035–1054.
- (10) Sepman, A.; Van Essen, V.; Mokhov, A.; Levinsky, H. *International Journal of Hydrogen Energy* **2008**, *33*, 5850–5857.
- (11) Molina, M. *Chemistry, 1991-1995* **1997**, *7*, 177.
- (12) Manisalidis, I.; Stavropoulou, E.; Stavropoulos, A.; Bezirtzoglou, E. *Frontiers in Public Health* **2020**, *8*, 14.
- (13) Majumdar, D. *Resonance* **2003**, *8*, 20–30.
- (14) Organization, W. H. et al. *Nitrate and nitrite in drinking-water: Background document for development of WHO Guidelines for Drinking-water Quality*; tech. rep.; World Health Organization, 2003.

- (15) Gholami, Z.; Luo, G.; Gholami, F.; Yang, F. *Catalysis Reviews* **2021**, *63*, 68–119.
- (16) Houshfar, E.; Skreiberg, Ø.; Todorović, D.; Skreiberg, A.; Løvås, T.; Jovović, A.; Sørum, L. *Fuel* **2012**, *98*, 29–40.
- (17) Zhu, Z.; Xu, B. *Separations* **2022**, *9*, 307.
- (18) Wang, Y.; Wang, C.; Li, M.; Yu, Y.; Zhang, B. *Chemical Society Reviews* **2021**, *50*, 6720–6733.
- (19) Catalytic Converter Market <https://www.marketsandmarkets.com/Market-Reports/catalytic-converter-systems-market-128255548.html> (accessed 03/10/2023).
- (20) Pereda-Ayo, B.; Duraiswami, D.; González-Velasco, J. R. *Catalysis Today* **2011**, *172*, 66–72.
- (21) Qiu, W.; Liu, Y.; Xie, M.; Jin, Z.; Li, P.; Yu, G. *EES Catalysis* **2023**.
- (22) He, H.; Zhang, X.; Wu, Q.; Zhang, C.; Yu, Y. *Catalysis Surveys from Asia* **2008**, *12*, 38–55.
- (23) Shelef, M.; Jones, J. H.; Kummer, J. T.; Otto, K.; Weaver, E. E. *Environmental Science & Technology* **1971**, *5*, 790–798.
- (24) Guan, Y.; Liu, Y.; Lv, Q.; Wang, B.; Che, D. *Journal of Environmental Chemical Engineering* **2021**, *9*, 106770.
- (25) Bhaskaran, A.; Sharma, D.; Roy, S.; Singh, S. A. *Environmental Science and Pollution Research* **2023**, 1–33.
- (26) Farhan, S. M.; Pan, W.; Zhijian, C.; JianJun, Y. *Fuel* **2024**, *355*, 129364.
- (27) Stenger Jr, H. G.; Hepburn, J. S. *Energy & Fuels* **1987**, *1*, 412–416.
- (28) Liu, Z.; Jia, B.; Zhang, Y.; Haneda, M. *Industrial & Engineering Chemistry Research* **2020**, *59*, 13916–13922.
- (29) Joubert, E.; Courtois, X.; Marecot, P.; Canaff, C.; Duprez, D. *Journal of Catalysis* **2006**, *243*, 252–262.
- (30) Zahaf, R.; Jung, J. W.; Coker, Z.; Kim, S.; Choi, T.-Y.; Lee, D., et al. *Aerosol and Air Quality Research* **2015**, *15*, 2409–2421.
- (31) Costa, C. N.; Efstathiou, A. M. *The Journal of Physical Chemistry C* **2007**, *111*, 3010–3020.

- (32) Machida, M; Ikeda, S; Kurogi, D; Kijima, T *Applied Catalysis B: Environmental* **2001**, *35*, 107–116.
- (33) Costa, C. N.; Stathopoulos, V.; Belessi, V.; Efstathiou, A. *Journal of Catalysis* **2001**, *197*, 350–364.
- (34) Yu, Q.; Richter, M.; Kong, F.; Li, L.; Wu, G.; Guan, N. *Catalysis Today* **2010**, *158*, 452–458.
- (35) X., J.; W., X.; Q., G.; W., J.; S., M.; L., W. *Journal of Catalysis* **2013**, *297*, 56–64.
- (36) Castegnaro, M. V.; Kilian, A. S.; Baibich, I. M.; Alves, M. C.; Morais, J. *Langmuir* **2013**, *29*, 7125–7133.
- (37) ZHENG, T.; Junjun, H.; Yunkun, Z.; Wenzheng, X.; Jieli, H. *Journal of Rare Earths* **2014**, *32*, 97–107.
- (38) Mehrabadi, B. A.; Eskandari, S.; Khan, U.; White, R. D.; Regalbuto, J. R. *Advances in Catalysis* **2017**, *61*, 1–35.
- (39) Qin, R.; Liu, K.; Wu, Q.; Zheng, N. *Chemical Reviews* **2020**, *120*, 11810–11899.
- (40) Cheng, Y.; Zhao, S.; Johannessen, B.; Veder, J.-P.; Saunders, M.; Rowles, M. R.; Cheng, M.; Liu, C.; Chisholm, M. F.; De Marco, R., et al. *Advanced Materials* **2018**, *30*, 1706287.
- (41) Konsolakis, M. *ACS Catalysis* **2015**, *5*, 6397–6421.
- (42) Wang, X.; Wen, W.; Mi, J.; Li, X.; Wang, R. *Applied Catalysis B: Environmental* **2015**, *176*, 454–463.
- (43) Väliheikki, A.; Petallidou, K. C.; Kalamaras, C. M.; Kolli, T.; Huuhtanen, M.; Maunula, T.; Keiski, R. L.; Efstathiou, A. M. *Applied Catalysis B: Environmental* **2014**, *156*, 72–83.
- (44) Luo, Y.; Wang, X.; Qian, Q.; Chen, Q. *International Journal of Hydrogen Energy* **2014**, *39*, 15836–15843.
- (45) Zhang, Z.; Zhang, Y.; Chen, Y. *Bioresource Technology* **2020**, *298*, 122444.
- (46) Liu, Y.; Wang, J. *Science of the Total Environment* **2019**, *671*, 388–403.
- (47) Tokazhanov, G.; Ramazanova, E.; Hamid, S.; Bae, S.; Lee, W. *Chemical Engineering Journal* **2020**, *384*, 123252.
- (48) Gebreeyessus, G. D. *Applied Water Science* **2019**, *9*, 135.
- (49) Mohammadi, R.; Ramasamy, D. L.; Sillanpää, M. *Desalination* **2021**, *498*, 114726.



- (50) Van Langevelde, P. H.; Katsounaros, I.; Koper, M. T. *Joule* **2021**, *5*, 290–294.
- (51) Xu, H.; Ma, Y.; Chen, J.; Zhang, W.; Yang, J. *Chemical society reviews* **2022**, *51*, 2710–2758.
- (52) Liu, J.-X.; Richards, D.; Singh, N.; Goldsmith, B. R. *Acs Catalysis* **2019**, *9*, 7052–7064.
- (53) Sanchis, I; Diaz, E; Pizarro, A.; Rodriguez, J.; Mohedano, A. *Separation and Purification Technology* **2022**, *290*, 120750.
- (54) Xiang, T.; Liang, Y.; Zeng, Y.; Deng, J.; Yuan, J.; Xiong, W.; Song, B.; Zhou, C.; Yang, Y. *Small* **2023**, 2303732.
- (55) Ullah, S.; Wang, S.; Li, C.; Jan, A. U.; Zhan, F.; Sharif, H. M. A.; Liu, Q.; Wang, G. *Journal of Environmental Chemical Engineering* **2023**, 110927.
- (56) Qin, J.; Chen, L.; Wu, K.; Wang, X.; Zhao, Q.; Li, L.; Liu, B.; Ye, Z. *ACS Applied Energy Materials* **2021**, *5*, 71–76.
- (57) Fu, X.; Zhao, X.; Hu, X.; He, K.; Yu, Y.; Li, T.; Tu, Q.; Qian, X.; Yue, Q.; Wasielewski, M. R., et al. *Applied Materials Today* **2020**, *19*, 100620.
- (58) Wang, Y.; Yin, H.; Dong, F.; Zhao, X.; Qu, Y.; Wang, L.; Peng, Y.; Wang, D.; Fang, W.; Li, J. *Small* **2023**, 2207695.
- (59) Li, L.; Tang, C.; Cui, X.; Zheng, Y.; Wang, X.; Xu, H.; Zhang, S.; Shao, T.; Davey, K.; Qiao, S.-Z. *Angewandte Chemie* **2021**, *133*, 14250–14256.
- (60) Zhang, S.; Li, M.; Li, J.; Song, Q.; Liu, X. *Proceedings of the National Academy of Sciences* **2022**, *119*, e21115504119.
- (61) Roy, S.; Baiker, A. *Chemical Reviews* **2009**, *109*, 4054–4091.
- (62) Cortés-Reyes, M.; Herrera, C.; Larrubia, M. Á.; Alemany, L. J. *Catalysis Today* **2020**, *356*, 292–300.
- (63) Gayen, A.; Baidya, T.; Biswas, K.; Roy, S.; Hegde, M. S. *Applied Catalysis A: General* **2006**, *315*, 135–146.
- (64) Roy, S.; Marimuthu, A; Hegde, M. S.; Madras, G. *Applied Catalysis B: Environmental* **2007**, *71*, 23–31.
- (65) Challagulla, S.; Payra, S.; Chakraborty, C.; Singh, S. A.; Roy, S. *Molecular Catalysis* **2019**, *476*, 110505.
- (66) Roy, S.; Marimuthu, A; Hegde, M. S.; Madras, G. *Applied Catalysis B: Environmental* **2007**, *73*, 300–310.

- (67) Li, X.; Yao, D.; Wu, F.; Wang, X.; Wei, L.; Liu, B. *ACS Omega* **2019**, *4*, 5088–5097.
- (68) Zhang, Y.-s.; Li, C.; Wang, C.; Yu, J.; Xu, G.; Zhang, Z.-g.; Yang, Y. *Industrial & Engineering Chemistry Research* **2018**, *58*, 828–835.
- (69) Yan, L.; Gu, Y.; Han, L.; Wang, P.; Li, H.; Yan, T.; Kuboon, S.; Shi, L.; Zhang, D. *ACS applied materials & interfaces* **2019**, *11*, 11507–11517.
- (70) Li, L.; Wu, Y.; Hou, X.; Chu, B.; Nan, B.; Qin, Q.; Fan, M.; Sun, C.; Li, B.; Dong, L., et al. *Industrial & Engineering Chemistry Research* **2018**, *58*, 849–862.
- (71) Han, L.; Gao, M.; Feng, C.; Shi, L.; Zhang, D. *Environmental Science & Technology* **2019**, *53*, 5946–5956.
- (72) Azambre, B.; Zenboury, L.; Da Costa, P.; Capela, S.; Carpentier, S.; Westermann, A. *Catalysis Today* **2011**, *176*, 242–249.
- (73) Amberntsson, A.; Fridell, E.; Skoglundh, M. *Applied Catalysis B: Environmental* **2003**, *46*, 429–439.
- (74) Wang, Y.; Kapteijn, F.; Makkee, M. *Applied Catalysis B: Environmental* **2018**, *231*, 200–212.
- (75) Mrad, R.; Aissat, A.; Cousin, R.; Courcot, D.; Siffert, S. *Applied Catalysis A: General* **2015**, *504*, 542–548.
- (76) Zhang, C.; Lively, R. P.; Zhang, K.; Johnson, J. R.; Karvan, O.; Koros, W. J. *The Journal of Physical Chemistry Letters* **2012**, *3*, 2130–2134.
- (77) Titi, H. M.; Marrett, J. M.; Dayaker, G.; Arhangelskis, M.; Mottillo, C.; Morris, A. J.; Rachiero, G. P.; Frišćić, T.; Rogers, R. *Science Advances* **2019**, *5*, eaav9044.
- (78) Song, Q.; Nataraj, S.; Roussenova, M. V.; Tan, J. C.; Hughes, D. J.; Li, W.; Bourgoïn, P.; Alam, M. A.; Cheetham, A. K.; Al-Muhtaseb, S. A., et al. *Energy & Environmental Science* **2012**, *5*, 8359–8369.
- (79) Wang, L.; Xu, Q.; Xu, J.; Weng, J. *RSC Advances* **2016**, *6*, 69033–69039.
- (80) Eßbach, C.; Senkovska, I.; Unmussig, T.; Fischer, A.; Kaskel, S. *ACS Applied Materials & Interfaces* **2019**, *11*, 20915–20922.
- (81) Razmjou, A.; Asadnia, M.; Ghaebi, O.; Yang, H.-C.; Ebrahimi Warkiani, M.; Hou, J.; Chen, V. *ACS Applied Materials & Interfaces* **2017**, *9*, 38076–38080.

- (82) Thomas, M.; Illathvalappil, R.; Kurungot, S.; Nair, B. N.; Mohamed, A. A. P.; Anilkumar, G. M.; Yamaguchi, T.; Hareesh, U. *ACS Applied Materials & Interfaces* **2016**, *8*, 29373–29382.
- (83) Payra, S.; Challagulla, S.; Indukuru, R. R.; Chakraborty, C.; Tarafder, K.; Ghosh, B.; Roy, S. *New Journal of Chemistry* **2018**, *42*, 19205–19213.
- (84) Khan, A. H.; Peikert, K.; Hoffmann, F.; Froba, M.; Bertmer, M. *The Journal of Physical Chemistry C* **2019**, *123*, 4299–4307.
- (85) Payra, S.; Challagulla, S.; Bobde, Y.; Chakraborty, C.; Ghosh, B.; Roy, S. *Journal of Hazardous Materials* **2019**, *373*, 377–388.
- (86) Payra, S.; Challagulla, S.; Chakraborty, C.; Roy, S. *Journal of Electroanalytical Chemistry* **2019**, *853*, 113545.
- (87) Lan, X.; Huang, N.; Wang, J.; Wang, T. *Catalysis Science & Technology* **2017**, *7*, 2601–2608.
- (88) Huang, Y.; Zhang, Y.; Chen, X.; Wu, D.; Yi, Z.; Cao, R. *Chemical Communications* **2014**, *50*, 10115–10117.
- (89) Say, Z.; Vovk, E. I.; Bukhtiyarov, V. I.; Ozensoy, E. *Applied Catalysis B: Environmental* **2013**, *142*, 89–100.
- (90) Dhainaut, F.; Pietrzyk, S.; Granger, P. *Applied Catalysis B: Environmental* **2007**, *70*, 100–110.
- (91) Barrera, A.; Viniestra, M.; Fuentes, S.; Díaz, G. *Applied Catalysis B: Environmental* **2005**, *56*, 279–288.
- (92) Vuong, T. H.; Radnik, J.; Rabeah, J.; Bentrup, U.; Schneider, M.; Atia, H.; Armbruster, U.; Grunert, W.; Bruckner, A. *ACS Catalysis* **2017**, *7*, 1693–1705.
- (93) Challagulla, S.; Payra, S.; Rameshan, R.; Roy, S. *Journal of Environmental Chemical Engineering* **2020**, *8*, 103815.
- (94) Liu, Y.; Tursun, M.; Yu, H.; Wang, X. *Molecular Catalysis* **2019**, *464*, 22–28.
- (95) Ling, L.; Cao, Y.; Zhao, Z.; Liu, P.; Wang, B.; Zhang, R.; Li, D. *Computational Materials Science* **2018**, *149*, 182–190.
- (96) Patel, V. K.; Sharma, S. *Catalysis Today* **2021**, *375*, 591–600.
- (97) Prieto-Centurion, D.; Eaton, T. R.; Roberts, C. A.; Fanson, P. T.; Notestein, J. M. *Applied Catalysis B: Environmental* **2015**, *168*, 68–76.

- (98) Roy, S.; Hegde, M. S.; Ravishankar, N.; Madras, G. *The Journal of Physical Chemistry C* **2007**, *111*, 8153–8160.
- (99) Roy, S.; Hegde, M. S. *Catalysis Communications* **2008**, *9*, 811–815.
- (100) Roy, S.; Marimuthu, A.; Hegde, M. S.; Madras, G. *Catalysis Communications* **2008**, *9*, 101–105.
- (101) Bera, P.; Hegde, M. S. *Catalysis surveys from Asia* **2011**, *15*, 181–199.
- (102) Roy, S.; Viswanath, B.; Hegde, M. S.; Madras, G. *The Journal of Physical Chemistry C* **2008**, *112*, 6002–6012.
- (103) Roy, S.; Hegde, M. S.; Sharma, S.; Lalla, N.; Marimuthu, A.; Madras, G. *Applied Catalysis B: Environmental* **2008**, *84*, 341–350.
- (104) Roy, S.; Marimuthu, A.; Deshpande, P. A.; Hegde, M. S.; Madras, G. *Industrial & engineering chemistry research* **2008**, *47*, 9240–9247.
- (105) Sarode, P. R.; Asakura, K.; Priolkar, K.; Hegde, M. *AIP Conf. Proc.* **2018**, *1953*, 070009.
- (106) Du, Q.; Cheng, X.; Tahir, M. H.; Su, D.; Wang, Z.; Chen, S. *International Journal of Hydrogen Energy* **2020**, *45*, 16469–16481.
- (107) Lee, K.-M.; Kwon, G.; Hwang, S.; Boscoboinik, J. A.; Kim, T. *Catalysis Science & Technology* **2021**, *11*, 7850–7865.
- (108) Wang, Y.; Zhu, A.; Zhang, Y.; Au, C.; Yang, X.; Shi, C. *Applied Catalysis B: Environmental* **2008**, *81*, 141–149.
- (109) Roy, S.; Challagulla, S. *Solution Combustion Synthesis Of Nanostructured Solid Catalysts For Sustainable Chemistry* **2020**, *5*, 87.
- (110) Challagulla, S.; Roy, S. *Journal of Materials Research* **2017**, *32*, 2764–2772.
- (111) Giannozzi, P.; Baroni, S.; Bonini, N.; Calandra, M.; Car, R.; Cavazzoni, C.; Ceresoli, D.; Chiarotti, G. L.; Cococcioni, M.; Dabo, I., et al. *Journal of Physics: Condensed Matter* **2009**, *21*, 395502.
- (112) Perdew, J. P.; Burke, K.; Ernzerhof, M. *Physical Review Letters* **1996**, *77*, 3865.
- (113) Bennett, L. J.; Jones, G. *Physical Chemistry Chemical Physics* **2014**, *16*, 21032–21038.
- (114) Henkelman, G.; Uberuaga, B. P.; Jónsson, H. *The Journal of Chemical Physics* **2000**, *113*, 9901–9904.

- (115) Yang, C.; Yu, X.; Heißler, S.; Weidler, P. G.; Nefedov, A.; Wang, Y.; Wöll, C.; Kropp, T.; Paier, J.; Sauer, J. *Angewandte Chemie International Edition* **2017**, *56*, 16399–16404.
- (116) Baidya, T.; Mazumder, T.; Koltunov, K. Y.; Likhar, P. R.; Clark, A. H.; Tiwari, K.; Sobolev, V. I.; Payra, S.; Murayama, T.; Lin, M., et al. *The Journal of Physical Chemistry C* **2020**, *124*, 14131–14146.
- (117) Qi, W.; Xie, K.; Liu, M.; Wu, G.; Wang, Y.; Zhang, Y.; Wu, Y. *RSC Advances* **2014**, *4*, 40494–40504.
- (118) Mahammadunnisa, S.; Reddy, P. M. K.; Lingaiah, N; Subrahmanyam, C. *Catalysis Science & Technology* **2013**, *3*, 730–736.
- (119) Shannon, R. D. *Acta crystallographica section A: crystal physics, diffraction, theoretical and general crystallography* **1976**, *32*, 751–767.
- (120) Payra, S.; Roy, S. *The Journal of Physical Chemistry C* **2021**, *125*, 8497–8507.
- (121) Mazumder, T.; Dandapat, S.; Baidya, T.; Likhar, P. R.; Clark, A. H.; Bera, P.; Tiwari, K.; Payra, S.; Srinivasa Rao, B.; Roy, S., et al. *The Journal of Physical Chemistry C* **2021**, *125*, 20831–20844.
- (122) Hengne, A. M.; Samal, A. K.; Enakonda, L. R.; Harb, M.; Gevers, L. E.; Anjum, D. H.; Hedhili, M. N.; Saih, Y.; Huang, K.-W.; Basset, J.-M. *ACS Omega* **2018**, *3*, 3688–3701.
- (123) Dubey, P; Kaurav, N.; Devan, R. S.; Okram, G.; Kuo, Y. *RSC Advances* **2018**, *8*, 5882–5890.
- (124) Vanpoucke, D. E.; Bultinck, P.; Cottenier, S.; Van Speybroeck, V.; Van Driessche, I. *Journal of Materials Chemistry A* **2014**, *2*, 13723–13737.
- (125) Soni, S.; Chouhan, N.; Meena, R. K.; Kumar, S.; Dalela, B.; Mishra, M.; Meena, R. S.; Gupta, G.; Kumar, S.; Alvi, P. A., et al. *Global Challenges* **2019**, *3*, 1800090.
- (126) Wang, J.; Gao, F.; Dang, P.; Tang, X.; Lu, M.; Du, Y.; Zhou, Y.; Yi, H.; Duan, E. *Chemical Engineering Journal* **2022**, *450*, 137374.
- (127) Zhao, S.; Peng, J.; Ge, R.; Wu, S.; Zeng, K.; Huang, H.; Yang, K.; Sun, Z. *Fuel Processing Technology* **2022**, *236*, 107432.
- (128) Herzberg, G., *Molecular spectra and molecular structure*; D. van Nostrand: 1945.
- (129) Kukolich, S. G. *Journal of the American Chemical Society* **1982**, *104*, 4715–4716.
- (130) Kalamaras, C. M.; Olympiou, G. G.; Pârvulescu, V. I.; Cojocaru, B.; Efstathiou, A. M. *Applied Catalysis B: Environmental* **2017**, *206*, 308–318.

- (131) Chen, J.; Zhan, Y.; Zhu, J.; Chen, C.; Lin, X.; Zheng, Q. *Applied Catalysis A: General* **2010**, *377*, 121–127.
- (132) Dima, G.; De Vooy, A.; Koper, M. *Journal of Electroanalytical Chemistry* **2003**, *554*, 15–23.
- (133) Calle-Vallejo, F.; Huang, M.; Henry, J. B.; Koper, M. T.; Bandarenka, A. S. *Physical Chemistry Chemical Physics* **2013**, *15*, 3196–3202.
- (134) Casella, I. G.; Contursi, M. *Electrochimica Acta* **2014**, *138*, 447–453.
- (135) Gong, Z.; Zhong, W.; He, Z.; Jia, C.; Zhou, D.; Zhang, N.; Kang, X.; Chen, Y. *Catalysis Today* **2022**, *402*, 259–265.
- (136) Wang, Y.; Zhou, W.; Jia, R.; Yu, Y.; Zhang, B. *Angewandte Chemie International Edition* **2020**, *59*, 5350–5354.
- (137) Payra, S.; Kanungo, S.; Roy, S. *Nanoscale* **2022**, *14*, 13352–13361.
- (138) Payra, S.; Devaraj, N.; Tarafder, K.; Roy, S. *ACS Applied Energy Materials* **2022**, *5*, 4945–4955.
- (139) Payra, S.; Shenoy, S.; Chakraborty, C.; Tarafder, K.; Roy, S. *ACS Applied Materials & Interfaces* **2020**, *12*, 19402–19414.
- (140) Liu, Y.; Deng, B.; Li, K.; Wang, H.; Sun, Y.; Dong, F. *Journal of Colloid and Interface Science* **2022**, *614*, 405–414.
- (141) Payra, S.; Reddy, K. L.; Sharma, R. S.; Singh, S.; Roy, S. *Journal of Hazardous Materials* **2020**, *393*, 122491.
- (142) Chen, G.-F.; Yuan, Y.; Jiang, H.; Ren, S.-Y.; Ding, L.-X.; Ma, L.; Wu, T.; Lu, J.; Wang, H. *Nature Energy* **2020**, *5*, 605–613.
- (143) Zhang, N.; Shang, J.; Deng, X.; Cai, L.; Long, R.; Xiong, Y.; Chai, Y. *ACS Nano* **2022**, *16*, 4795–4804.
- (144) Zhang, X.; Wang, Y.; Liu, C.; Yu, Y.; Lu, S.; Zhang, B. *Chemical Engineering Journal* **2021**, *403*, 126269.
- (145) Zhao, J.; Liu, L.; Yang, Y.; Liu, D.; Peng, X.; Liang, S.; Jiang, L. *ACS Sustainable Chemistry & Engineering* **2023**, *11*, 2468–2475.
- (146) He, L.; Yao, F.; Zhong, Y.; Tan, C.; Hou, K.; Pi, Z.; Chen, S.; Li, X.; Yang, Q. *Journal of Hazardous Materials* **2022**, *436*, 129253.

- (147) Ayyub, M. M.; Rao, C. *Materials Horizons* **2021**, *8*, 2420–2443.
- (148) Qiao, Y.; Peng, M.; Lan, J.; Jiang, K.; Chen, D.; Tan, Y. *Journal of Materials Chemistry A* **2023**, *11*, 495–511.
- (149) He, Q.; Wang, H.; Zhao, X.; Chen, L. *Materials Today Chemistry* **2021**, *22*, 100564.
- (150) Li, S.; Gao, Y.; Li, N.; Ge, L.; Bu, X.; Feng, P. *Energy & Environmental Science* **2021**, *14*, 1897–1927.
- (151) Bashir, Y.; Raj, R.; Das, S.; Ghangrekar, M. *Water, Air, & Soil Pollution* **2023**, *234*, 91.
- (152) Xiong, B.; Yang, Y.; Liu, J.; Ding, J.; Yang, Y. *Applied Surface Science* **2021**, *567*, 150839.
- (153) Badawy, I. M.; Ismail, A. M.; Khedr, G. E.; Taha, M. M.; Allam, N. K. *Scientific Reports* **2022**, *12*, 13456.
- (154) Wang, J.; Zhang, L.; Wang, Y.; Niu, Y.; Fang, D.; Su, Q.; Wang, C. *Dalton Transactions* **2022**, *51*, 15111–15120.
- (155) Gao, J.; Jiang, B.; Ni, C.; Qi, Y.; Zhang, Y.; Oturan, N.; Oturan, M. A. *Applied Catalysis B: Environmental* **2019**, *254*, 391–402.
- (156) Wu, Z.-Y.; Karamad, M.; Yong, X.; Huang, Q.; Cullen, D. A.; Zhu, P.; Xia, C.; Xiao, Q.; Shakouri, M.; Chen, F.-Y., et al. *Nature Communications* **2021**, *12*, 2870.
- (157) Durai, L.; Gopalakrishnan, A.; Badhulika, S. *Energy & Fuels* **2021**, *35*, 12507–12515.
- (158) Srivastava, A.; Sahu, P.; Murali, M.; Ali, S. M.; Sahu, M.; Pillai, J. S.; Rawat, N. *Journal of Electroanalytical Chemistry* **2021**, *901*, 115752.
- (159) Jiao, S.; Fu, X.; Huang, H. *Advanced Functional Materials* **2022**, *32*, 2107651.
- (160) Zhang, Z.; Wen, G.; Luo, D.; Ren, B.; Zhu, Y.; Gao, R.; Dou, H.; Sun, G.; Feng, M.; Bai, Z., et al. *Journal of the American Chemical Society* **2021**, *143*, 6855–6864.

## List of Publications and Conference Presentations

### Publications from thesis work

1. Challagulla, S., Payra, S., Rameshan, R., & Roy, S. (2020). Low temperature catalytic reduction of NO over porous Pt/ZIF-8. *Journal of Environmental Chemical Engineering*, 8(4), 103815.
2. Rameshan, R., Pentyala, P., Singh, S. A., Deshpande, P. A., & Roy, S. (2022). Probing the surface active sites of  $Ce_{1-x}Ni_xO_{2-\delta}$  for catalytic reduction of NO. *Journal of Environmental Chemical Engineering*, 10(6), 108966.
3. Rameshan, R., Tiwari, A., Kanungo, S., Roy, S. (2023). Rags to Riches: Meliorating the Electrocatalytic Reduction of Nitrate to Ammonia over Cu-Based Nanoalloys. *Inorganic Chemistry*, 62(25), 9934–9944.

### Other publications

1. Saminathan, M., Muthiah, S., Ravi, L., Bhui, A., Rameshan, R., Perumal, S. (2022). Improved thermoelectric properties of Fe doped Si-rich higher manganese silicide. *Materials Science and Engineering: B*, 284, 115912.

### Conference Presentations

1. Poster: Challagulla, S., Payra, S., Rameshan, R., & Roy, S., Thermal Reduction of NO over Nobel metal loaded Metal-Organic Framework, National symposium on Convergence of Chemistry of Materials (CCM-2019) organized by Department of Chemistry, BITS Pilani - Hyderabad Campus, India - Consolation prize
2. Poster: Rameshan, R., Pentyala, P., Singh, S. A., Deshpande, P. A., & Roy, S., Investigating role of surface active sites of  $Ce_{1-x}Ni_xO_{2-\delta}$  for the thermal catalytic NO reduction, National symposium on Convergence of Chemistry of Materials (CCM-2023) organized by Department of Chemistry, BITS Pilani - Hyderabad Campus, India - Consolation prize



## **Biography of Reeshma Rameshan**

Reeshma Rameshan completed her M. Tech in Materials Science and Engineering from the University of Mysore. She started her career as a Junior Research Fellow at SRM Institute of Science and Technology (SRMIST), Kattankulathur, Chennai. Later she was appointed as a Junior Research Fellow in the HBL-sponsored project titled "Preparation and characterization of electrode material for Lithium Ion Batteries" at BITS-Pilani, Hyderabad campus under the supervision of Prof. Sounak Roy. Her research interest includes materials synthesis and applications towards environmental remediation. She authored/co-authored five publications in international and national peer-reviewed journals and presented posters at national conferences.

## **Biography of Prof. Sounak Roy**

Prof. Sounak Roy is working as a Professor in the Department of Chemistry at Birla Institute of Technology and Science, Pilani, Hyderabad Campus, India. His research interests encompass around solid state chemistry, energy, and environmental catalysis, and understanding the reaction mechanism in light of the structure-property relationship. Currently, his group is engaged in the area of catalytic NO<sub>x</sub> abatement, conversion of CO<sub>2</sub> to biofuels, water splitting and fuel cells.